UNIVERSIDADE FEDERAL DO RIO GRANDE DO SUL
PROGRAMA DE PÓS-GRADUAÇÃO EM MICROELETRÔNICA

MAURÍCIO BANASZESKI DA SILVA

A Physics-Based Statistical Random Telegraph Noise Model

Thesis presented in partial fulfillment of the requirements for the degree of doctorate in Microelectronics

Prof. Dr. Gilson Wirth
Advisor

Porto Alegre
2016

CIP – CATALOGAÇÃO NA PUBLICAÇÃO

Banaszeski da Silva, Maurício
A Physics-Based Statistical Random Telegraph Noise Model [manuscrito] /Maurício Banasaseski da Silva – 2016.
126 f.:il.
Orientador: Gilson Inácio Wirth;
Tese (Doutorado) – Universidade Federal do Rio Grande do Sul. Programa de Pós-Graduação em Microeletrônica. Porto Alegre, BR – RS, 2016.
1. Flicker Noise 2. Halo Implants 3. Low Frequency Noise (LFN) 4. MOSFETs 5. Power Spectral Density (PSD) 6. Random Telegraph Noise (RTN), 7. Statistical Model 8. Variability. I. Wirth, Gilson Inácio. II. A Physics-Based Statistical Random Telegraph Noise Model.

This Thesis is dedicated to the memory of my mother, Clecy Lourdes

For her endless love and for being my role model of life

Esta Tese é dedicada à memória da minha mãe, Clecy Lourdes

Por seu amor imenso e por ser meu modelo de vida

ACKNOWLEDGEMENT

First and foremost, I thank my parents for their love and support through my life. Words cannot express how grateful I am to my mother, Clecy, and my father, Fernando, for all of the sacrifices that they have made on my behalf. I thank to my sister, Alessandra, for the support in this important time of our life. My whole family deserves a wholehearted thanks.

I would like to thank my supervisor, Prof. Dr. Gilson I. Wirth, for his guidance through this study and his confidence in me. I would like also to thank Dr. Hans Tuinhout and Dr. Andrie Scholten, for their hospitality, knowledge and guidance. I must acknowledge as well Adrie Duijnhoven for the hospitality and for the excellent measurements provided.

I am grateful too for the hard work of my faculty colleagues, professors and staffs. I am also grateful for the hard work of NXP Semiconductors staffs and for the opportunity to be part of the company during my doctorate.

ABSTRACT

Low Frequency Noise (LFN) and Random Telegraph Noise (RTN) are performance limiters in many analog and digital circuits. For small area devices, the noise power spectral density can easily vary by many orders of magnitude, imposing serious threat on circuit performance and possibly reliability. In this thesis, we propose a new RTN model to describe the statistics of the low frequency noise in MOSFETs. Using the proposed model, we can explain and calculate the Expected value and Variability of the noise as function of devices' biases, geometry and physical parameters. The model is validated through numerous experimental results for n-channel and p-channel devices from different CMOS technology nodes. We show that the LFN statistics of n-channel and p-channel MOSFETs can be described by the same mechanism. From our results and model, we show that the trap density of the p-channel device is a strongly varying function of the Fermi level, whereas for the n-channel the trap density can be considered constant. We also show and explain, using the proposed model, the impact of the halo-implanted regions on the statistics of the noise. Using this model, we clarify why the variability, denoted by $\sigma[\log(S_{Id})]$, of RTN/LFN doesn't follow a $1/\sqrt{\text{area}}$ dependence; and we demonstrate that the noise, and its variability, found in our measurements can be modeled using reasonable physical quantities. Moreover, the proposed model can be used to calculate the percentile quantity of the noise, which can be used to predict or to achieve certain circuit yield.

Keywords: Flicker Noise. Halo implants. Low Frequency noise (LFN). MOSFETs. Power Spectral Density (PSD). Random Telegraph Noise (RTN). Statistical Model. Variability.

Um Modelo Estatístico e Fisicamente Baseado para o Ruído RTN

RESUMO

O Ruído de Baixa Frequência (LFN), tais como o ruído *flicker* e o *Random Telegraph Noise* (RTN), são limitadores de performance em muitos circuitos analógicos e digitais. Para transistores diminutos, a densidade espectral de potência do ruído pode variar muitas ordens de grandeza, impondo uma séria limitação na performance do circuito e também em sua confiabilidade. Nesta tese, nós propomos um novo modelo de RTN estatístico para descrever o ruído de baixa frequência em MOSFETs. Utilizando o modelo proposto, pode-se explicar e calcular o valor esperado e a variabilidade do ruído em função das polarizações, geometrias e dos parâmetros físicos do transistor. O modelo é validado através de inúmeros resultados experimentais para dispositivos com canais tipo *n* e *p*, e para diferentes tecnologias CMOS. É demonstrado que a estatística do ruído LFN dos dispositivos de canal tipo *n* e *p* podem ser descritos através do mesmo mecanismo. Através dos nossos resultados e do nosso modelo, nós mostramos que a densidade de armadilhas dos transistores de canal tipo *p* é fortemente dependente do nível de Fermi, enquanto para o transistor de tipo *n* a densidade de armadilhas pode ser considerada constante na energia. Também é mostrado e explicado, através do nosso modelo, o impacto do implante de *halo* nas estatísticas do ruído. Utilizando o modelo demonstra-se porque a variabilidade, denotado por $\sigma[\log(S_{Id})]$, do RTN/LFN não segue uma dependência 1/√área; e fica demonstrado que o ruído, e sua variabilidade, encontrado em nossas medidas pode ser modelado utilizando parâmetros físicos. Além disso, o modelo proposto pode ser utilizado para calcular o percentil do ruído, o qual pode ser utilizado para prever ou alcançar certo rendimento do circuito.

Palavras-chaves: Ruído Flicker. Implantes de Halo. Ruído de Baixa Frequência (LFN). MOSFETs. Densidade Espectral de Potência (PSD), Random Telegraph Noise (RTN). Modelo Estatístico. Variabilidade.

LIST OF FIGURES

Figure 1.1 – Representation of the noise power spectral density of an arbitrary MOS transistor 14
Figure 1.2 – Example of a bump present in the LFN spectrum. 15
Figure 1.3 – Example of the LFN of large devices with WL = 100×8μm^2. 15
Figure 1.4 – Noise spectra of 48 devices with WL = 100×8μm^2. 16
Figure 1.5 – Example of 3 noise spectra of small devices with WL = 1×0.06μm^2. 16
Figure 1.6 – Noise spectra of 282 devices with WL = 1×0.06μm^2. 17
Figure 1.7 – Standard deviation of the logarithm of the noise for various device areas. 17
Figure 1.8 – Wrong method for fitting noise variability. 19
Figure 1.9 – Ideal Pelgrom behavior of the standard deviation. 19
Figure 1.10 – Upconversion of the LFN. 19
Figure 1.11 – Period Jitter. 20
Figure 2.1 – Illustration of the RTS given by the impact of a single defect in the oxide. 21
Figure 2.2 – Illustration of a RTN spectrum in log-log domain. 21
Figure 2.3 – Distribution of the emission time of a trap [3]. 22
Figure 2.4 – Comparison among three flicker noise models. 27
Figure 2.5 – Difference between the noise behavior of NMOS and PMOS devices. 28
Figure 3.1 – Illustration of the noise given by the summation of traps with log-uniformly distributed time constants. 29
Figure 3.2 – Average of the noise spectra of a small area device. 30
Figure 3.3 – Noise distribution for three different devices' area. 30
Figure 3.4 – Example of the Noise Variability Model prediction. 31
Figure 3.5 – Plot of $\beta/(\beta+1)^2$ as a function of the trap energy, for E_F = 0.75 V. 33
Figure 3.6 – Arbitrary trap distribution in energy used in the Monte Carlo simulation. 37
Figure 3.7 – Expected value calculated using the proposed model (solid line) and Monte Carlo (symbols) for different quasi-Fermi levels. 37
Figure 3.8 – Variance calculated using the proposed model (solid line) and Monte Carlo (symbols) for different quasi-Fermi levels. 37
Figure 4.1 – Charge balance in a small cross section of a NMOS transistor. 40
Figure 4.2 – Change on the conductivity of a segment of a uniformly inverted channel device given by an occupied trap. 41
Figure 4.3 – Comparison between the mobility fluctuation and number fluctuation components. 45
Figure 4.4 – Equivalent transistor for calculating the current deviation. 46
Figure 5.1 – Area scaling of the Expected value of the LF noise, for n-channel devices in 140-nm technology. V_{gs} = 1.4 and V_{ds} = 0.1V. 52
Figure 5.2 – Area scaling of the Variance of the LF noise, for n-channel devices in 140-nm technology. V_{gs} = 1.4 and V_{ds} = 0.1V. 52
Figure 5.3 – K value for different area devices, for n-channel devices in 140-nm technology. V_{gs} = 1.4 and V_{ds} = 0.1V. 53
Figure 5.4 – Area scaling of the Standard Deviation of the logarithm of LF noise, for n-channel devices in 140-nm technology. V_{gs} = 1.4 and V_{ds} = 0.1V. 54
Figure 5.5 – Same data as in Figure 5.4 now plotted on log-log scale, to demonstrate that the model converges to 1/√area for large devices and that no noise saturation occurs near the origin of Figure 5.4. 54
Figure 5.6 – Example of the LFN Variability model prediction for a population of large geometry devices plotted back into the original spectra using (5.6) with K=5e-13m^2. Measured: 43 devices (WL=30×0.336μm^2) with V_{ds}=100mV and V_{gs}=1.4V. 54
Figure 5.7 – Example of the LFN Variability model prediction for a population of small geometry devices plotted back into the original spectra. K=5e-13m^2. Measured: 43 devices (WL=0.232×0.16μm^2) with V_{ds}=100mV and V_{gs}=1.4V. 54

Figure 5.8 – Area scaling of the Expected value of the LF noise, for p-channel devices in 140-nm technology, $V_{gs} = -1.4$ V and $V_{ds} = -0.1$V....55
Figure 5.9 – Area scaling of the Variance of the LF noise, for p-channel devices in 140-nm technology, $V_{gs} = -1.4$ V and $V_{ds} = -0.1$V. 55
Figure 5.10 – K value for different area devices, for p-channel devices in 140-nm technology, $V_{gs} = -1.4$ V and $V_{ds} = -0.1$V....55
Figure 5.11 – Area scaling of the Standard Deviation of the logarithm of LF noise for p-channel devices in 140-nm technology, $V_{gs}= -1.4$ and $V_{ds}= -0.1$V. 55
Figure 5.12 – Area scaling of the Expected value of the LF noise, for devices in 40-nm technology. $|V_{gs}| = 1.1$ V and $|V_{ds}| = 50$ mV. 56
Figure 5.13 – Area scaling of the Variance of the LF noise, for devices in 40-nm technology, $V_{gs} = 1.1$ V and $V_{ds} = 50$ mV. 56
Figure 5.14 – K value for different area devices, for devices in 40-nm technology. $|V_{gs}| = 1.1$ V and $|V_{ds}| = 50$ mV. 56
Figure 5.15 – Area scaling of the Standard Deviation of the logarithm of the LF noise for devices in 40-nm technology. Fitted using (5.6) with K=3.7×10^{-13} m^2 for NMOS and 1.2×10^{-13} m^2 for PMOS. $|V_{ds}| = 50$mV and $|V_{gs}| = 1.1$V. 56
Figure 5.16 – Area scaling of the Expected value of the LF noise, for devices in 65-nm GO2 technology. $|V_{gs}| = 2.5$ V and $|V_{ds}| = 0.5$ V. 56
Figure 5.17 – Area scaling of the Variance of the LF noise, for devices in 65-nm GO2 technology. $|V_{gs}| = 2.5$ V and $|V_{ds}| = 0.5$ V. 56
Figure 5.18 – K value for different area devices, for devices in 65-nm GO2 technology. $|V_{gs}| = 1.1$ V and $|V_{ds}| = 50$ mV. 57
Figure 5.19 – Area scaling of the Standard Deviation of the logarithm of the LF noise for devices in 65-nm GO2 technology. Fitted using (5.6) with $K = 1.9\times10^{-12}$ m^2 for NMOS and $K = 5.4\times10^{-13}$ m^2 for PMOS. $|V_{ds}| = 0.5$ V and $|V_{gs}| = 2.5$ V. 57
Figure 5.20 – LF noise PSD variability of 43 n-channel devices with W = 8 µm, using V_{ds}=0.5V and V_{gs}=0.5V. 59
Figure 5.21 – Variability as a function of the channel width for various bias configuration, $L = 0.32$ µm. 60
Figure 5.22 – Difference between the K behavior for short and long channel devices. 61
Figure 5.23 – LF noise PSD of 43 NMOS 140-nm node devices, $W = 8$ µm, $L = 8$µm, V_{gs}=1.4 and V_{ds}=0.5 V. 61
Figure 5.24 – LF noise PSD of 43 NMOS 140-nm node devices, $W = 8$ µm, $L = 8$ µm, Vgs = 0.5 and Vds = 0.5 V. 61
Figure 5.25 – Extracted K of 43 n-channel devices in 140-nm technology with $V_{ds} = 0.1$ V. $W = 8$ µm and various channel lengths. 62
Figure 5.26 – Extracted K of 43 n-channel devices in 140-nm technology with $V_{ds} = 0.5$ V. $W = 8$ µm and various channel lengths. 62
Figure 5.27 – Extracted K of 43 n-channel devices in 140-nm technology with $V_{ds} = 1.8$ V. $W = 8$ µm and various channel lengths. 62
Figure 5.28 – Extracted K of 63 n-channel devices in 40-nm technology with $V_{ds} = 0.05$ V. $W = 0.9$ µm and various channel lengths. For 9-µm long devices, $W = 9$µm. 63
Figure 5.29 – Extracted K of 63 n-channel devices in 40-nm technology with $V_{ds} = 0.55$ V....63
Figure 5.30 – Extracted K of 63 n-channel devices in 40-nm technology with $V_{ds} = 1.1$ V....63
Figure 5.31 – Extracted K of 282 n-channel devices in 65-nm GO1 technology with $V_{ds} = 0.5$ V. $W = 1$ µm and various channel lengths. For the 10-µm long devices, $W = 10$µm....63
Figure 5.32 – Extracted K of 68 NMOS 65-nm node GO2 devices with $V_{ds} = 0.5$ V. $W = 1$ µm and various channel lengths. For 10-µm long devices, $W = 10$µm. 63
Figure 5.33 – Expected value of 43 p-channel devices in 140-nm technology, with $W\times L = 8\times0.14$µm^2 and $|V_{ds}| = 0.1$ V. 65
Figure 5.34 – K value of p-channel devices in 140-nm technology, with $W\times L = 8\times0.14$µm^2 and $|V_{ds}| = 0.1$ V. 65

Figure 5.35 – Extracted K of 43 p-channel devices in 140-nm node, with $W = 8$ μm, $V_{ds} = 0.1$ V and various channel lengths. 65
Figure 5.36 – Extracted K of 43 p-channel devices in 140-nm node, with $W = 8$ μm, $V_{ds} = 0.5$ V and various channel lengths. 65
Figure 5.37 – Extracted K of 43 p-channel devices in 140-nm node, with $W = 8$ μm, $V_{ds} = 1.8$ V and various channel lengths. 65
Figure 6.1 – Schematic of the calibration process. 67
Figure 6.2 – CV curve comparison for the n-channel 140-nm technology. 67
Figure 6.3 – IV curve of a large channel device with low drain bias. 68
Figure 6.4 – IV curve of a short channel device with low drain bias. 68
Figure 6.5 – IV curve of a short channel device with high drain bias. 68
Figure 6.6 – One-electron normalization of the current deviation for different mesh sizes. $Q_t/q = 2\times10^{10}$ cm^{-2}. 70
Figure 6.7 – One-electron normalization of the current deviation for different mesh sizes. 70
Figure 6.8 – Description of the current deviation equation. 71
Figure 6.9 – 2-D cross-section of a long channel device (1 μm), showing the net doping gradient. Halo-implanted regions are far apart. 72
Figure 6.10 – Normalized impact vs. channel position, high V_{gs}, low V_{ds}, L = 8 μm. 73
Figure 6.11 – Normalized impact vs channel position, low V_{gs}, low V_{ds}, L = 8 μm. 73
Figure 6.12 – Normalized impact vs. channel position, high V_{gs}, high V_{ds}, L = 8 μm. 74
Figure 6.13 – Normalized impact vs. channel position, low V_{gs}, high V_{ds}, L = 8 μm. 74
Figure 6.14 – 2-D cross-section of a 0.32-μm device showing the net doping gradient. Halo-implanted regions are very close to each other. 74
Figure 6.15 – Normalized impact vs. channel position, high V_{gs}, low V_{ds}, L = 0.32 μm. 75
Figure 6.16 – Normalized impact vs channel position, low V_{gs}, low V_{ds}, L = 0.32 μm. 75
Figure 6.17 – Normalized impact vs. channel position, high V_{gs}, high V_{ds}, L = 0.32 μm. 75
Figure 6.18 – Normalized impact vs. channel position, low V_{gs}, high V_{ds}, L = 0.32 μm. 75
Figure 6.19 – Carriers density as a function of the normalized channel position for three different channel length. V_{gs} = 1.8 V and V_{ds}=1.8 V. 75
Figure 6.20 – 2-D cross-section of a 0.14-μm device showing the net doping gradient. Halo-implanted regions are overlapped. 76
Figure 6.21 – Normalized impact vs. channel position, high V_{gs}, low V_{ds}, L = 0.14 μm. 76
Figure 6.22 – Normalized impact vs channel position, low V_{gs}, low V_{ds}, L = 0.14 μm. 76
Figure 6.23 – Normalized impact vs. channel position, high V_{gs}, high V_{ds}, L = 0.14 μm. 77
Figure 6.24 – Normalized impact vs. channel position, low V_{gs}, high V_{ds}, L = 0.14 μm. 77
Figure 6.25 – Measured versus calculated K. L=0.14 μm. 78
Figure 6.26 – Measured versus calculated Standard Deviation. W = 8 μm, L = 0.14 μm. 78
Figure 6.27 – Measured versus calculated Expected value. L=0.14 μm. 78
Figure 6.28 – Measured versus calculated Variance. L = 0.14 μm. 78
Figure 6.29 – Measured versus calculated Expected value. L=0.32 μm. 79
Figure 6.30 – Measured versus calculated Variance. L=0.32 μm. 79
Figure 6.31 – Measured versus calculated K. L=0.32 μm. 79
Figure 6.32 – Measured versus calculated Standard Deviation. L=0.32 μm. 79
Figure 6.33 – Measured versus calculated Expected value. L=1 μm. 79
Figure 6.34 – Measured versus calculated Variance. L=1 μm. 79
Figure 6.35 – Measured versus calculated K. L=1 μm. 80
Figure 6.36 – Measured versus calculated Standard deviation. L=1 μm 80
Figure 6.37 – Measured vs calculated Expected value. L=8 μm 80
Figure 6.38 – Measured vs calculated Variance. L=8 μm 80
Figure 6.39. – Measured versus calculated K. L=8 μm 81
Figure 6.40 – Measured vs calculated Standard Deviation. L=8 μm. 81
Figure 6.41 – Extracted K of 43 PMOS 140-nm node devices with V_{ds} = 0.5 V. 81

Figure 6.42 – Normalized impact versus channel position for an 8-µm long p-channel device with low V_{gs} and low V_{ds}. 81
Figure 6.43 – Trap distribution used for the calculation of PMOS devices. 82
Figure 6.44 – Conversion from trap density as a function of quasi-Fermi level to trap density as a function of channel position. 83
Figure 6.45 – LFN Measurements versus proposed model, for p-channel devices with L=1µm. 84
Figure 6.46 – LFN Measurements versus proposed model, for p-channel devices with L=0.316µm. 84
Figure 6.47 – LFN Measurements versus proposed model, for p-channel devices with L = 0.14 µm. 85
Figure 6.48 – LFN Measurements versus proposed model using the trap density 20% higher, for p-channel devices with L=0.14µm. 85
Figure 6.49 – LFN Measurements versus proposed model, for 9-µm long n-channel devices in 40-nm technology. 86
Figure 6.50 – LFN Measurements versus proposed model, for 0.9-µm long n-channel devices in 40-nm technology. 87
Figure 6.51 – LFN Measurements versus proposed model, for 0.04-µm long n-channel devices in 40-nm technology. 87
Figure 7.1 – Expected value of long channel and uniformly doped devices, calculated using the full model in (5.10) (solid lines) and the compact model in (6.17) (dashed lines). 91
Figure 7.2 – K value of long channel and uniformly doped devices calculated using the full model in (6.11) (solid lines) and the compact model in (6.18) (dashed lines). 91
Figure 7.3 – Expected value of 8×1µm^2 p-channel devices in 140-nm technology. Comparison between measured data (solid symbols) and calculated using the compact model (dashed lines). 92
Figure 7.4 – K value of 8×1µm^2 p-channel devices in 140-nm technology. Comparison between measured data (solid symbols) and calculated using the compact model (dashed lines). 92
Figure 7.5 – Example of the lateral doping gradient introduced by the halo implants. 93
Figure 7.6 – Simplification of the halo-implanted device in three different uniform regions. 94
Figure 7.7 – Weak inversion approximation for the Expected value of n-channel 40-nm devices. V_{ds}=0.05V 97
Figure 7.8 – Weak inversion approximation for K value of n-channel 40-nm devices. V_{ds}=0.05V 97
Figure 7.9 – Weak inversion approximation for the Expected value of n-channel 140-nm devices. V_{ds}=0.1V. 97
Figure 7.10 – Weak inversion approximation for K value of n-channel 140-nm devices. V_{ds}=0.1V. 97
Figure 7.11 – Comparison between the measured (solid symbols) and calculated (dashed lines) Standard Deviation of the logarithm of the LFN for different channel lengths. V_{gs} = 0.5 V and V_{ds} = 0.1V. 98
Figure 7.12 – Weak inversion approximation of the current deviation for 1-µm long devices in 140-nm technology with V_{gs}=0.4V and V_{ds}=0.1V. 98
Figure 7.13 – Weak inversion approximation of the current deviation for 1-µm long devices in 140-nm technology with V_{gs}=0.4V and V_{ds}=1.8V. 98
Figure 7.14 – A calculated using the proposed simplifications and calculated solving the 1D Poisson equation with $V_{fb} = -0.82$ V, $N_{a,ch} = 4.5\times10^{17}$ cm^{-2}, $N_{a,h} = 8\times10^{17}$ cm^{-2} and Tox = 3 nm. 99
Figure 7.15 – Schematic of the three transistors model. 99
Figure 8.1 – Q-Q plot of ln(S_{Id}) for 10×10 µm^2 devices in 65-nm GO1 technology with V_{gs} = 1.2 V. Dashed lines represent the lognormal fit, symbols represent the measured data. 102
Figure 8.2 – Q-Q plot of ln(S_{Id}) for 10×10 µm^2 devices in 65-nm GO1 technology with V_{gs} = 0.4 V. Dashed lines represent the lognormal fit, symbols represent the measured data. 102
Figure 8.3 – Q-Q plot of the normalized ln(S_{Id}). The normalization is done to coincide the left tails of both distributions. 103
Figure 8.4 – Distribution made by summing two independents lognormal distributions with $\sigma_1 = 0.16$, $\mu_1 = -55.35$, $\sigma_2 = 1.1$ and $\mu_2 = -57.35$. 103
Figure 8.5. – Current deviation as a function of the trap position used in the Monte Carlo simulation, for V_{gs}=0.4 V. 104
Figure 8.6 – Comparison of the measured data distribution and the generated distribution using Monte Carlo simulations for, 10×10 µm^2 devices with V_{gs} = 0.4V. 104
Figure 8.7 – Current deviation as a function of the trap position used in the Monte Carlo simulation, for V_{gs}=1.2 V. 105

Figure 8.8 – Comparison of the measured data distribution and the generated distribution using Monte Carlo simulations, for 10×10 μm^2 devices with V_{gs} = 0.4V. 105
Figure 8.9 – Current deviation used in the Monte Carlo simulation for 8×1 μm^2 devices in 140-nm node with V_{gs}= 0.4 V and V_{ds}=1.8 V....106
Figure 8.10 – Comparison of the Q-Q plot of measured and simulated ln(S_{Id}/I_d^2), for 8×1 μm^2 devices in 140-nm node with V_{gs}= 0.4 V and V_{ds}=1.8 V....106
Figure 8.11 – Current deviation used in the Monte Carlo simulation for 8×0.14 μm^2 devices in 140-nm node with V_{gs}= 0.4 V and V_{ds}=0.1 V....106
Figure 8.12 – Comparison of the Q-Q plot of measured and simulated ln(S_{Id}/I_d^2), for 8×0.14 μm^2 devices in 140-nm node with V_{gs}= 0.4 V and V_{ds}=0.1 V. 106
Figure 8.13 – Current deviation used in the Monte Carlo simulation for 0.8×8 μm^2 devices in 140-nm node with V_{gs}= 1.8 V and V_{ds}=1.8 V....106
Figure 8.14 – Comparison of the Q-Q plot of measured and simulated ln(S_{Id}/I_d^2), for 0.8×8 μm^2 devices in 140-nm node with V_{gs}= 1.8 V and V_{ds}=1.8 V....106
Figure 8.15 – Q-Q plot of 43 measured devices with W×L=0.232×0.14 μm^2 and the Q-Q plot of 100000 Monte Carlo simulations with a constant trap density in energy of N_{tr}/γ = 1.5×10^9 cm^{-2}eV^{-1} and $\delta\tilde{I}_d$ = 2.8×10^{-13} cm^2 uniform from source to drain....107
Figure 8.16 – Q-Q plot of the MC simulation using a....108
Figure 8.17 – Distribution of the trap density in energy and the arbitrary Fermi-level used for the MC simulation of Figure 8.16. 108
Figure 8.18 – Resultant MC distribution after adding another set of traps with 4 times the trap density and δI_d 10 times smaller....109
Figure 8.19 – Monte Carlo distribution considering ΔI_d with a Weibull distribution with k_w=0.51....109
Figure 9.1 – EDGE Low Frequency Noise system [47]....111
Figure 9.2 – Schematic of the LFN test setup. (Adapted from [55])....112
Figure 9.3 – Roll-off frequency for 10×10 μm^2 n-channel devices with V_{gs}=0.9 V, V_{ds}=0.5 V, r_{ds} ≈14 KΩ and R_{load} =10 KΩ. 112
Figure 9.4 – Roll-off frequency smaller than 10 Hz. For n-channel devices with W×L = 8×30 μm^2, V_{gs}=1.8 V, V_{ds}=0.1 V, r_{ds} ≈13 KΩ and R_{load} =10 KΩ....112
Figure 9.5 – Noise floor of the low frequency noise measurement system [55]. 113
Figure 9.6 – Smoothing function applied to four 1×0.06 μm^2 n-channel device with V_{gs}=1.2 V, V_{ds}=0.5 V...114
Figure 9.7 – Smoothing function applied to a 10×10 μm^2 n-channel device with V_{gs}=1.2 V, V_{ds}=0.5 V.........114
Figure 9.8 – Estimation of the Expected value of a lognormal distribution using three different methods. 116
Figure 9.9 – Estimation of the Variance of a lognormal distribution using three different methods. 116
Figure 9.10 – Estimation of the Variance/mean^2 of a lognormal distribution using three different methods. .117
Figure 9.11 – Bootstrapping analysis of 50 observations using three different estimation methods for the expected value. 118
Figure 9.12 – Bootstrapping analysis of 50 observations using three different estimation methods for the variance....118
Figure 9.13 – Bootstrapping analysis of 50 observations using three different estimation methods for variance/mean^2. 119

LIST OF TABELS

Table 5.1 – Extracted Model Parameters for n-Channel Devices..59
Table 5.2 – Extracted Model Parameters for p-Channel Devices..59
Table 9.1 – Statistics of the lognormal distribution used in the Monte Carlo simulation. 115

LIST OF ABBREVIATIONS

CMOS	Complementary Metal Oxide Silicon
LFN	Low Frequency Noise
MC	Monte Carlo
MLE	Maximum Likelihood Estimator
MOS	Metal Oxide Silicon
NMOS	N-channel Metal Oxide Silicon
NMP	Nonradiative Multiphonon
PMOS	P-channel Metal Oxide Silicon
PSD	Power Spectrum Density
RTN	Random Telegraph Noise
RTS	Random Telegraph Signal
SNM	Static Noise Margin
SRAM	Static Random-Access Memory
SRH	Shockley-Read-Hall
STI	Shallow Trench Isolation
UMVUE	Uniformly Minimum Variance Unbiased Estimator

SUMMARY

1 INTRODUCTION 14

1.1 The Low Frequency Noise 14

1.2 LF Noise on Large Devices 15

1.3 LF Noise on Small Devices 16

1.4 Scaling of the Noise Variability with Device Area 17

1.5 Relevance of the LFN 19

2 A REVIEW ON LFN MODELS 21

2.1 The Random Telegraph Noise 21

2.2 McWorther's 1/*f* Model 24

2.3 Correlated Mobility Fluctuation 1/*f* Model 25

2.4 Hooge's 1/*f* Model 26

2.5 NMOS versus PMOS Discussion 27

3 DERIVING A STATISTICAL MODEL 29

3.1 Oxide defects as the LFN origin 29

3.2 Noise distribution 30

3.3 Expected Value and Variance 31

3.4 Expected Value Derivation 32

3.5 Variance Derivation 35

3.6 Monte Carlo Comparison 36

3.7 Derivation using SRH Model 38

4 MODELING THE CURRENT DEVIATION 40

4.1 The Charge Balance 40

4.2 Trap Impact on a Uniformly Inverted Channel ($V_{ds} \approx 0$V) 41

4.3 Carrier Number Fluctuation 42

4.4 Mobility Fluctuation 43

4.5 Correlated Carrier Number and Mobility Fluctuation 44

4.6 Trap Impact for a Non-uniformly Inverted Channel ($|V_{ds}| > 0$ V) 45

4.7 Trap Impact for Non-Uniformly Doped MOSFETs 46

4.8 Sources of the Current Deviation Variability 47

5 THE RTN STATISTICAL MODEL 49

Completing the Model 49

5.1 Models Comparison 50

5.2 The Uniformly Inverted Channel 51

5.3 Non-Uniformly Inverted Channel 59
5.4 n-Channel Versus p-Channel Devices 64
6 MODEL CALCULATION USING TCAD SIMULATIONS 66
6.1 TCAD Deck Calibration 66
6.2 Current Deviation Extraction Method 69
6.3 Current Deviation 72
6.4 Model Fit for n-channel devices in 140-nm node 77
6.5 Model Fit for p-channel devices in 140-nm node 81
6.6 Model Fit for n-channel devices in 40-nm node 85
6.7 Discussion 88
7 ANALYTICAL ANALYSIS & COMPACT MODELING 89
7.1 Uniformly doped devices 89
7.2 Halo-implanted Devices 93
7.3 The Three Transistors Model 99
8 DISCUSSIONS ON THE LFN DISTRIBUTION 102
8.1 Large area devices 102
8.2 Very small area devices 107
9 MEASUREMENT & DATA ANALYSIS 111
9.1 Low Frequency Noise Characterization 111
9.2 Lognormal Estimators 114
9.3 Bootstrapping 117
10 CONCLUSION 120
REFERENCES 121

1 INTRODUCTION

Low Frequency Noise (LFN) is a serious performance limiter in mixed signal CMOS circuits such as RF mixers, voltage-controlled oscillators (VCOs), and time-to-digital A/D converters. Moreover, Random Telegraph Noise (RTN) is emerging as a potential yield hazard in the most advanced CMOS nodes, as it can for instance appear as a time dependent Static Noise Margin (SNM) limiter in SRAMs (Agostinelli, et al., 2005) (Toh, 2009). Therefore, providing adequate models for LFN/RTN average value and variability is essential for circuit reliability.

1.1 The Low Frequency Noise

Mainly, there are three different behaviors of the noise in the low frequency domain of MOS devices. The power spectrum density (PSD) plot of Figure 1.1 shows two of these behaviors. At higher frequencies, the figure shows the white noise and at lower frequencies, it shows the flicker noise. The flicker noise is characterized by a 1/*f* or a pink spectrum behavior. Therefore, it is commonly named as 1/*f* noise or pink noise. In contrast, the white noise is characterized by its frequency independent behavior.

Figure 1.1 – Representation of the noise power spectral density of an arbitrary MOS transistor

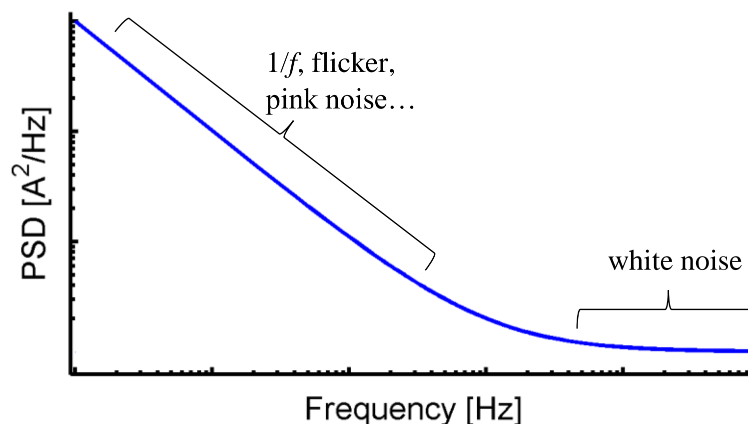

In addition to the flicker and white noise, it is also very common to see bumps on the noise spectra, as shown in

Figure 1.2. These bumps are the result of the prominence of the effect of individual defects in the device (Kirton & Uren, 1989).This effect adds Lorentzian-like spectrum (see Chapter 2) to the already existing noise PSD. This low frequency noise behavior is commonly referred to as Random Telegraph Noise (RTN) and it is often found on smaller devices (Hung, et al., 1990). On the analysis of the LFN of various different MOS devices it is common to see from almost perfect 1/*f* spectra (Section 1.2) to spectra that are totally dominated by Lorentzians (Section 1.3).

Figure 1.2 – Example of a bump present in the LFN spectrum.

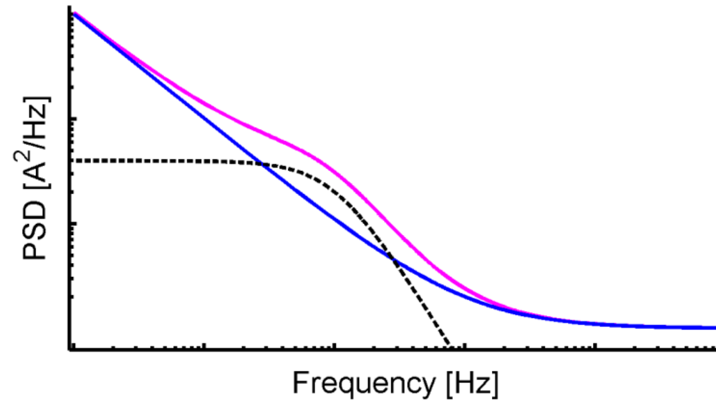

1.2 LF Noise on Large Devices

Figure 1.3 shows an example of the measured low frequency noise of a very large device with width (*W*) of 100 µm and length *(L)* of 8 µm on CMOS 140-nm technology. The noise spectrum in the figure shows a nice 1/*f* behavior. The notation S_{Id} is used to note that the measured power spectrum density of the noise is measured in the drain current of the devices.

Figure 1.3 – Example of the LFN of large devices with $WL = 100\times8\mu m^2$.

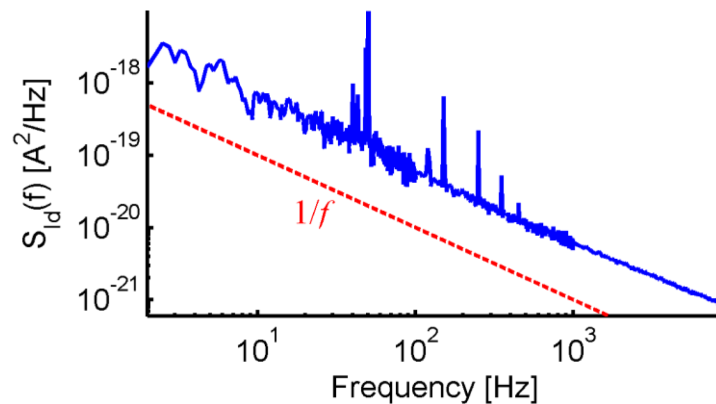

Figure 1.4 shows, from the noise measurement of 48 similar devices, that the noise variability for such large devices is small. Thus, the noise behaves more deterministically and is well-modeled using empirical models or using deterministic physics-based models – e.g. (McWhorter, 1957) and (Hung, et al., 1990).

Figure 1.4 – Noise spectra of 48 devices with $WL = 100\times8\mu m^2$.

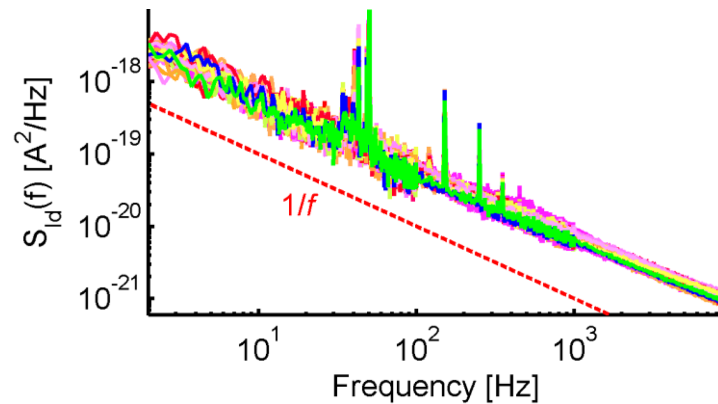

1.3 LF Noise on Small Devices

On small area devices, as shown in Figure 1.5, for three devices with $WL = 1\times0.06\mu m^2$ (CMOS 65-nm technology), the noise has a completely different behavior than on very large devices, which makes the models used to predict the noise of large devices unable to properly address the behavior of small devices. From Figure 1.5, even among three devices with the same area, each noise spectrum has a different frequency behavior and a different noise magnitude. This is a characteristic of the RTN caused by the effect of individual defects, each of which adds a Lorentzian to the noise spectrum.

Due to the difference between the noise spectra of large devices and small devices, some authors – e.g. (Kolhatkar, et al., 2003) – separate the analysis of the two noise behaviors and treat them as results of different effects. However, the findings of this work support the view in (Wirth, et al., 2009) and show that the noise can be modeled from the same effect for any device area.

Figure 1.5 – Example of 3 noise spectra of small devices with $WL = 1\times0.06\mu m^2$.

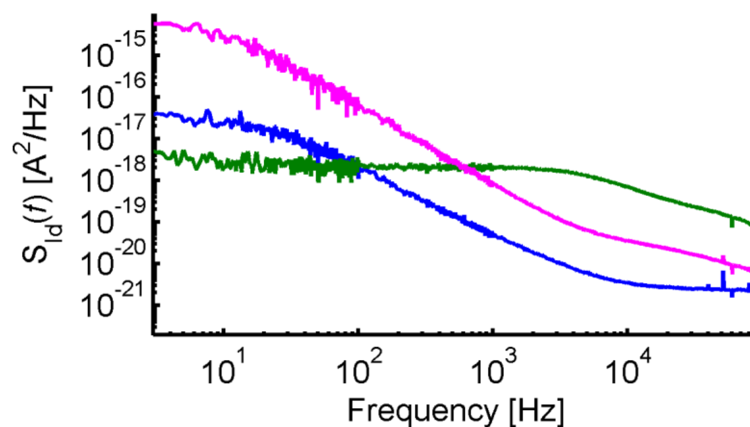

Figure 1.6 shows the noise measurement of 282 devices. As seen in the figure, the variability of such small devices is huge. Comparing, for a given frequency, the smallest noise magnitude with the largest noise magnitude there is a difference of almost four orders of magnitude. This large

variability imposes serious challenges on the usage of small devices in noise sensitive circuits. It also highlights the need to develop a stochastic model for such stochastic phenomena.

Figure 1.6 – Noise spectra of 282 devices with $WL = 1\times0.06\mu m^2$.

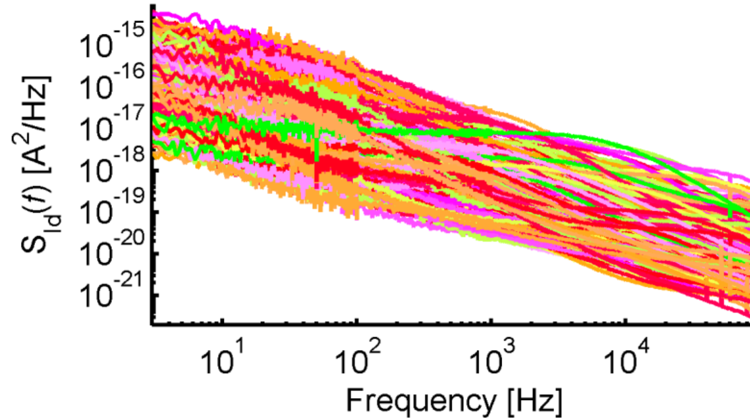

1.4 Scaling of the Noise Variability with Device Area

In this work, the useful quantity used to describe the variability of the LFN is the Standard Deviation of the natural logarithm of the noise, $\sigma[\log(S_{Id})]$. Sometimes, it will be only referred to as Standard Deviation or just variability. The reasons to use $\log(S_{Id})$ will become clearer along the work. However, considering that the LF noise quantity is usually analyzed in the logarithm domain, the calculation of $\sigma[\log(S_{Id})]$ should make the variability analysis easier and more meaningful.

The variability of the LFN power spectral density depends strongly on the gate area of MOSFETs (Ghibaudo & Roux-dit-Buisson, 1994). LFN variability studies – e.g., (Lopez, et al., 2011), (Ioannidis, et al., 2013) and (Ioannidis, et al., 2011) – generally propose an area scaling of the noise variability, $\sigma[\log(S_{Id})]$, based on a 1/√area dependency. Figure 1.7 shows that the variability indeed depends strongly on the device area. However, according to our measurements, present in the Figure 1.7, the variability does not follow the 1/√area dependency.

Figure 1.7 – Standard deviation of the logarithm of the noise for various device areas.

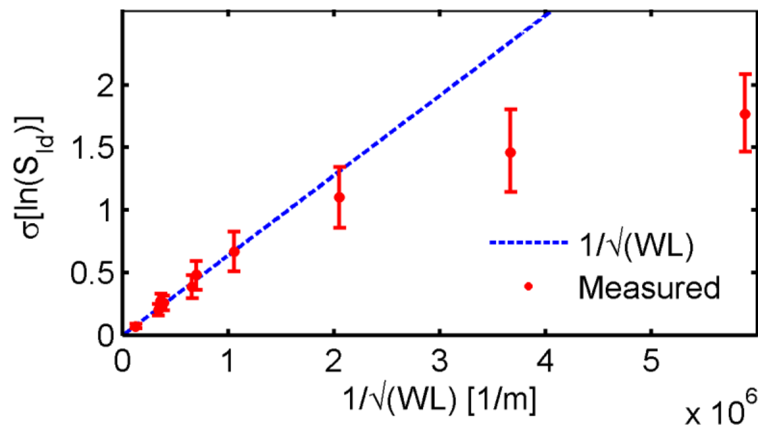

The work in (Yu, et al., 2012) reasons that LF noise variability deviates from the 1/√area dependency based on the statistics of sums of lognormal distributions, but eventually it relies on a rather arbitrary empirical function to fit the variability area scaling.

Other works – e.g. (Higashi, et al., 2014) and (Nour, et al., 2016) – attempt to describe the noise in a transistor by modeling the very complicated trapping and detrapping mechanism of every trap in a transistor. The resultant noise is then found trough transient and Monte Carlo simulations in which every time step of the simulation complex calculations are needed. Therefore, this method is very time demanding and it is dependent on trapping-detrapping mechanisms that are not thoroughly understood.

Since there is no satisfactory model that describes statistically the LFN from large devices to small devices and that could physically describe the scalability of the noise variability with the device area, in the following chapters of this work we are going to develop a new physics-based model. Using the model proposed in this work, we can better describe the statistic nature of the low frequency noise.

Remark

One could argue that the fitting of Figure 1.7 is not the best fitting possible, and that something as shown in Figure 1.8 is a better fitting. However, according to Pelgrom (Pelgrom, et al., 1989), hardly a physical mechanism that causes variability in the transistor parameter could create such behavior. Considering that the noise is given by two independent effects, each represented by a random variable (*A* and *B*). If the variance of *A* vanishes with the area, following the Pelgrom-behavior, so $\sigma_A^2 = \alpha/WL$ and the variance of *B* doesn't depend on the area due to distance variations in the wafer, so $\sigma_B^2 = \beta$, the standard deviation of the noise is calculated as

$$\sigma = \sqrt{\frac{\alpha}{WL} + \beta} \ , \qquad (1.1)$$

and at its highest slope the tangent of the curve described by (1.1) should point towards the origin in the $\sigma \times 1/\sqrt{WL}$ plot, as shown in Figure 1.9.

Figure 1.8 – Wrong method for fitting noise variability.

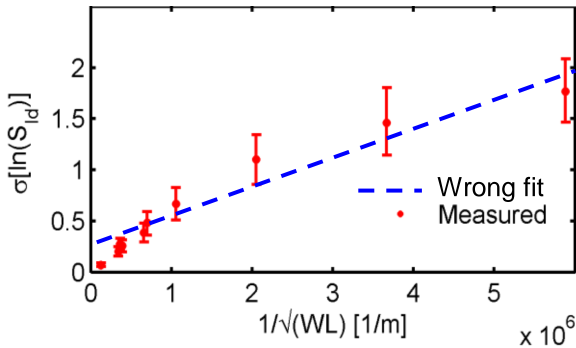

Figure 1.9 – Ideal Pelgrom behavior of the standard deviation.

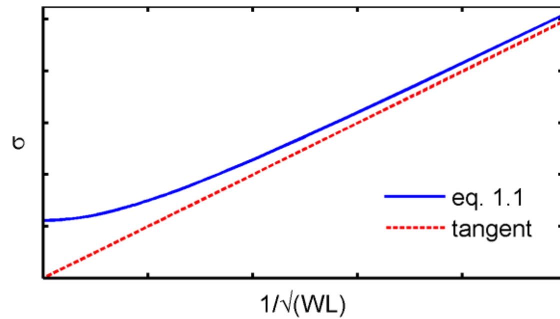

1.5 Relevance of the LFN

The most obvious application in which the low frequency noise can limit performance is in circuits with low frequency applications. An example of such low frequency systems are the audio amplifiers. Moreover, sensor networks are playing more and more role in several applications such as healthcare wearables, agriculture, and environment monitoring (Mainetti, et al., 2011). In many cases, the sensors are monitoring low frequency signals, such as bio-chemical signals and movements.

The LFN can also limit the performance of high frequency systems, due to the upconversion of the low frequency noise. The upconversion happens, for instance, in voltage-controlled oscillators (VCOs), causing phase noise. Phase noise can limit channel capacity and interfere in adjacent signals. This effect can pose a serious threat in the advance of wireless communication and in the advancement of the Internet of Things (IoT). As shown in Figure 1.10, the upconversion of the flicker noise results in the $1/f^3$ component, whereas the white noise results in the $1/f^2$ component.

Figure 1.10 – Upconversion of the LFN.

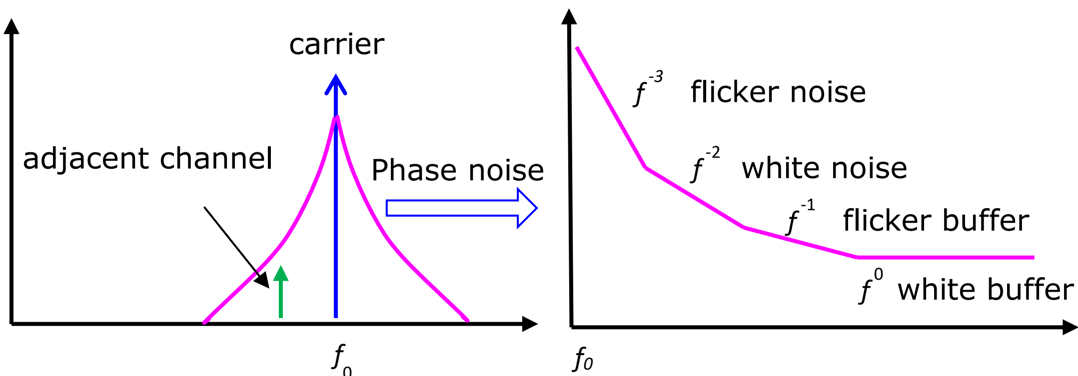

In the digital domain, the phase noise manifests itself as jitter. Jitter is an uncertainty in the period of the clock, as shown in Figure 1.11, and can cause timing violations in digital circuits.

Figure 1.11 – Period Jitter.

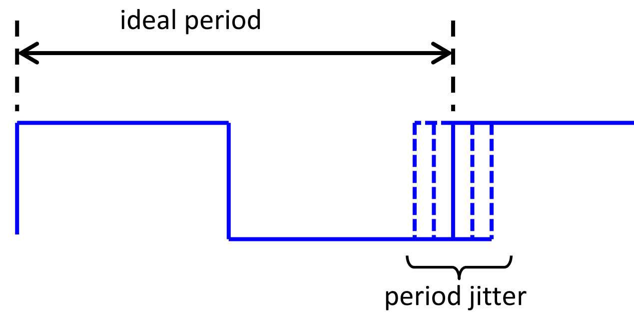

In very small area devices, Random Telegraph Noise (RTN) is emerging as a potential yield hazard, as it can for instance appear as a time dependent Static Noise Margin (SNM) limiter in SRAMs (Agostinelli, et al., 2005) (Toh, 2009), where the high current deviation present in such small devices can lead to read, write or data retention failures.

Works on the literature that try to understand and model the low frequency noise in MOSFET circuits exist as early as 1970s – e.g. (Christensson, et al., 1968), (Christensson & Lundström, 1968), (Berz, 1970) and (Fu & Sah, 1972) – and the LFN has been relevant since then. Nowadays, however, the relevance of the LFN has increased due to use of deeply scaled devices, use of lower supply voltages, and due to the popularization of wireless communication and sensor networks, among other factors. Conversely, present models are incapable of fully modeling the LFN characteristics in these devices. Therefore, LFN is not only a problem of the past but is also a problem of the present and a major issue for the near future.

2 A REVIEW ON LFN MODELS

2.1 The Random Telegraph Noise

The random telegraph noise (RTN) is characterized by the fluctuation of the drain current between two fixed levels with stochastic low- and high-level times, resembling a random telegraph signal (RTS), as shown in Figure 2.1.These fluctuations are mainly caused by a defect in the gate dielectric or at the dielectric-silicon interface (Kirton & Uren, 1989). These defects, or traps, are known to capture and release carriers from the channel. Therefore, the two current levels, between which the current fluctuates, represent the state of the trap (empty or occupied). In the case of an acceptor like trap (negatively charged when occupied by a carrier and neutral when not occupied) the current of an n-channel device decreases when the trap captures a carrier and returns to its highest level when the carrier is released back to the channel.

In the frequency domain, the RTN associated with a single trap is represented by a Lorentzian function. In the log-log domain, as shown in Figure 2.2, the Lorentzian is characterized by a plateau region and by a $1/f^2$ region.

Figure 2.1 – Illustration of the RTS given by the impact of a single defect in the oxide.

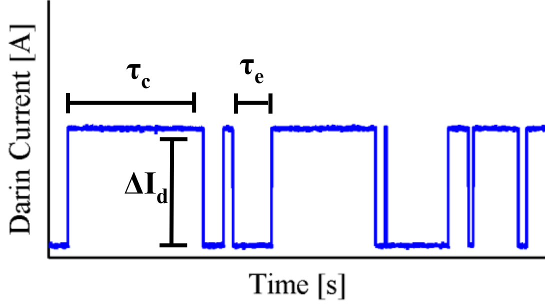

Figure 2.2 – Illustration of a RTN spectrum in log-log domain.

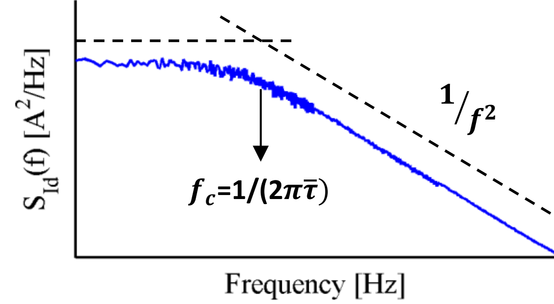

The power spectrum density (PSD) of the random telegraph noise, given by a single defect, is calculated as (Machlup, 1954)

$$S_{Id}(f) = \frac{4\Delta I_d^{\,2}}{(\overline{\tau}_e + \overline{\tau}_c)\left[\left(1/\overline{\tau}_e + 1/\overline{\tau}_c\right)^2 + \left(2\pi f\right)^2\right]}, \tag{2.1}$$

where $\overline{\tau}_e$ and $\overline{\tau}_c$ are the mean of the emissions and captures times respectively, and ΔI_d is the amplitude of the drain current fluctuation.

With some algebra, equation (2.1) can be rewritten as

$$S_{Id}(f) = 4\Delta I_d^2 \frac{\beta}{(1+\beta)^2} \frac{\overline{\tau}}{1+\overline{\tau}^2(2\pi f)^2}, \tag{2.2}$$

where $\beta = \frac{\overline{\tau}_e}{\overline{\tau}_c}$, $\frac{1}{\overline{\tau}} = \frac{1}{\overline{\tau}_e} + \frac{1}{\overline{\tau}_c}$ and, from detailed balance theory (degeneracy $g = 1$) (Ralls, et al., 1984), $\frac{\overline{\tau}_e}{\overline{\tau}_c} = e^{(E_F - E_T)/kT}$, where E_F, E_T , k and T are the Fermi energy, the trap energy, the Boltzmann constant and temperature respectively. In the form of (2.2), the Lorentzian formula evidently shows the plateau amplitude, given by $4\Delta I_d^2 \frac{\beta}{(1+\beta)^2}\overline{\tau}$, and the corner frequency of the Lorentzian (transition between the plateau and the $1/f^2$ region, 3dB drop), given by $f_c = 1/2\pi\overline{\tau}$.

Another characteristic of the RTN is the time taken for a trap to capture an emit a carrier, τ_c and τ_e respectively. For a given trap, τ_c and τ_e have an exponential distribution, where the average capture and emission times, $\overline{\tau}_c$ and $\overline{\tau}_e$, are unique proprieties of a trap. Figure 2.3 shows the measured emission times of a single trap (Kirton & Uren, 1989).

Figure 2.3 – Distribution of the emission time of a trap

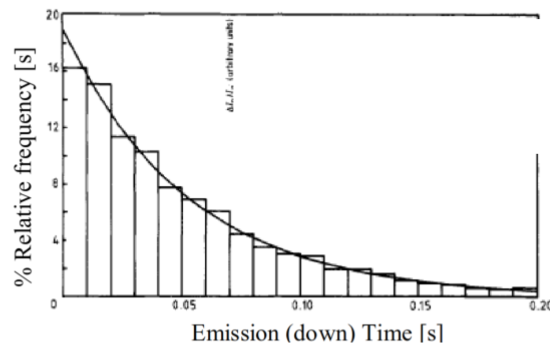

(Kirton & Uren, 1989)

The exponential distribution of the capture and emission times arises from the stochastic nature of the trap, which behaves as a regeneration-generation center (R-G centers). From Shockley-Read-Hall (SRH) model (Shockley & Read, 1952) (Hall, 1952) the possible transitions in R-G centers are: a) the capture of electrons from the conduction band, b) emission of an electron to conduction band, c) capture of a hole from valance band and d) emission of a hole to the valance band. In equilibrium and steady-state conditions, the average rate for these transitions are

$$\left.\frac{\partial n}{\partial t}\right|_{(a)} = \sigma_n \upsilon_{th} n \quad , \qquad \left.\frac{\partial n}{\partial t}\right|_{(b)} = \sigma_n \upsilon_{th} n_i e^{(E_T - E_i)/kT} ,$$
$$\left.\frac{\partial p}{\partial t}\right|_{(c)} = \sigma_p \upsilon_{th} p \quad \text{and} \quad \left.\frac{\partial p}{\partial t}\right|_{(d)} = \sigma_p \upsilon_{th} n_i e^{(E_i - E_T)/kT} , \tag{2.3}$$

where σ_n, σ_p, υ_{th}, n, p and n_i are the electron capture cross section, the hole capture cross section, the carrier thermal velocity, the electron concentration, the hole concentration, and the intrinsic concentration of electrons respectively.

Combining the average rates that a trap captures an electron – (a) and (d) – and combining the average rates that a trap releases an electron – (b) and (c) – results in

$$\begin{aligned} \frac{1}{\overline{\tau}_e} &= \upsilon_{th}(\sigma_p p + \sigma_n n_i e^{(E_T - E_i)/kT}) \\ \frac{1}{\overline{\tau}_c} &= \upsilon_{th}(\sigma_n n + \sigma_p n_i e^{(E_i - E_T)/kT}). \end{aligned} \tag{2.4}$$

Which gives

$$\beta = \frac{\overline{\tau}_e}{\overline{\tau}_c} = e^{(E_F - E_T)/kT} \tag{2.5}$$

and

$$\overline{\tau} = \overline{\tau}_c \frac{\beta}{\beta + 1} \ . \tag{2.6}$$

In a normal operation condition of a n-channel device, one can consider only the electrons capture rate. Therefore,

$$\overline{\tau}_c = \frac{1}{\sigma_n \upsilon_{th} n} \tag{2.7}$$

and

$$\overline{\tau} = \frac{1}{\sigma_n \upsilon_{th} n} \frac{\beta}{\beta + 1} \tag{2.8}$$

Bulk defects, depending on their nature, are known to have defined energies and defined cross sections due to the crystalline nature of the semiconductor. Therefore, it is not believed that they could be the responsible for Lorentzians with such different population of time constants (Kirton & Uren, 1989), as shown in Figure 1.6. Thus, it is believed that defects in the gate dielectric or at its interface are responsible for such noise behavior, where the amorphous nature of the dielectric allows a wide distribution of defect energy and cross section.

The exact nature of the wide distribution of cross sections are unknown. Nevertheless, many different theories are present in the literature. The tunneling theory correlates the position of the defect inside the dielectric with its cross section, by which the trap time constant can be approximated as (McWhorter, 1957)

$$\overline{\tau} \propto \frac{1}{\sigma_n} \propto e^{\gamma_a z} , \tag{2.9}$$

where γ_a is the wave function attenuation constant and z is the trap distance from the interface. Another theory proposes a nonradiative multiphonon (NMP) capture cross section, in which the trap

cross section is proportional to an activation energy and that a wide distribution of such energies is responsible for the distribution of $\overline{\tau}$. According to this theory (Kirton & Uren, 1989)

$$\sigma_n = \sigma_0 e^{-E_B/kT}, \quad (2.10)$$

where σ_0 is the cross section pre-factor that can include information about the tunnel interaction given by (2.9)and other gate voltage dependencies of the transitions (Palma, et al., 1997).

Other works on the literature – e.g. (Grasser, 2012) and (Grasser, et al., 2009) – propose more complex theories to explain the capture and emission mechanisms of a trap. These works extend the NMP model to account for metastable defect configurations, where after a capture or before an emission the trap changes to metastable states generating different electric field and temperature dependencies.

2.2 McWorther's 1/*f* Model

The McWorther model (McWhorter, 1957), also known as the carrier number fluctuation model, considers the flicker noise as a result of interactions between traps in the oxide and the carriers in the channel, as described in Section 2.1. According to the model the power spectral density of the mean-square fluctuations in the number of occupied traps over an elemental volume is given by

$$S_{\Delta v \delta N_t} = 4N_t(x,y,z,E)f_t(1-f_t)\frac{\tau(x,y,z,E)}{1+\omega^2\tau(x,y,z,E)^2}\Delta\upsilon, \quad (2.11)$$

where $N_t(x,y,z,E)$ is the trap density in the oxide and in the energy, $\tau(x,y,z,E)$ is the trap time constant, $f_t = [1+\exp((E-E_f)/kT)]^{-1}$ and $\omega = 2\pi f$ the angular frequency. In our case, the elemental volume $\Delta\upsilon$ is given by $\Delta\upsilon = \Delta x dydz$.

The total PSD of the fluctuations in the number of occupied traps in a section of the device with area equal to $W\Delta x$ is given by the summation of all the traps that contribute to the noise in this area, where $\Delta N_t = \Delta x W N_t$. Therefore,

$$S_{\Delta N_t}(x,f) = \int_{E_v}^{E_c}\int_0^W\int_0^{T_{ox}} 4N_t(x,y,z,E)f_t(1-f_t)\frac{\tau(x,y,z,E)}{1+\omega^2\tau(x,y,z,E)^2}\Delta x dz dy dE \quad (2.12)$$

In the evaluation of (2.12) two assumptions are made: 1) the trap density has a uniform spatial distribution in the oxide near the interface. Hence, $N_t(x,y,z,E) = N_t(E)$ and 2) the trap time constant is given by the tunneling theory, in which

$$\tau = \tau_0 e^{\gamma_a z}, \quad (2.13)$$

where γ_a is the attenuation factor of the electron wave function in the oxide. For a Si-SiO_2 interface, the electron tunneling theory predicts that $\gamma_a=10^8$ cm^{-1} (McWhorter, 1957). Since $f_t(1-f_t)$ behaves like a delta function around the quasi-Fermi level with area equal to kT, the integral in (2.12) results in

$$S_{\Delta N_t}(x,f)=N_t(E_{fn,fp})\frac{kTW\Delta x}{\gamma_a f} \tag{2.14}$$

From the number fluctuation model, the fluctuations of occupied traps induce a fluctuation on the carrier's density, which in turn cause fluctuation on the drain current. Local fluctuations on the drain current of a section of the channel with width W and length Δx, are calculated as

$$\delta I_d=\frac{I_d}{\Delta N}\delta\Delta N\,, \tag{2.15}$$

where $\Delta N=W\Delta xN$. In the original derivation in, McWorther (1957) considered that $\delta\Delta N\approx\delta\Delta N_t$, which is a good simplification in the strong inversion. Reimbold *et al.* (1984) derived a more complete relation in which the trapped charge not only impacts the inversion layer charge but it also impacts the depletion charges and the trapped charges (Reimbold, 1984). Therefore,

$$\frac{\delta N}{\delta N_t}=\frac{C_{inv}}{C_{inv}+C_{ox}+C_d+C_{it}}\,. \tag{2.16}$$

Now (2.15) can be written as

$$\delta I_d=\frac{I_d}{W\Delta xN}\left(\frac{\delta N}{\delta N_t}\right)\delta\Delta N_t\ , \tag{2.17}$$

and the power spectral density of the local current fluctuation is

$$S_{\Delta Id}(x,f)=\left(\frac{I_d}{W\Delta x}\frac{1}{N}\right)^2\left(\frac{\delta N}{\delta N_t}\right)^2 S_{\Delta N_t}(x,f)\ . \tag{2.18}$$

Finally, using Klaassen and Prins (Klaassen & Prins, 1967) and replacing (2.14) in (2.18) we have

$$S_{Id}(f)=\frac{1}{L}\int_0^L S_{\Delta Id}\Delta x dx=\frac{kT}{\gamma_a f}\frac{I_d^2}{WL^2}\int_0^L N_t(E_{fn})\left(\frac{\eta}{N}\right)^2 dx\,, \tag{2.19}$$

with $\eta=\dfrac{\delta N}{\delta N_t}=\dfrac{C_{inv}}{C_{inv}+C_{ox}+C_d+C_{it}}$.

2.3 Correlated Mobility Fluctuation 1/*f* Model

The correlated mobility fluctuation extends the carrier number fluctuation theory to account for the Coulomb scattering of free charge carriers at the vicinity of the trapped oxide charge (Hung,

et al., 1990). As a consequence, the trapped carrier will not only cause a fluctuation on the free carrier number but will also cause a fluctuation on the mobility. This model is widely used in modern compact models such as BSIM (Chauhan, et al., 2013) and PSP (Li, et al., 2008) models.

According to the correlated mobility model, fluctuations on the drain current of a section of the channel with width W and length Δx, are calculated as (Hung, et al., 1990)

$$\delta I_d = I_d \left(\frac{1}{\Delta N} \frac{\delta \Delta N}{\delta \Delta N_t} \pm \frac{1}{\mu_{eff}} \frac{\delta \mu_{eff}}{\delta \Delta N_t} \right) \delta \Delta N_t, \tag{2.20}$$

The next step to derive this model is to find the value of $\delta\mu_{eff}/\delta\Delta N_t$, using Mathiessen's rule

$$\frac{1}{\mu_{eff}} = \frac{1}{\mu_n} + \frac{1}{\mu_{ox}} = \frac{1}{\mu_n} + \alpha N_t, \tag{2.21}$$

where μ_{ox} is the mobility limited by oxide charge scattering, one can show that

$$\frac{\delta \mu_{eff}}{\delta \Delta N_t} = \frac{\alpha \mu_{eff}^2}{W \Delta x}. \tag{2.22}$$

Using (2.22) in (2.20) the expression of the fluctuation on the drain current becomes

$$\delta I_d = I_d \left(\frac{\eta}{\Delta N} \pm \alpha \mu_{eff} \right) \frac{\delta \Delta N_t}{W \Delta x}. \tag{2.23}$$

Finally, the power spectral density of the mean-square fluctuations in the drain current is

$$S_{Id}(f) = \frac{kT}{\gamma_a f} \frac{I_d^2}{WL^2} \int_0^L N_t(E_{fn}) \left(\frac{\eta}{N} \pm \alpha \mu_{eff} \right)^2 dx \tag{2.24}$$

2.4 Hooge's 1/*f* Model

Hooge's model considers the flicker noise is a result of fluctuation in the bulk mobility caused by phonon scattering (Hooge & Vandamme, 1978). According to Hooge's model, the drain current noise is given by the following empirical equation:

$$S_{Id} = \frac{I_d^2 \alpha_H}{fWLN}, \tag{2.25}$$

where α_H is Hooge's empirical parameter, f the frequency and N the carrier density.

Equation (2.25) is only valid when the carrier density is uniform across the channel. Therefore, to account for the noise with large drain bias applied the channel can be divided into infinitesimal uniform segments and the total noise is evaluated by

$$S_{Id} = \frac{I_d^2 \alpha_H}{fWL^2} \int_0^L \frac{dx}{N(x)} \tag{2.26}$$

For bulk devices, the α_H parameter was found to have a constant value of about 2×10^{-3} (Hooge & Vandamme, 1978). However, for MOS devices α_H is found to be several orders of magnitude below this value. Nevertheless, to explain the discrepancy between measurements and the expected noise using (2.25) a bias dependence of α_H is often used, which apparently contradicts Hooge's theory (Hung, et al., 1990). Despite this discrepancy, there are still authors that argue in favor of Hooge's model, especially when modeling the 1/*f* noise of PMOS devices – e.g. (Vandamme, et al., 1994).

Figure 2.4 shows a comparison among the three flicker noise models, calculated for a NMOS transistor with T_{ox} = 3 nm, V_{th}=0.5 V, $N_t = 1.7\times10^{17}$ cm^{-3}eV^{-1}.

Figure 2.4 – Comparison among three flicker noise models.

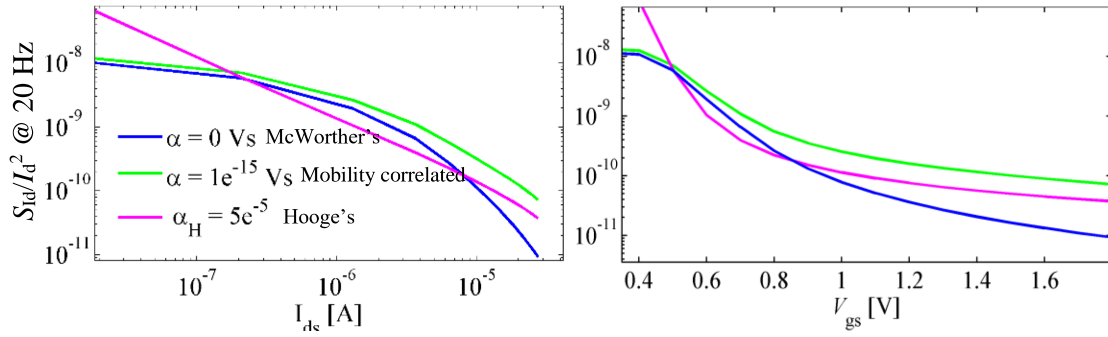

2.5 NMOS versus PMOS Discussion

Figure 2.5 shows an example of the noise power spectral density for both NMOS and PMOS devices (140-nm node, $W\times L$ = 8×1μm^2), measured at 20Hz for different gate bias and V_{ds} = 0.1V. Analyzing the noise in the figure one can clearly see that the noise of PMOS device has a weaker dependence with gate bias than the NMOS device.

To explain this difference, many authors along the years have considered that the origin of the noise in PMOS devices is given by the phonon scattering theory (Hooge's model) whereas the noise of NMOS devices has an origin in interface defects (Mcworther's model). To understand this view, one can use the calculation of carrier density at strong inversion, given by $C_{ox}(V_{gs}-V_T)/q$ (where C_{ox} is the oxide capacitance, V_T the threshold voltage and q the electron charge), then for a small drain bias (2.19) and (2.25) become

$$S_{Id,McWorther}(f)=\frac{kT}{\gamma_a f}\frac{I_d^2}{WL}N_t(E_{fn})\frac{q}{C_{ox}^2(V_{gs}-V_{th})^2} \tag{2.27}$$

and

$$S_{Id,Hooge}(f)=\frac{I_d^2\alpha_H q}{fWLC_{ox}(V_{gs}-V_{th})}\ . \tag{2.28}$$

Equation (2.27) is inversely dependent on the square of V_{gs} while (2.28) is only inversely dependent on V_{gs}. Therefore, this difference for some authors in the past was a clear evidence that PMOS and NMOS devices have different noise origins.

Figure 2.5 – Difference between the noise behavior of NMOS and PMOS devices.

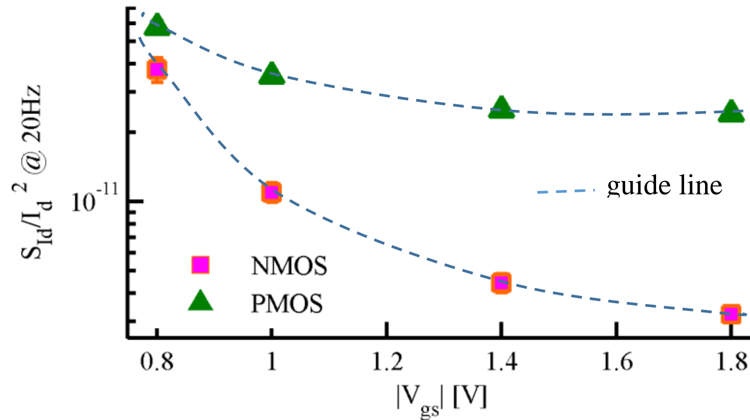

With the introduction of the mobility correlated model (Hung, et al., 1990), the fitting of the noise of both PMOS and NMOS was possible by just adjusting the α and N_t parameters. However, if it is assumed that the trap density is constant as a function of the energy the α parameter assumes unphysical values for PMOS devices. Therefore, the discussion about the origins of the noise has continued, with some authors – e.g. (Scofield, et al., 1994) – arguing in defense of a varying trap density with energy for the PMOS devices while others – e.g (Vandamme, et al., 1994) – arguing for a phonon scattering mechanism to explain the noise of PMOS device.

In this work, using our proposed model and analyzing the Expected value, Variance and noise variability we show strong evidences in favor of the varying trap density viewpoint and that the noise origin from interface defects for both NMOS and PMOS devices.

3 DERIVING A STATISTICAL MODEL

3.1 Oxide defects as the LFN origin

In this work, the low frequency noise is treated as a consequence of the capture and emission of channel carriers from multiple oxide defects (or traps). The noise of multiple defects in the oxide is derived by discrete summation of the noise of each individual defect (assuming that they are uncorrelated), resulting in

$$S_{Id}(\omega) = 4\sum_{i=1}^{N_{tot}} \Delta I_i^2 \frac{\beta_i}{(1+\beta_i)^2} \frac{\overline{\tau}_i}{1+\overline{\tau}_i^2\omega^2}, \tag{3.1}$$

where N_{tot} is the total number of traps in the device oxide.

When the characteristic time constant ($\overline{\tau}$) of the traps in a transistor is log-uniform distributed, in other words, when the corner frequency of individual Lorentzians are uniformly distributed in the log-scale, the total noise in the transistor will have a 1/*f* behavior, as shown in the Figure 3.1.

Figure 3.1 – Illustration of the noise given by the summation of traps with log-uniformly distributed time constants.

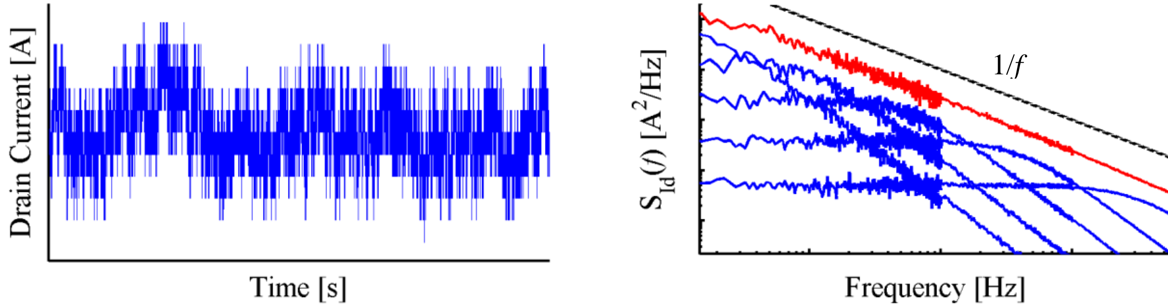

Figure 3.2 shows the average of the noise spectra previously shown in Figure 1.6. The figure demonstrates that the average of such large amount of spectra, formed by well-defined Lorentzians, has a 1/*f* behavior. This observation, combined with studies as for instance reported in (Wirth, et al., 2009) and (Scholten, et al., 2003), supports our fundamental assumption that RTN effects dominate the LFN behavior and that $\overline{\tau}$ is indeed log-uniform distributed. Therefore, the RTN and the 1/*f* noise should be treated in a single model to describe the LFN variability. In addition, if the traps are uniformly distributed over the entire transistor area, this implicates that large area devices have many traps and have a LFN with a 1/*f* behavior, and that small area devices have few traps and have a LFN with a Lorentzian behavior.

Figure 3.2 – Average of the noise spectra of a small area device.

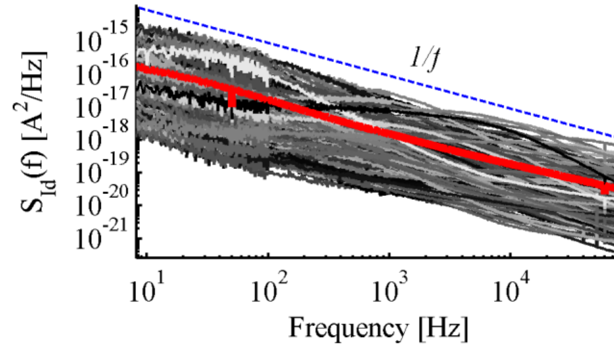

3.2 Noise distribution

According to our measurements, shown in Figure 3.3, the noise could be well described by a lognormal distribution for different device sizes. Other works in the literature already point that the noise distribution is lognormal (Lopez, et al., 2011) (Ioannidis, et al., 2011) (Srinivasan & Dey, 2012). However, for the first time this noise distribution characteristic is used to build a statistical LFN model.

Figure 3.3 – Noise distribution for three different devices' area.

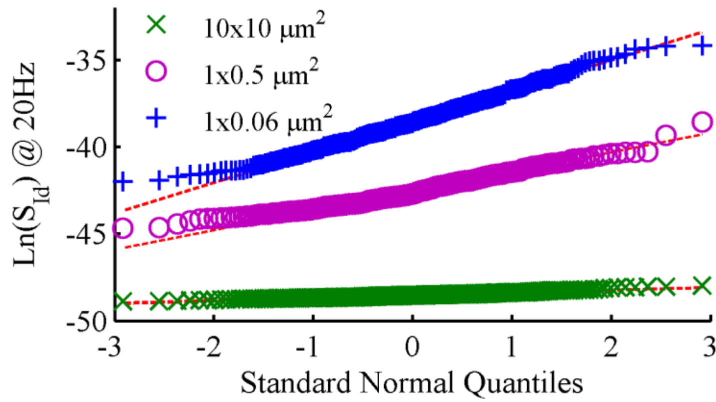

Using general statistics of the lognormal distribution, found in statistics textbooks (Johnson, et al., 1994), to calculate the standard deviation of the natural logarithm of the noise one has that

$$\sigma\left[\ln\left(S_{id}(f)\right)\right]=\sqrt{\ln\left(1+\frac{\mathrm{Var}\left[S_{Id}(f)\right]}{\mathrm{E}\left[S_{Id}(f)\right]^2}\right)}, \tag{3.2}$$

and the average of the natural logarithm of the noise is

$$\mu\left[\ln\left(S_{id}(f)\right)\right]=\ln\left(\mathrm{E}\left[S_{Id}(f)\right]\right)-\frac{1}{2}\sigma\left[\ln\left(S_{id}\right)\right]^2. \tag{3.3}$$

Equation (3.2) will be the key equation for deriving our model. We demonstrate, using (3.2) and (3.3), along this work that our model is useful to calculate and predict the envelope of the RTN/LFN noise (e.g. $\mu \pm 3\sigma$), as shown in the Figure 3.4.

Figure 3.4 – Example of the Noise Variability Model prediction.

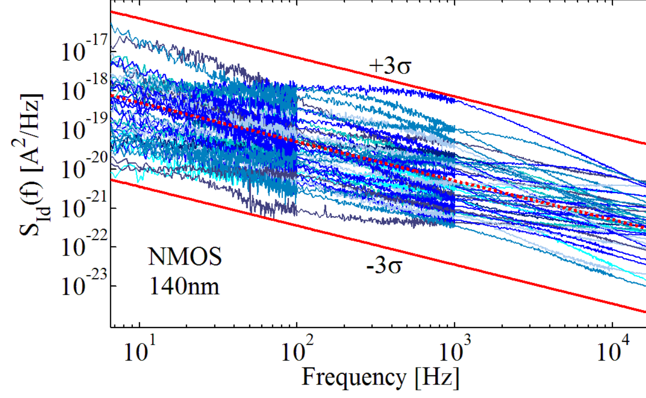

Therefore, the next two important quantities to calculate are the Expected value, $\mathrm{E}\left[S_{Id}(f)\right]$, and the Variance, $\mathrm{Var}\left[S_{Id}(f)\right]$, of the noise.

3.3 Expected Value and Variance

From our first key assumption in Section 3.1, that the LFN is given by the summation of Lorentzians and it is described by (3.1), we can calculate the Expected value and the Variance of the noise. To accomplish it, the parameters in the equation are treated as random variables. A complete derivation of the Expected value and the Variance is given in Section 3.4 and 3.5. However, the key assumptions for the derivation are:

- $\overline{\tau}$ is log-uniform distributed.
- The total number of traps in a transistor, N_{tot}, is Poisson distributed with mean equal to $N_{tr} \times WL$ and N_{tr} is the trap density.
- $\dfrac{\beta}{(1+\beta)^2}$ can be approximate by a delta function, at energy equal to E_F, multiplied by kT. Therefore, there is no need to assume any particular distribution for E_T.
- ΔI_d is a random variable dependent on the random position of the trap along the channel (X_T). However, as discussed later, the trap position is not the only source of ΔI_d variability and the expectation of ΔI_d is given by the law of total expectation: $\mathrm{E}[\Delta I_d] = \mathrm{E}[\mathrm{E}[\Delta I_d|X_T]]$, where, $\mathrm{E}[\Delta I_d|X_T]$ is the conditional expectation of ΔI_d dependent on the value of the random variable X_T.
- X_T is uniformly distributed along the channel.

From Section 3.4, the Expected of the LF noise is

$$\mathrm{E}\left[S_{Id}(f)\right]=\frac{kT}{f}\frac{I_d^2}{WL}\mathrm{E}\left[\Delta\tilde{I}_d^2\frac{N_{tr}(E_{Fn})}{\gamma}\right]$$

or

$$\mathrm{E}\left[S_{Id}(f)\right]=\frac{kT}{f}\frac{I_d^2}{WL^2}\int_0^L \mathrm{E}\left[\Delta\tilde{I}_d^2|X_T=x\right]\frac{N_{tr}(E_{Fn})}{\gamma}dx \tag{3.4}$$

and, from Section 3.5, the Variance is

$$\mathrm{Var}\left[S_{Id}(f)\right]=\frac{kT}{3\pi^2 f^2}\frac{I_d^4}{W^3L^3}\mathrm{E}\left[\Delta\tilde{I}_d^4\frac{N_{tr}(E_{Fn})}{\gamma}\right]$$

or

$$\mathrm{Var}\left[S_{Id}(f)\right]=\frac{kT}{3\pi^2 f^2}\frac{I_d^4}{W^3L^4}\int_0^L \mathrm{E}\left[\Delta\tilde{I}_d^4|X_T=x\right]\frac{N_{tr}(E_{Fn})}{\gamma}dx. \tag{3.5}$$

Normalizing the Variance by the square of the Expected value we have

$$\frac{\mathrm{Var}\left[S_{Id}(f)\right]}{\mathrm{E}\left[S_{Id}(f)\right]^2}=\frac{1}{3\pi^2 kT}\frac{\gamma}{W}\frac{\int_0^L \mathrm{E}\left[\Delta\tilde{I}_d^4|X_T=x\right]N_{tr}(E_F)dx}{\left(\int_0^L \mathrm{E}\left[\Delta\tilde{I}_d^2|X_T=x\right]N_{tr}(E_F)dx\right)^2}, \tag{3.6}$$

where $\Delta\tilde{I}_d = \Delta I_d WL/I_d$ is the normalized current deviation, $N_{tr}(E_T)$ is the trap density as a function of the quasi-Fermi level [$cm^{-2}eV^{-1}$] and $\gamma = \ln(\bar{\tau}_{max}/\bar{\tau}_{min})$. γ is a unitless constant that describes the density of traps in the log scale of time constants. Therefore, it is more meaningful to refer to the trap density as N_{tr}/γ per cm^2 per eV per neper. In this work, when we refer to trap density we will always be referring to the N_{tr}/γ quantity.

The normalized Variance ($\mathrm{Var}[S_{Id}]/\mathrm{E}[S_{Id}]^2$), described by (3.6) is used to calculate the standard deviation of the noise in (3.2). From (3.4) – (3.6), the last quantity to calculate, to have the full derivation of our LFN statistical model, is the statistic of the current deviation (ΔI_d). This statistic is derived in Chapter 4.

3.4 Expected Value Derivation

The calculation of the Expected value, $\mathrm{E}[S_{Id}(f)]$, and the Variance of the LF noise, $\mathrm{Var}[S_{Id}(f)]$, is done using equation (3.1) in which E_T, X_T, $\bar{\tau}$ and ΔI_d are properties of each trap and are random variables. It is also necessary to consider that the total number of traps, N_{tot}, in a transistor is also a random variable. Using the law of total expectation, $\mathrm{E}[Y] = \mathrm{E}[\mathrm{E}[Y|N]]$, one has that

$$\mathrm{E}\left[\sum_{i=1}^{N} X_i\right]=\mathrm{E}\left[\mathrm{E}\left[\sum_{i=1}^{N} X_i|N\right]\right]=\mathrm{E}\left[N\,\mathrm{E}\left[X\right]\right]. \tag{3.7}$$

For N and X independents,

$$E\left[\sum_{i=1}^{N} X_i\right] = E[N]E[X].$$

Therefore, the Expected value of the noise described in equation (3.1) is

$$\mathrm{E}[S_{Id}(\omega)] = 4\,\mathrm{E}[N_{tot}]\mathrm{E}\left[\Delta I^2 \frac{\beta}{(1+\beta)^2}\frac{\bar{\tau}}{1+\bar{\tau}^2\omega^2}\right]. \quad (3.8)$$

The expected value of a measurable function of X is given by: $\mathrm{E}[g(x)] = \int_{-\infty}^{\infty} g(x) f_x dx$, where f_x is the probability density function of X. Using this, one has that the Expected value of the LFN is

$$\mathrm{E}[S_{Id}(\omega)] = 4\,\mathrm{E}[N_{tot}]\int_0^{\infty}\int_{\tau_{\min}}^{\tau_{\max}}\int_0^{\infty} \Delta I_d^2 \frac{\beta}{(1+\beta)^2}\frac{\bar{\tau}}{1+\bar{\tau}^2\omega^2} f_{E_T} f_{\bar{\tau}} f_{\Delta I_d} dE_T d\bar{\tau} d\Delta I_d, \quad (3.9)$$

where f_{Et}, f_{τ} and $f_{\Delta Id}$ are the probability density function of the traps' energy, time constant and current deviation respectively

Figure 3.5 shows the behavior of $\beta/(1+\beta)^2$ as a function of the trap energy (remembering that $\beta = e^{(E_F - E_T)/kT}$). From the figure, the behavior of $\beta/(1+\beta)^2$ can be approximated as a delta function at $E_T = E_F$, with an area equal to

$$\int_0^{\infty} \frac{\beta}{(1+\beta)^2} dE_T = -kT\int_{\infty}^{0} \frac{\beta}{(1+\beta)^2}\frac{1}{\beta} d\beta = kT \ .$$

Therefore, $\beta/(1+\beta)^2 \approx kT\delta(E - E_F)$ and (3.9) becomes

$$\mathrm{E}[S_{Id}(\omega)] = 4kT\,\mathrm{E}[N_{tot}]\int_0^{\infty}\int_{\tau_{\min}}^{\tau_{\max}} \Delta I_d^2 \frac{\bar{\tau}}{1+\bar{\tau}^2\omega^2} f_{E_T}(E_F) f_{\bar{\tau}} f_{\Delta I_d} d\bar{\tau} d\Delta I_d \ . \quad (3.10)$$

Figure 3.5 – Plot of $\beta/(\beta+1)^2$ as a function of the trap energy, for $E_F = 0.75$ V.

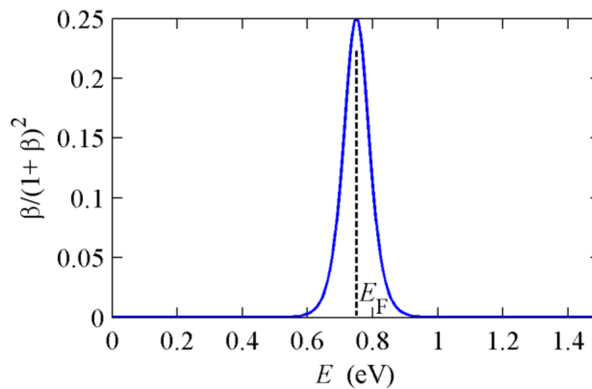

As ΔI_d is independent of $\bar{\tau}$, one can solve separately

$$\mathrm{E}\left[\frac{\bar{\tau}}{1+\bar{\tau}^2\omega^2}\right]=\int_{\tau_{\min}}^{\tau_{\max}}\frac{\bar{\tau}}{1+\bar{\tau}^2\omega^2}f_{\bar{\tau}}d\bar{\tau}\,. \tag{3.11}$$

Considering that $\bar{\tau}$ is a log-uniform distributed random variable in an arbitrary interval between $\bar{\tau}_{\min}$ and $\bar{\tau}_{\max}$ (where $\bar{\tau}_{\min} << 1/\omega << \bar{\tau}_{\max}$) that contains a total number of trap given by N_{tot}, the probability density function of $\bar{\tau}$ is $f_{\bar{\tau}} = 1/\gamma\bar{\tau}$, with $\gamma = \ln(\bar{\tau}_{\max}/\bar{\tau}_{\min})$. Solving equation (3.11) with $f_{\bar{\tau}} = 1/\gamma\bar{\tau}$ one has

$$\mathrm{E}\left[\frac{\bar{\tau}}{1+\bar{\tau}^2\omega^2}\right]=\frac{1}{\gamma\omega}\left(\arctan\left(\bar{\tau}_{\max}\omega\right)-\arctan\left(\bar{\tau}_{\min}\omega\right)\right)\,. \tag{3.12}$$

For an observation window where $\bar{\tau}_{\min} << 1/\omega << \bar{\tau}_{\max}$, the Expected value is simplified to

$$\mathrm{E}\left[S_{Id}(\omega)\right]=4\,\mathrm{E}\left[N_{tot}\right]\mathrm{E}\left[\Delta I^2 f_{E_T}(E_F)\right]\frac{1}{\gamma\omega}\frac{\pi}{2}, \tag{3.13}$$

or

$$\mathrm{E}\left[S_{Id}(f)\right]=\frac{1}{\gamma f}\mathrm{E}[N_{tot}]\mathrm{E}\left[\Delta I^2 f_{E_T}(E_F)\right]. \tag{3.14}$$

Considering that N_{tot} is Poisson distributed with mean equal to $N'_{tr}WL$, where N'_{tr} is the trap density per cm^2, the Expected value is calculated as

$$\mathrm{E}\left[S_{Id}(f)\right]=\frac{N'_{tr}WL}{\gamma f}\mathrm{E}\left[\Delta I^2 f_{E_T}(E_F)\right]. \tag{3.15}$$

Now, consider that the distribution of ΔI_{d} is dependent on the random position of the trap along the length of the channel (X_{T}) and it is also subject to other random factors, so

$$\mathrm{E}\left[\Delta I^2\right]=\mathrm{E}\left[\mathrm{E}\left[\Delta I_d^2\middle|X_T\right]\right],$$

and,

$$\mathrm{E}\left[\Delta I^2 f_{E_T}(E_{Fn})\right]=\mathrm{E}\left[\mathrm{E}\left[\Delta I_d^2\middle|X_T\right]f_{E_T}(E_{Fn})\right]. \tag{3.16}$$

Consider, also, that the traps are uniformly distributed in the channel, $f_{X_T}=1/L$, so now

$$\mathrm{E}\left[\Delta I^2 f_{E_T}(E_{Fn})\right]=\frac{kT}{L}\int_0^L\mathrm{E}\left[\Delta I_d^2\middle|X_T=x\right]f_{E_T}(E_{Fn})dx\,. \tag{3.17}$$

Substituting equation (3.17) into (3.15) and using $N'_{tr}f_{\text{ET}}(E_{\text{F}})/\gamma = N_{\text{tr}}(E_{\text{F}})/\gamma$, the trap density per cm^2 per eV,

$$\mathrm{E}\left[S_{Id}(f)\right]=\frac{kT}{f}W\int_0^L\mathrm{E}\left[\Delta I_d^2\middle|X_T=x\right]N_{tr}(E_{Fn})/\gamma dx\,. \tag{3.18}$$

Finally, normalizing ΔI_d, so $\Delta\tilde{I}_d = \frac{WL}{I_d}\Delta I_d$, the Expected value of the LFN is given by (3.4).

$$\text{(3.4):}\quad \mathrm{E}\left[S_{Id}(f)\right] = \frac{kT}{f}\frac{I_d^2}{WL^2}\int_0^L \mathrm{E}\left[\Delta\tilde{I}_d^2 \middle| X_T = x\right]\frac{N_{tr}(E_{Fn})}{\gamma}dx .$$

3.5 Variance Derivation

To take into account that the traps' proprieties (E_T, X_T, $\overline{\tau}$ and ΔI_d) and N_{tot} are random variables, the variance of (3.1) is calculated using the law of total variance,

$$\mathrm{Var}\left[Y\right] = \mathrm{E}\left[\mathrm{Var}\left[Y \middle| N\right]\right] + \mathrm{Var}\left[\mathrm{E}\left[Y \middle| N\right]\right] . \tag{3.19}$$

Hence, the variance of the random sum of a random variable is:

$$\mathrm{Var}\left[\sum_i^N X_i\right] = \mathrm{E}\left[\mathrm{Var}\left[\sum_i^N X_i \middle| N\right]\right] + \mathrm{Var}\left[\mathrm{E}\left[\sum_i^N X_i \middle| N\right]\right] . \tag{3.20}$$

As $\mathrm{Var}\left[\sum_i^N X_i \middle| N\right] = N\,\mathrm{Var}\left[X\right]$ and $\mathrm{E}\left[\sum_i^N X_i \middle| N\right] = N\,\mathrm{E}\left[X\right]$, also with N and X independents, equation (3.20) becomes

$$\mathrm{Var}\left[\sum_i^N X_i\right] = \mathrm{E}\left[N\right]\mathrm{Var}\left[X\right] + \mathrm{Var}\left[N\right]\mathrm{E}\left[X\right]^2 . \tag{3.21}$$

In our case, N is a Poisson random variable (since N_{tot} in (3.1) follows a Poisson distribution) then E[N] = Var[N]. Moreover, using $\mathrm{Var}\left[X\right] = \mathrm{E}\left[X^2\right] - \mathrm{E}\left[X\right]^2$, one can reduce (3.21) to

$$\mathrm{Var}\left[\sum_i^N X_i\right] = \mathrm{E}\left[N\right]\mathrm{E}\left[X^2\right]. \tag{3.22}$$

Substituting $X = 4\Delta I^2 \frac{\beta}{(1+\beta)^2}\frac{\overline{\tau}}{1+\overline{\tau}^2\omega^2}$, as in equation (3.1), and E[N] = E[N_{tot}] = $N'_{tr}WL$, the Variance of the LF noise is

$$\mathrm{Var}\left[S_{Id}(\omega)\right] = 16N_{tr}WL\,\mathrm{E}\left[\Delta I^4 \frac{\beta^2}{(1+\beta)^4}\frac{\overline{\tau}^2}{(1+\overline{\tau}^2\omega^2)^2}\right] \tag{3.23}$$

or

$$\mathrm{Var}\left[S_{Id}(\omega)\right] = 16N_{tr}WL\int_0^\infty\int_{\tau_{\min}}^{\tau_{\max}}\int_0^\infty \Delta I_d^4 \frac{\beta^2}{(1+\beta)^4}\frac{\overline{\tau}^2}{(1+\overline{\tau}^2\omega^2)^2} f_{E_T} f_{\overline{\tau}} f_{\Delta I_d}\, dE_T\, d\overline{\tau}\, d\Delta I_d . \tag{3.24}$$

The function $\beta^2/(1+\beta)^4$, also, behaves as a delta function at $E = E_F$, with area equal to

$$\int_0^{\infty} \frac{\beta^2}{(1+\beta)^4} dE_T = -kT \int_{\infty}^{0} \frac{\beta^2}{(1+\beta)^4} \frac{1}{\beta} d\beta = \frac{kT}{6} . \quad (3.25)$$

Therefore, $\beta^2/(1+\beta)^4 \approx \frac{kT}{6}\delta(E-E_F)$ and (3.24) reduces to

$$\mathrm{Var}\left[S_{Id}(\omega)\right] = 16\frac{kT}{6} N_{tr} WL \int_0^{\infty} \int_{\tau_{\min}}^{\tau_{\max}} \Delta I^4 \frac{\bar{\tau}^2}{(1+\bar{\tau}^2\omega^2)^2} f_{E_T}(E_F) f_{\bar{\tau}} f_{\Delta I_d} d\bar{\tau} d\Delta I_d . \quad (3.26)$$

As ΔI_d is independent of $\bar{\tau}$, one can solve separately

$$\mathrm{E}\left[\frac{\bar{\tau}^2}{(1+\bar{\tau}^2\omega^2)^2}\right] = \int_{\tau_{\min}}^{\tau_{\max}} \frac{\bar{\tau}^2}{(1+\bar{\tau}^2\omega^2)^2} \frac{1}{\gamma\bar{\tau}} d\bar{\tau} = \frac{1}{2\gamma\omega^4}\left(-\frac{1}{\bar{\tau}_{\max}^2 + \frac{1}{\omega^2}} + \frac{1}{\bar{\tau}_{\min}^2 + \frac{1}{\omega^2}}\right) . \quad (3.27)$$

For $\bar{\tau}_{\min} << 1/\omega << \bar{\tau}_{\max}$, the variance of the noise is approximated as

$$\mathrm{Var}\left[S_{Id}(\omega)\right] \approx \frac{8}{6} N'_{tr} WL \mathrm{E}\left[\Delta I^4 f_{E_T}(E_F)\right] \frac{1}{\gamma\omega^2} , \quad (3.28)$$

or

$$\mathrm{Var}\left[S_{Id}(f)\right] \approx \frac{N'_{tr} WL}{3\pi^2 \gamma f^2} \mathrm{E}\left[\Delta I_d^4 f_{E_T}(E_F)\right] . \quad (3.29)$$

Again, considering the distribution of ΔI_d dependent on the position of the trap along the length of the channel and considering the traps uniformly distributed in the device's length,

$$\mathrm{E}\left[\Delta I_d^4 f_{E_T}(E_F)\right] = \frac{1}{L}\int_0^L \mathrm{E}\left[\Delta I_d^4 \middle| X_T = x\right] f_{E_T}(E_{Fn}) dx . \quad (3.30)$$

Therefore,

$$\mathrm{Var}\left[S_{Id}(f)\right] = \frac{kT}{3\pi^2\gamma f^2} W \int_0^L \mathrm{E}\left[\Delta I_d^4 \middle| X_T = x\right] N_{tr}(E_{Fn}) dx . \quad (3.31)$$

Finally, using $\Delta\tilde{I}_d = \frac{WL}{I_d}\Delta I_d$, the Variance of the LFN is given by (3.5).

$$(3.5): \quad \mathrm{Var}\left[S_{Id}(f)\right] = \frac{kT}{3\pi^2\gamma f^2} \frac{I_d^4}{W^3 L^4} \int_0^L \mathrm{E}\left[\Delta\tilde{I}_d^4 \middle| X_T = x\right] N_{tr}(E_{Fn}) dx .$$

3.6 Monte Carlo Comparison

To show that the derivations of (3.4), (3.5) and (3.6) are correct, we compare their results with a Monte Carlo calculation applied to (3.1).

In this Monte Carlo calculation, we use the same distributions for the random variables used for the derivation of the model (i.e. $\bar{\tau}$ is log-uniform distributed, the total number of traps is Poisson distributed and the traps are uniformly distributed in the device area). To show that the delta functions at E=E_F multiplied by kT and $kT/6$ are good simplifications for $\beta/(\beta+1)^2$ and $\beta^2/(\beta+1)^4$ respectively, we use an arbitrary distribution of the traps' energies (E_T) depicted in Figure 3.6. The temperature is 300 K and the frequency is 20Hz. We also assume that the current deviation is given by an exponential distribution (the assumption of an exponential distribution is explained in Chapter 4), where $E[\Delta\tilde{I}_d|X_T]$ = 2.8×10^{-13} cm^2, $E[\Delta\tilde{I}_d^2|X_T] = 1.57\times10^{-25}$ cm^4 and $E[\Delta\tilde{I}_d^4|X_T] = 1.47\times10^{-49}$ cm^8 for all traps' positions along the channel. An average of 620 traps was used per device with a hypothetical area of 1×1μm^2 and $\bar{\tau}$ distributed from $\bar{\tau}_{min}=2\times10^{-9}$ s and $\bar{\tau}_{max}=5\times10^{8}$ s, which gives the Ntr(E_F)/γ depicted in Figure 3.6.

Figure 3.6 – Arbitrary trap distribution in energy used in the Monte Carlo simulation.

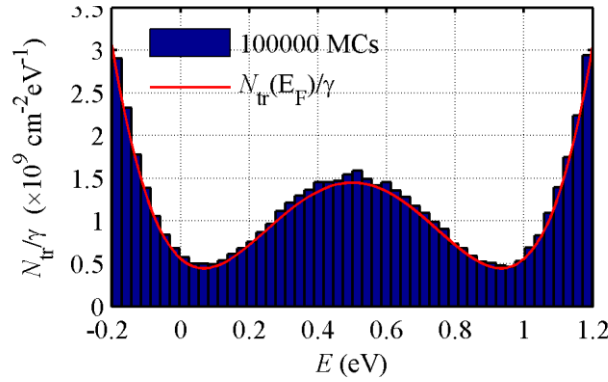

Figure 3.7 and Figure 3.8 show the comparison between the calculated values using (3.4), (3.5) and 100000 Monte Carlo simulations, described above, for different quasi-Fermi levels. The figures show a good fitting between the proposed model and the Monte Carlo. This indicates that the model was correctly derived and the simplifications used just introduce some minor errors.

Figure 3.7 – Expected value calculated using the proposed model (solid line) and Monte Carlo (symbols) for different quasi-Fermi levels.

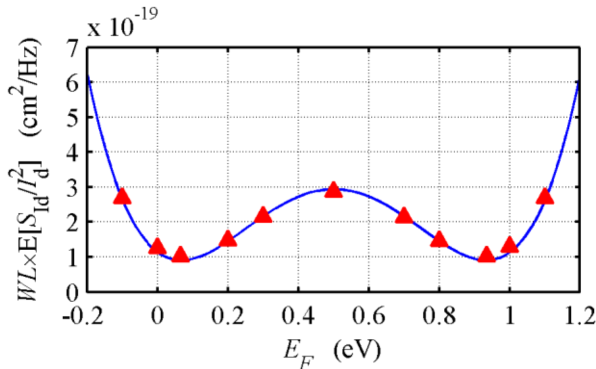

Figure 3.8 – Variance calculated using the proposed model (solid line) and Monte Carlo (symbols) for different quasi-Fermi levels.

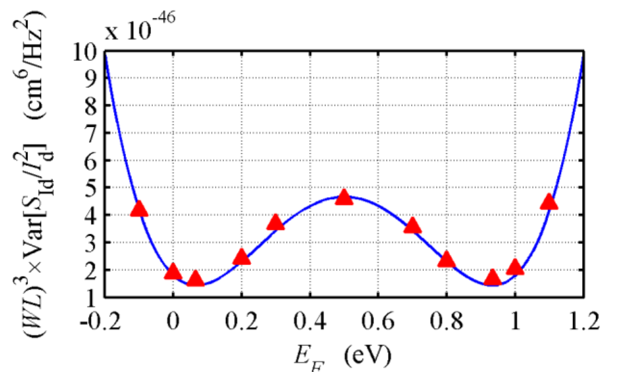

3.7 Derivation using SRH Model

In Sections 3.4 and 3.5, we derived the statistical model considering $\bar{\tau}$ a random variable log-uniform distributed. However, in Section 2.1, according to the SRH model, we derived that

$$\bar{\tau} = \frac{1}{\sigma_n \upsilon_{th} n} \frac{\beta}{\beta+1}, \tag{3.32}$$

where, now, the log-uniform distributed random variable is the trap capture cross section (σ_n).

In this section, we show that using (3.32) we have the same results as in Sections 3.4 and 3.5. From (3.9), the Expected value is calculated as

$$\mathrm{E}\left[S_{Id}(\omega)\right] = 4\,\mathrm{E}\left[N_{tot}\right] \int_0^\infty \int_{\tau_{\min}}^{\tau_{\max}} \int_0^\infty \Delta I_d^2 \frac{\beta}{(1+\beta)^2} \frac{\bar{\tau}}{1+\bar{\tau}^2\omega^2} f_{E_T} f_{\bar{\tau}} f_{\Delta I_d} dE_T d\bar{\tau} d\Delta I_d \,.$$

After applying the delta function simplification and using (3.32), one has that

$$\mathrm{E}\left[S_{Id}(\omega)\right] = 4kT\,\mathrm{E}\left[N_{tot}\right] \int_0^\infty \int_{\sigma_{\min}}^{\sigma_{\max}} \Delta I_d^2 \frac{(2\sigma_n \upsilon_{th} n)^{-1}}{1+(2\sigma_n \upsilon_{th} n)^{-2}\omega^2} f_{E_T}(E_F) f_{\sigma_n} f_{\Delta I_d} d\sigma_n d\Delta I_d \,. \tag{3.33}$$

Solving the cross-section independent of ΔI_d

$$\mathrm{E}\left[\frac{(2\sigma_n \upsilon_{th} n)^{-1}}{1+(2\sigma_n \upsilon_{th} n)^{-2}\omega^2}\right] = \frac{1}{\gamma_\sigma \omega}\left(\arctan\left(\omega/(2\sigma_{\min}\upsilon_{th} n)\right) - \arctan\left(\omega/(2\sigma_{\max}\upsilon_{th} n)\right)\right), \tag{3.34}$$

where

$$\gamma_\sigma = \ln\left(\frac{\sigma_{\max}}{\sigma_{\min}}\right) \tag{3.35}$$

The new observation window to make the Expected value of the noise inversely proportional to the frequency is $1/(2\sigma_{\max}\upsilon_{th} n) << 1/\omega << 1/(2\sigma_{\min}\upsilon_{th} n)$. The observation window hence is dependent on the carrier density. This can make the observation window, depending on the bias, to reach a region where the cross section is no longer log-uniform distributed (beyond σ_{min} and σ_{max}) and can result in a $1/f^{\alpha}$ dependence of the Expected value.

Restricting the observation window as $1/(2\sigma_{\max}\upsilon_{th} n) << 1/\omega << 1/(2\sigma_{\min}\upsilon_{th} n)$, then the Expected value is given by

$$\mathrm{E}\left[S_{Id}(\omega)\right] = 4\,\mathrm{E}\left[N_{tot}\right]\mathrm{E}\left[\Delta I^2 f_{E_T}(E_F)\right]\frac{1}{\gamma_\sigma \omega}\frac{\pi}{2}\,, \tag{3.36}$$

and it is the same as calculated in Section 3.4.

Equation (3.35) then suggests that, depending on the nature of the effect that dominates the cross section distribution (shown in Section 2.1), the N_{tr}/γ can be directly dependent on the

temperature (if energy activated, equation (2.10)), can be independent on the temperature (if purely tunnel assisted, equation (2.9)) or, as the mechanisms behind it are not totally understood, can have other temperature dependencies and also electric fields dependencies. Anyhow, in this work, we do not investigate the temperature dependency of the N_{tr}/γ, and all our measurements are done in the absolute temperature of 298 K.

Using the same methods one can show that the same conclusion applies for the Variance. The Variance is calculated as

$$\mathrm{Var}\left[S_{Id}(\omega)\right] = 16 N_{tr} WL \int_0^{\infty} \int_{\tau_{\min}}^{\tau_{\max}} \int_0^{\infty} \Delta I_d^4 \frac{\beta^2}{(1+\beta)^4} \frac{\overline{\tau}^2}{(1+\overline{\tau}^2\omega^2)^2} f_{E_T} f_{\overline{\tau}} f_{\Delta I_d} dE_T d\overline{\tau} d\Delta I_d \,. \tag{3.37}$$

After applying the delta function simplification one has that

$$\mathrm{Var}\left[S_{Id}(\omega)\right] = 16 \frac{kT}{6} N_{tr} WL \int_0^{\infty} \int_{\sigma_{\min}}^{\sigma_{\max}} \Delta I^4 \frac{(2\sigma_n \upsilon_{th} n)^{-2}}{(1+(2\sigma_n \upsilon_{th} n)^{-2}\omega^2)^2} f_{E_T}(E_F) f_{\sigma_n} f_{\Delta I_d} d\sigma_n d\Delta I_d \,. \tag{3.38}$$

Solving the cross-section independent of ΔI_d

$$\mathrm{E}\left[\frac{(2\sigma_n \upsilon_{th} n)^{-2}}{(1+(2\sigma_n \upsilon_{th} n)^{-2}\omega^2)^2}\right] = \frac{1}{2\gamma_\sigma \omega^4}\left(-\frac{1}{(2\sigma_{\min}\upsilon_{th} n)^{-2} + \frac{1}{\omega^2}} + \frac{1}{(2\sigma_{\max}\upsilon_{th} n)^{-2} + \frac{1}{\omega^2}}\right). \tag{3.39}$$

For the observation window $1/(2\sigma_{\max}\upsilon_{th} n) << 1/\omega << 1/(2\sigma_{\min}\upsilon_{th} n)$ the Variance is given by

$$\mathrm{Var}\left[S_{Id}(\omega)\right] \approx \frac{8}{6} N_{tr} WL\, \mathrm{E}\left[\Delta I^4 f_{E_T}(E_F)\right] \frac{1}{\gamma \omega^2}, \tag{3.40}$$

which is the same as shown in Section 3.5.

4 MODELING THE CURRENT DEVIATION

The next step to evaluate the proposed model in (3.4), (3.5) and (3.6), is to calculate the statistics of the impact of a trap at a given position in the channel. To that end, we start by using the drift-diffusion theory as proposed by Klaassen and Prins (1967) – in the derivation of thermal noise (Klaassen & Prins, 1967) – to calculate the current deviation caused by a trap at the oxide-silicon interface and at position x_t along the channel. After, we use a modified version of Klaasen and Prins to calculate the current deviation in non-uniform doped devices. Finally, we use these calculations as a start point to derive the full statistics of the trap impact at a given position along the channel.

4.1 The Charge Balance

When a carrier is trapped in the oxide, all the charges present in a cross section of the device balance out, altering the inversion charge, depletion charge and the gate charge, hence the total charge remains unchanged, as depicted in Figure 4.1.

Figure 4.1 – Charge balance in a small cross section of a NMOS transistor.

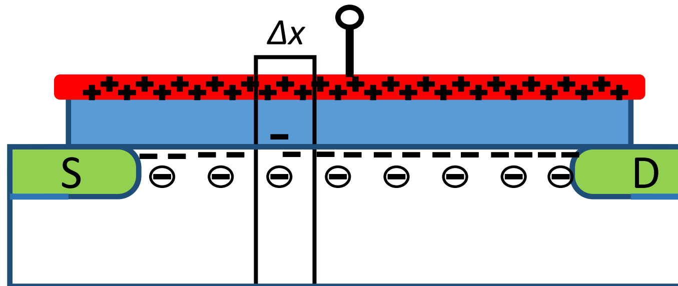

The drain current of a MOS device is given by

$$I_d = WQ_{inv}\mu \frac{dV}{dx} \quad . \tag{4.1}$$

Hence, the current deviation caused by an occupied trap has a direct relation with the deviation in the inversion charge and with the deviation in the mobility.

From the charge balance principle,

$$\delta Q_g = -(\delta Q_{inv} + \delta Q_D + \delta Q_t) \, . \tag{4.2}$$

The charges can be related to the capacitances using

$$\delta Q_{inv} = -C_{inv}\delta\varphi_s ,$$
$$\delta Q_D = -C_D\delta\varphi_s , \quad (4.3)$$
$$\delta Q_G = -C_{ox}\delta\varphi_s .$$

Where, C_{inv}, C_{ox}, C_D and φ_s are the inversion capacitance, oxide capacitance, depletion capacitance and surface potential respectively. Therefore, the change in the inversion charge due to a fluctuation in the trapped charge is given by (Reimbold, 1984)

$$\frac{\delta Q_{inv}}{\delta Q_t} = \eta = -\frac{\delta Q_{inv}}{\delta Q_G + \delta Q_{inv} + \delta Q_D} = \frac{C_{inv}}{C_{inv} + C_{ox} + C_D} , \quad (4.4)$$

Using the simplification $C_{inv} \approx q^2 N_{inv}/kT$,

$$\eta \approx \frac{N_{inv}}{N_{inv} + (kT/q^2)(C_{ox} + C_D)} . \quad (4.5)$$

4.2 Trap Impact on a Uniformly Inverted Channel ($V_{ds} \approx 0$V)

On a uniform channel, the resistance is given by

$$R_o = \frac{1}{g_0}\frac{L}{W} , \quad (4.6)$$

where g_0 is the channel conductivity.

After a trap is occupied, the conductivity in the impacted area ($L_t \times L_t$) will change to g', as depicted in Figure 4.2, and the new equivalent resistance of the channel is calculated as

$$R' = R_0 + \frac{R_0 L_t^2}{WL} \frac{\frac{\Delta g}{g_0}}{1 + \frac{L_t}{W}\frac{\Delta g}{g_0}} , \quad (4.7)$$

where $\Delta g = g_0 - g'$ is the change in conductivity in the area impacted by the occupied trap

Figure 4.2 – Change on the conductivity of a segment of a uniformly inverted channel device given by an occupied trap.

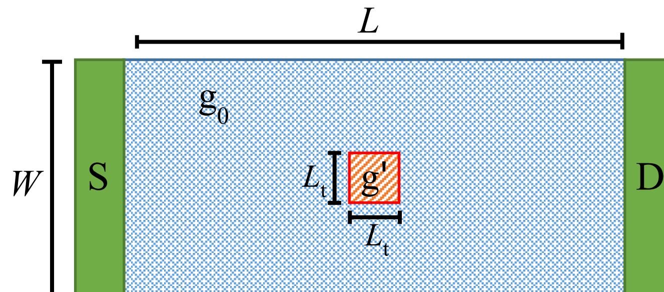

Therefore, the change in the channel resistance is

$$\Delta R \approx \frac{R_0 L_t^2}{WL}\frac{\Delta g}{g_0}, \tag{4.8}$$

and the impact on the current given by the occupied trap can be calculated as

$$\frac{\delta I_d}{I_d} = -\frac{\Delta R}{R_0} \approx -\frac{L_t^2}{WL}\frac{\Delta g}{g_0}. \tag{4.9}$$

The conductivity in a MOSFET is given by

$$g = Q_{inv}\mu \tag{4.10}$$

and the change in the conductivity given by a change in both inversion charge and mobility is

$$\begin{aligned} \Delta g &= \Delta Q_{inv}\mu + Q_{inv}\Delta\mu + \Delta Q_{inv}\Delta\mu \\ \Delta g &\approx \Delta Q_{inv}\mu + Q_{inv}\Delta\mu. \end{aligned} \tag{4.11}$$

4.3 Carrier Number Fluctuation

The carrier number fluctuation, or simply the number fluctuation, considers that there is only a change on the inversion charge. Hence,

$$\Delta g = \Delta Q_{inv}\mu. \tag{4.12}$$

From the charge balance, the change in the inversion charge is given by

$$\Delta Q_{inv} = \frac{\delta Q_{inv}}{\delta Q_t}\Delta Q_t, \tag{4.13}$$

hence, for only one trapped electron,

$$\Delta Q_{inv} = \frac{\delta Q_{inv}}{\delta Q_t}\frac{q}{L_t^2} = \eta\frac{q}{L_t^2}. \tag{4.14}$$

Finally, using (4.12), (4.14), (4.9) and considering a constant mobility along the channel, the current deviation (in a uniformly inverted channel) given by a fluctuation in the carrier density caused by an occupied trap is

$$\frac{\delta I_d}{I_d} = \frac{\eta}{WLN_{inv}}. \tag{4.15}$$

and it is independent on the trap impacted area ($L_t \times L_t$).

Using (4.5), we obtain

$$\frac{\delta I_d}{I_d} \approx \frac{1}{WL}\frac{1}{N_{inv} + (kT/q^2)(C_{ox} + C_D)}. \tag{4.16}$$

4.4 Mobility Fluctuation

If one considers that the occupied trap only changes the mobility of the device,

$$\Delta g = Q_{inv}\Delta\mu\,.$$

Relating the mean scattering rate ($1/\tau_{sc}$) with the mobility, one has that (Mueller & Schulz, 1996)

$$\frac{1}{\tau_{sc}} = \frac{q}{m^*}\frac{1}{\mu} = \sigma_{sc}\upsilon_{th}N_{sc}\,, \tag{4.17}$$

where m^* is the conduction effective mass, υ_{th} the thermal velocity, σ_{sc} the cross section of the scattering centers and N_{sc} the density of scattering centers.

From Matthiessen's rule

$$\frac{1}{\mu} = \frac{1}{\mu+\Delta\mu} + \frac{1}{\mu_{st}}\,, \tag{4.18}$$

where μ_{st} is the mobility due to a single trap and $\mu+\Delta\mu$ is the mobility due to all other scattering events. Substituting (4.18) into (4.17) and considering the mobility fluctuation due to only one trap, results in

$$\left(\frac{1}{\mu} - \frac{1}{\mu+\Delta\mu}\right) \approx \frac{\Delta\mu}{\mu^2} = \sigma_{sc,st}\upsilon_{th}m^*\frac{1}{L_t^2 q}\,. \tag{4.19}$$

Following our nomenclature, the single trap cross section is $\sigma_{sc,st} = L_t$, and the mobility fluctuation is given by

$$\frac{\Delta\mu}{\mu} = L_t\upsilon_{th}m^*\frac{1}{L_t^2 q}\mu\,. \tag{4.20}$$

From (4.9) the current deviation, given by a fluctuation in the mobility, is calculated as

$$\frac{\delta I_d}{I_d} = \frac{L_t^2}{WL}\frac{\Delta\mu}{\mu}\,. \tag{4.21}$$

Finally, substituting (4.20) into (4.21),

$$\frac{\delta I_d}{I_d} = \frac{L_t}{WL}\frac{\upsilon_{th}m^*}{q}\mu\,. \tag{4.22}$$

Differently from the carrier number fluctuation, equation (4.16), the current deviation caused by a mobility fluctuation is dependent on the trap scattering cross section. A simple estimate for L_t is calculated by considering that the carrier is scattered once the interaction energy from the trap is larger than kT (Simoen, et al., 1992). The electrostatic potential from a point charge is given by

$$V(r)=\frac{q}{4\pi\varepsilon_s r}\ . \tag{4.23}$$

Therefore, the cross section where the potential is larger than *kT/q* is given by (Simoen, et al., 1992),

$$L_t=\frac{2q^2}{4\pi\varepsilon_s kT}\ . \tag{4.24}$$

For T = 300 K, one has that L_t = 8 nm.

In strong inversion, the carriers charge decrease the trapped charge potential range (Simoen, et al., 1992), an effect named screening. Nevertheless, in thin oxide devices the gate charge also screens the trap potential [28], which makes the full calculation of the scattering cross section very complex, as the 2-D Poisson equation needs to be solved. In [28] the calculation of the cross section for thin oxide devices was done, and the authors concluded that the scattering cross section was weakly dependent on the carrier density and could be approximated as $1.6T_{ox}$.

In this work, the analyzed devices with oxides ranging from 2 nm to 5 nm. Therefore, we use $\alpha = L_t \upsilon_{th} m^* q^{-1}$ as a constant fitting parameter. For instance, when L_t = 4 nm one has that $\alpha \approx 1.3\times10^{-15}$ Vs.

4.5 Correlated Carrier Number and Mobility Fluctuation

Combining the effects of a charged trap on the carrier number and on the mobility, one has that

$$\Delta g \approx \Delta Q_{inv}\mu + Q_{inv}\Delta\mu \tag{4.25}$$

and

$$\frac{\delta I_d}{I_d}=\frac{L_t^2}{WL}\left(\frac{\Delta Q_{inv}}{Q_{inv}}+\frac{\Delta\mu}{\mu}\right). \tag{4.26}$$

Substituting (4.14) and (4.20) into (4.26),

$$\frac{\delta I_d}{I_d}=\frac{1}{WL}\left(\frac{\eta}{N_{inv}}+L_t\upsilon_{th}m^*\mu\frac{1}{q}\right) \tag{4.27}$$

For $\alpha = L_t\upsilon_{th}m^*q^{-1}$

$$\frac{\delta I_d}{I_d}=\frac{1}{WL}\left(\frac{\eta}{N_{inv}}+\alpha\mu\right) \tag{4.28}$$

Figure 4.3 shows a comparison between the carrier number and mobility component of (4.28) , for a typical NMOS transistor with $T_{ox} = 2.9$ nm , $V_{th} = 0.5$ V and α=0.8×10^{-15} Vs . From the figure, we can see that the mobility fluctuation component is only relevant at the strong inversion region.

Figure 4.3 – Comparison between the mobility fluctuation and number fluctuation components.

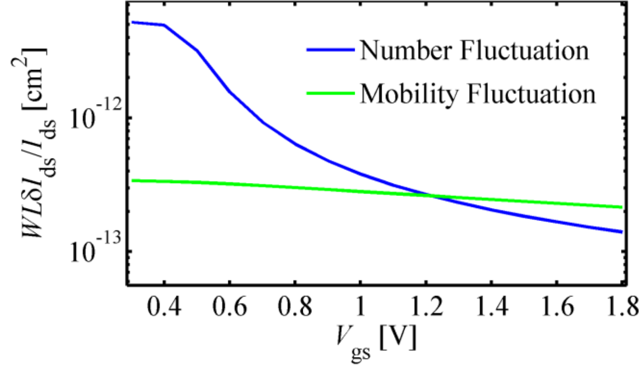

Using (4.5), we obtain

$$\frac{\eta}{N_{inv}} \approx \frac{1}{N_{inv} + (kT/q^2)(C_{ox} + C_D)}. \tag{4.29}$$

Therefore, in weak inversion, $N_{inv} << (kT/q^2)(C_{ox} + C_D)$ and, as shown in Figure 4.3, equation (4.28) saturates at

$$\left.\frac{\delta I_d}{I_d}\right|_{WI} \approx \frac{1}{WL}\frac{q^2}{kT(C_{ox} + C_D)}. \tag{4.30}$$

4.6 Trap Impact for a Non-uniformly Inverted Channel (|V_{ds}| > 0 V)

When |V_{ds}| is larger than 0 V the conductivity of the MOSFET is a function of the channel position, thus

$$g(x) = Q_{inv}(x)\mu(x) \tag{4.31}$$

and

$$\Delta g(x) \approx \Delta Q_{inv}(x)\mu(x) + Q_{inv}(x)\Delta\mu(x). \tag{4.32}$$

Therefore, to calculate the impact of a trap on the drain current the full transistor equation has to be considered. This was deduced in the Klaassen and Prins paper (Klaassen & Prins, 1967) for thermal noise calculation. In the paper, the authors relate the current impact on the terminal of a transistor with the internal current impact on an infinitesimal uniformly charged transistor, as shown in Figure 4.4. This relation is given by

$$\delta I_d = \frac{1}{L}\Delta i_x \Delta x\,, \tag{4.33}$$

where Δi_x is the impact on the current of the infinitesimal uniformly charged transistor with length equal to Δx.

Figure 4.4 – Equivalent transistor for calculating the current deviation.

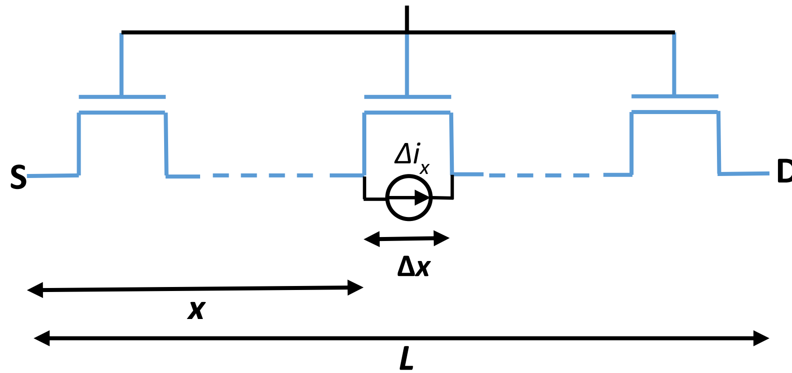

As previously calculated in (4.28), the impact of a trap on the current of a uniform transistor with length equal to Δx is given by

$$\frac{\Delta i_x}{I_d} = \frac{1}{W\Delta x}\left(\frac{\eta_x}{N_{inv,x}} + \alpha\mu_x\right). \tag{4.34}$$

Therefore, using (4.33) and (4.34), the current impact on a transistor is dependent of the trap position (x_t) and is equal to

$$\frac{\delta I_d(x_t)}{I_d} = \frac{1}{WL}\left(\frac{\eta(x_t)}{N_{inv}(x_t)} + \alpha\mu(x_t)\right). \tag{4.35}$$

Due to the infinitesimal uniform transistor approximation used in the derivation of (4.35), the result is an approximation where the channel potential between the positions x_t–L_t/2 and x_t+L_t/2 can be nearly constant, where L_t is the length under the influence of the trap.

4.7 Trap Impact for Non-Uniformly Doped MOSFETs

For non-uniformly doped devices, the Klaassen and Prins calculation is incorrect and a more complete derivation was done in the work in (Roy, et al., 2007), which relates the current impact on the terminal of a transistor with the internal current impact on an infinitesimal uniform transistor by

$$\delta I_d = \frac{f(x)}{\int_0^L f(x)dx}\Delta i_x \Delta x\,, \tag{4.36}$$

where,

$$f(x) = \exp\left[-\int_0^x \frac{1}{g} \frac{\partial g}{\partial x} dx \right]. \tag{4.37}$$

Therefore,

$$\frac{\delta I_d(x_t)}{I_d} = \frac{f(x_t)}{W\int_0^L f(x_t)dx}\left(\frac{\eta(x_t)}{N_{inv}(x_t)} + \alpha\mu(x_t) \right). \tag{4.38}$$

4.8 Sources of the Current Deviation Variability

From (4.38), one of the most evident sources of the current deviation variability is the trap position along the device channel. In order to account it without discarding other presumable source of variability, one can use the law of total expectation, $\mathrm{E}\left[\Delta I_d\right]=\mathrm{E}\left[\mathrm{E}\left[\Delta I_d \,|X_T\right]\right]$. For a uniform trap density from source to drain,

$$E\left[\Delta I_d\right] = \frac{1}{L}\int_0^L E\left[\Delta I_d \,|X_T = x\right]dx\,. \tag{4.39}$$

Another candidate source of ΔI_d variability is the trap distribution along the oxide thickness. If just the distribution of traps along the x (source to drain) and y (interface to gate) positions are considered as source of variability and if this distribution is uniform, we have

$$E\left[\Delta I_d\right] = \frac{1}{LT_{ox}}\int_0^L \int_0^{Tox} \Delta I_d(x,y)dydx\,, \tag{4.40}$$

where T_{ox} is the oxide thickness.

However, the position of the trap inside the oxide and along the channel are not the only sources of variability. Random dopant and fixed oxide charges are known to induce the current through percolation paths on the transistor channel (Mueller & Schulz, 1996) (Mueller & Schulz, 1998) (Asenov, et al., 2003). This effect makes the local current density bellow the trap to be a random quantity, resulting in a high variability of ΔI_d.

Some works on the literature associate the variability of ΔI_d caused by the random dopants, the oxide charges and the position of the trap inside the oxide to an exponential distribution (Mueller & Schulz, 1998) (Asenov, et al., 2003) (Bukhori, et al., 2010) (Kaczer, et al., 2010). Based on this, we assume that for a given position along the channel the current deviation can be approximated to an exponential distribution. For exponential distributions, we can easily calculate its second and fourth raw moments as a function of the average, hence:

$$E\left[\Delta\tilde{I}_d^2 \,|X_T\right] = 2E\left[\Delta\tilde{I}_d \,|X_T\right]^2$$
$$E\left[\Delta\tilde{I}_d^4 \,|X_T\right] = 24E\left[\Delta\tilde{I}_d \,|X_T\right]^4 \qquad (4.41)$$

We, now, further assume that for our proposed model,

$$E\left[\Delta\tilde{I}_d \,|X_T\right] = \delta\tilde{I}_d(x_t), \qquad (4.42)$$

with $\delta\tilde{I}_d(x_t)$ given by (4.38).

Remark

The exponential distribution is a special case of the Weibull distribution with the shape parameter $k_w = 1$. Therefore, we can use a more generic form of (4.41). Using the Weibull distribution properties

$$E\left[\Delta\tilde{I}_d^2 \,|X_T\right] = \Gamma\left(\frac{2}{k_w}+1\right)E\left[\Delta\tilde{I}_d \,|X_T\right]^2,$$
$$E\left[\Delta\tilde{I}_d^4 \,|X_T\right] = \Gamma\left(\frac{4}{k_w}+1\right)E\left[\Delta\tilde{I}_d \,|X_T\right]^4, \qquad (4.43)$$

where Γ is the gamma function.

According to our measurements present hereinafter we have a very good fitting of the model with the data using the exponential distribution, even though, a fine tuning can be achieved by the use of $k_w \neq 1$.

5 THE RTN STATISTICAL MODEL

In this Chapter, we connect the statistical current deviation model derived above with the model derived in Chapter 3, to create the complete Statistical RTN Model for MOSFETs. We introduce the quantity *K*, which gives the area scalability of the LFN variability for different technologies. We show the implications of the proposed model when the devices are operated under uniformly charged channel and non-uniformly charged channel conditions. We also show that the proposed model can explain the differences in the behavior between the n- and p-channel devices.

Completing the Model

Combining our proposed equations for the Expected value and the Variance of the LFN (equations (3.4) and (3.5) respectively) with the statistics of the current deviation derived in (4.41) and (4.42), gives the Expected value of the LFN as

$$\mathrm{E}\left[S_{Id}(f)\right] = 2\frac{kT}{f}\frac{I_d^2}{WL^2}\int_0^L \delta\tilde{I}_d^2(x)\frac{N_{tr}(E_{Fn})}{\gamma}dx \tag{5.1}$$

and the Variance as

$$\mathrm{Var}\left[S_{Id}(f)\right] = 24\frac{kT}{3\pi^2 f^2}\frac{I_d^4}{W^3L^4}\int_0^L \delta\tilde{I}_d^4(x)\frac{N_{tr}(E_{Fn})}{\gamma}dx, \tag{5.2}$$

where the normalized current deviation is given by (4.38),

$$\delta\tilde{I}_d(x_t) = WL\frac{\delta I_d(x_t)}{I_d} = L\left(\frac{f(x_t)}{\int_0^L f(x_t)dx}\right)\left(\frac{\eta(x_t)}{N_{inv}(x_t)} + \alpha\mu(x_t)\right). \tag{5.3}$$

From general statistics of the lognormal distribution, previously shown in (3.2),

$$\sigma\left[\ln\left(S_{id}(f)\right)\right] = \sqrt{\ln\left(1 + \frac{\mathrm{Var}\left[S_{Id}(f)\right]}{\mathrm{E}\left[S_{Id}(f)\right]^2}\right)}. \tag{5.4}$$

If a *K* parameter is defined as

$$K = WL\,\mathrm{Var}\left[S_{Id}(f)\right]\Big/\mathrm{E}\left[S_{Id}(f)\right]^2, \tag{5.5}$$

then (5.4) can be written as

$$\sigma\left[\ln\left(S_{id}(f)\right)\right]=\sqrt{\ln\left(1+\frac{K}{WL}\right)}. \tag{5.6}$$

The theory that is developed in this work shows that, under certain simplifying conditions, *K* is a constant value for all device geometries, justifying our choice to take *K* as the key quantity to investigate in this study. *K*, as will become clear in this work, is a normalized quantity that allows comparing the behavior of the noise variability amongst different technologies, dimensions, and bias conditions. Using (5.1) and (5.2) in (5.5), the quantity that describes the variability of LF noise is calculated as

$$K=6\frac{\gamma L}{3\pi^2 kT}\frac{\int_0^L \delta I_d^4(x)N_{tr}(E_F)dx}{\left(\int_0^L \delta I_d^2(x)N_{tr}(E_F)dx\right)^2}. \tag{5.7}$$

From the lognormal statistics, we also have that

$$\mu\left[\ln\left(S_{id}(f)\right)\right]=\ln\left(\mathrm{E}\left[S_{Id}(f)\right]\right)-\frac{1}{2}\sigma\left[\ln\left(S_{id}\right)\right]^2. \tag{5.8}$$

Hence, the 99.7th percentile of $S_{Id}(f)$ (+3σ in a normal distribution) can be calculated from

$$99.7^{\text{th}}\ \text{percentile}\, S_{Id}(f)=e^{\mu\left[\ln\left(S_{id}(f)\right)\right]+3\sigma\left[\ln\left(S_{id}\right)\right]}. \tag{5.9}$$

5.1 Models Comparison

For a uniformly doped MOSFET the current deviation is given by (4.35) and the Expected value of the noise in (5.1) becomes

$$E\left[S_{Id}(f)\right]=2\frac{kT}{\gamma f}\frac{I_d^2}{WL^2}\int_0^L\left(\frac{\eta(x)}{N_{inv}(x)}+\alpha\mu(x)\right)^2 N_{tr}(E_{Fn})dx, \tag{5.10}$$

which is a similar equation as the total noise derived in the widely-adopted flicker noise model introduced by Hung et al (1990),

$$S_{Id}(f)=\frac{kT}{\gamma_a f}\frac{I_d^2}{WL^2}\int_0^L\left(\frac{\eta(x)}{N_{inv}(x)}+\alpha\mu(x)\right)^2 N_t(E_{Fn})dx. \tag{5.11}$$

Despite the similarities, there are some fundamental differences in both equations. In Hung's model derivation, equation (5.11) is the total noise given by the sum of all the traps in a transistor. However, in our model, equation (5.10) is the Expected value of the noise in a set of transistors. Therefore, our proposed model is a stochastic model in which Hung's model is the special case when

WL is so large that $\sigma[\log(S_{Id})] \rightarrow 0$ and $E[S_{Id}(f)] \rightarrow S_{Id}(f)$, it is also the special case when the transistor is uniformly doped and the current deviation is just a function of the trap position along the channel. While, in our Expected value calculation the factor 2 accounts for the exponential distribution of the current deviation.

According to the derivation done by McWorther (1857) used by Hung et al (1990), τ is assumed to be associated with the depth location of the trap inside the oxide, and γ_a represents the attenuation coefficient of the electron wave function ($\gamma_a \approx 10^8$ cm). The log-uniform distribution of τ is attributed to a uniform distribution of traps inside the oxide. Campbell et al (2009) demonstrated that the elastic tunneling model underpinning this assumption is not realistic. In our approach τ is simply treated as a log-uniform random variable, implying that γ, in our model, represents the density of τ in the natural logarithm scale, hence $\gamma=\ln(\tau_{max}/\tau_{min})$ and it is unitless. In Hung's model the trap density, $N_t(E_F)$ has unit of cm^{-3}eV^{-1} while in our derivation $N_{tr}(E_F)$ has unit of cm^{-2}eV^{-1}. However, it should be noted that despite these differences in the assumptions, the resulting N_{tr}/γ (cm^{-2}.eV^{-1}) and N_t/γ_a (cm^{-2}.eV^{-1}) have the same unit in both works. In a direct translation between the parameters of both models

$$\frac{N_t(E_{Fn})}{\gamma_a} = 2\frac{N_{tr}(E_{Fn})}{\gamma} \; . \tag{5.12}$$

5.2 The Uniformly Inverted Channel

In the remainder of this work, the bias conditions that a device can be subject to are divided in two scenarios: the uniformly charged (inverted) channel and the non-uniformly charged channel. In the latter scenario, the effects of the halo implants and the large carrier density gradient induced by V_{ds} are substantial and the full calculation of the model equations must be done. In the first scenario, when V_{gs} is high and V_{ds} is small, the channel can be assumed to be uniformly charged (inverted) from source to drain. Under this assumption, ΔI_d and N_{tr}/γ can be assumed independent of the trap position, and the proposed model equations can be simplified into

$$\delta\tilde{I}_d = WL\frac{\delta I_d}{I_d} \approx \left(\frac{\eta}{N_{inv}} + \alpha\mu\right), \tag{5.13}$$

$$E\left[S_{Id}(f)\right] = 2\frac{kT}{f}\frac{I_d^2}{WL}\left(\frac{\eta}{N_{inv}} + \alpha\mu\right)^2 \frac{N_{tr}(E_{Fn})}{\gamma}, \tag{5.14}$$

$$Var\left[S_{Id}(f)\right] = 24\frac{kT}{3\pi^2 f^2}\frac{I_d^4}{(WL)^3}\left(\frac{\eta}{N_{inv}} + \alpha\mu\right)^4 \frac{N_{tr}(E_{Fn})}{\gamma}, \tag{5.15}$$

$$\frac{\mathrm{Var}\left[S_{Id}(f)\right]}{\mathrm{E}\left[S_{Id}(f)\right]^2} = 6\frac{1}{3\pi^2 kT}\frac{\gamma}{N_{tr}(E_F)}\frac{1}{WL} \tag{5.16}$$

and

$$K = WL\frac{\mathrm{Var}\left[S_{Id}\right]}{\mathrm{E}\left[S_{Id}\right]^2} = \frac{2}{\pi^2 kT}\frac{\gamma}{N_{tr}(E_F)}. \tag{5.17}$$

Moreover, under this condition $\eta \approx 1$ and $N_{\mathrm{inv}} \approx C_{\mathrm{ox}}\,(V_{\mathrm{gs}} - V_{\mathrm{T}})/q$, with V_{T} representing the strong inversion threshold voltage.

The above equations show that when the channel is uniformly charged and the trap density is independent of the transistor size, the Expected value of the LF noise is inversely proportional to the area $(WL)^{-1}$, the Variance is inversely proportional to the cubic of the area $(WL)^{-3}$ and K is area independent. The experimental results in Figures 5.1 − 5.3 confirm this behavior. In these figures we fit the extracted Expected value, Variance and K from the measured data and compare with the values calculated using (5.14), (5.15) and (5.17) respectively. For this fit we use $N_{\mathrm{tr}}(E_{\mathrm{F}})/\gamma = 1.5\times10^{9}$ cm^{2}eV^{-1} and $(\eta/N_{\mathrm{inv}} + \alpha\mu) = 2.8\times10^{-13}$ cm^2 for all devices dimensions. We also plot the results from 100000 draw Monte Carlo calculations applied to (3.1) (see Section 3.6), using a constant trap density in energy. The measured devices were fabricated in a 140-nm CMOS technology with $W\times L$ (μm^2) given by: 30×0.32, 8×8, 8×1, 8×0.336, 8×0.14 0.8×8, 0.8×0.32, 0.232×8, 0.232×0.32 and 0.232×0.14. For each geometry, 43 devices were measured.

For all the following analysis of this work, the Expected value, Variance and K are extracted from the measured data at **20 Hz**, using the Maximum Likelihood Estimator of lognormal distribution (described in Chapter 9). The uncertainty bars are the 0.02$^{\mathrm{th}}$ and 0.98$^{\mathrm{th}}$ quantiles from a Bootstrap analysis (described in Chapter 9). The temperature used in all the following analysis is 298 K.

Figure 5.1 – Area scaling of the Expected value of the LF noise, for n-channel devices in 140-nm technology. $V_{\mathrm{gs}} = 1.4$ V and $V_{\mathrm{ds}} = 0.1$V.

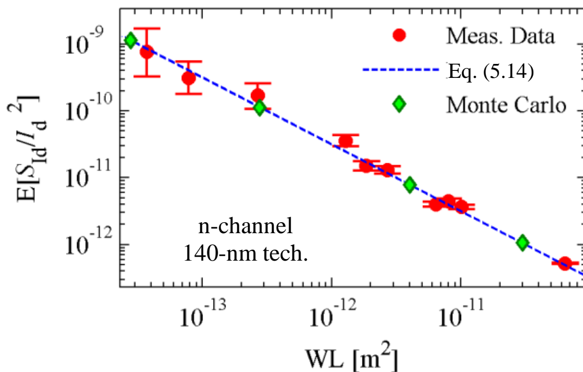

Figure 5.2 – Area scaling of the Variance of the LF noise, for n-channel devices in 140-nm technology. $V_{\mathrm{gs}} = 1.4$ V and $V_{\mathrm{ds}} = 0.1$V.

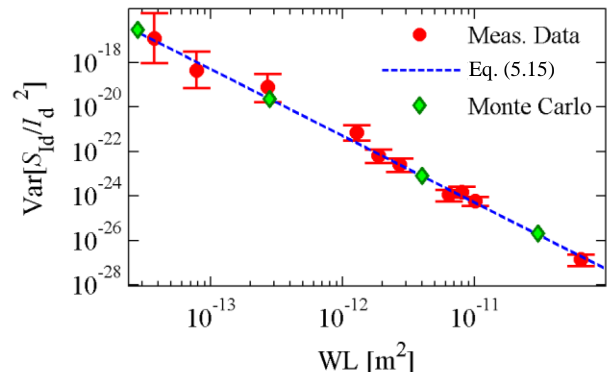

Figure 5.3 – K value for different area devices, for n-channel devices in 140-nm technology. V_{gs} = 1.4 V and V_{ds} = 0.1V.

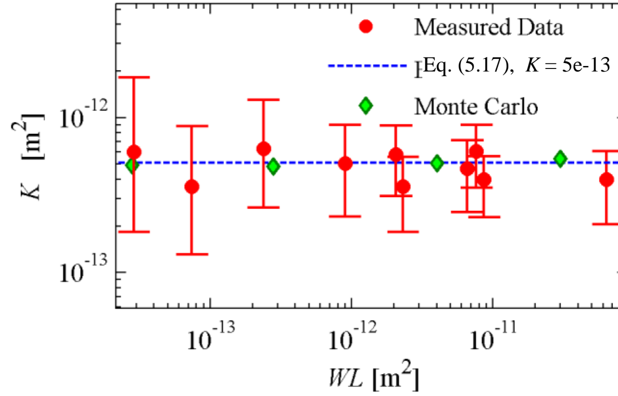

In the calculations above, we assumed $\delta\tilde{I}_d = (\eta/N_{inv} + \alpha\mu)$ to be the same value for all devices dimensions. However, this is not very accurate as V_T and the mobility varies for different channel length devices. In the analyzed 140-nm technology the V_T is expected to have values of 0.5 V and 0.6 V for the long channel and the minimum length device respectively. Therefore, this V_T variation in conjunction with a variation in the mobility can cause some deviation from the area dependency. However, this difference is very small compared to the span of orders of magnitude in the device area, shown in Figures 5.1 to 5.3. This deviation can be better seen in technologies with highly doped halo implants. The halo implants increase the Reverse Short Channel Effect (RSCE), which in turn increase the difference in V_T values between devices with different channel length, and increase the mobility difference.

The fact that a single value of K fits the variability for all device dimensions, as shown in Figure 5.3, and the dependence of K on the trap density given by (5.17), suggests that all devices have similar trap densities, despite their area. However, the high uncertainty in the small area devices data could be hiding a slightly higher trap density in the perimeter of the devices (e.g. along the Shallow Trench Isolation – STI – edges (Tuinhout & Duijnhoven, 2013)). Anyhow, one can conclude from these figures that the trap density should be roughly of the same order of magnitude for all device dimensions.

According to our model, the fitting value of K from Figure 5.3 can be used in (5.6) to give the area scaling prediction of the noise variability ($\sigma[\ln(S_{Id})]$) for this technology. Figure 5.4 and Figure 5.5 show how, in practice, the area scaling of the noise variability follows the predicted behavior of (5.6). The dashed lines represent the conventional 1/√area dependency when calculated using the large geometry devices (which gives the smallest statistical uncertainty). They clearly show the overestimation of the variability for small devices when the 1/√area relation is used. Moreover, Figure 5.5 also demonstrates that the variability does converge to the conventional 1/√area model for large area devices.

Figure 5.4 – Area scaling of the Standard Deviation of the logarithm of LF noise, for n-channel devices in 140-nm technology. V_{gs} = 1.4 V and V_{ds} = 0.1V.

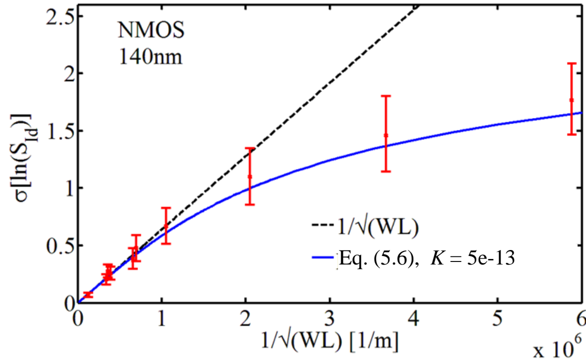

Figure 5.5 – Same data as in Figure 5.4 now plotted on log-log scale, to demonstrate that the model converges to 1/√area for large devices and that no noise saturation occurs near the origin of Figure 5.4.

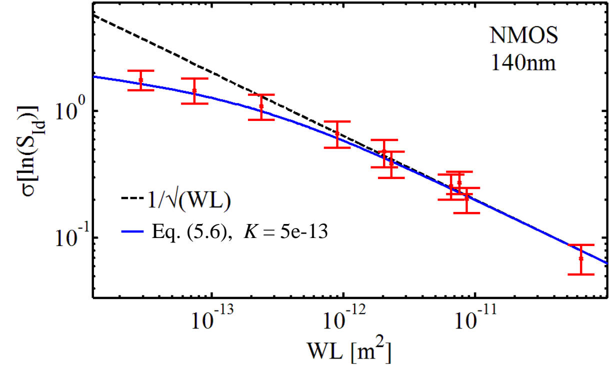

Figures 5.6 and 5.7 demonstrate, for a large and a small device geometry, how well the 3-sigma PSD predictions given by our noise variability model correspond with the observed variability of the LF noise spectra. The Standard Deviation was calculated using (5.6) with $K = 5\times10^{-13}$ m^2 for both geometries and was plotted back into the original spectra using (5.9). Figure 5.6 shows that for large area devices the many individual Lorentzians are summed, implying that they are no longer discernible as individual bumps. The apparent larger spectrum noise in the lower frequency bands (>1 kHz and <100 Hz), in Figure 5.6, is due to the lower number over time traces used for the FFT averaging at lower frequencies.

Figure 5.6 – Example of the LFN Variability model prediction for a population of large geometry devices plotted back into the original spectra using (5.6) with $K = 5\times10^{-13}$ m^2. WL = 30×0.336 μm^2, V_{ds} = 0.1 V and V_{gs} =1.4 1V.

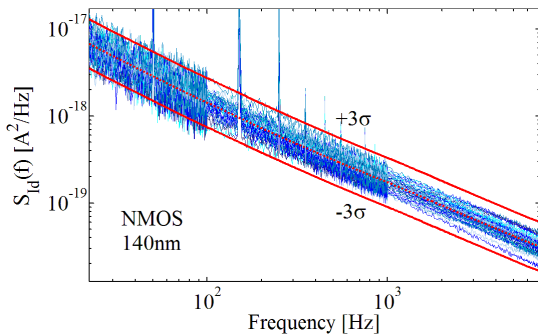

Figure 5.7 – Example of the LFN Variability model prediction for a population of small geometry devices plotted back into the original spectra. $K = 5\times10^{-13}$m^2. WL = 0.232×0.16 μm^2, V_{ds} = 0.1 V and V_{gs} = 1.4 V.

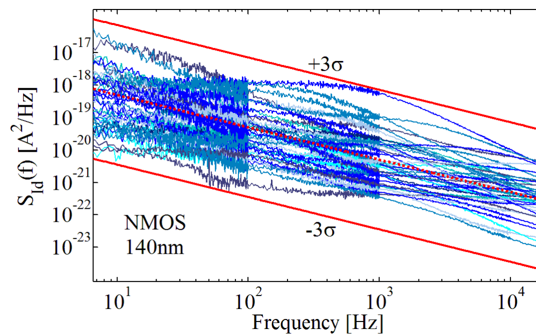

Figure 5.8 to Figure 5.11 demonstrate that, for p-channel devices in 140-nm technology, the proposed model also gives a good prediction of the noise statistics under the uniformly inverted channel assumption. The figures show the fittings using the proposed model for p-channel devices with V_{gs} = −1.4 V, V_{ds}= −0.1 V and $W\times L$ (μm^2) given by: 30×0.32, 8×1, 8×0.32, 8×0.14, 0.8×0.336,

0.232×0.336 and 0.232×0.14. For each geometry 43 devices were measured. The extracted Expected value, Variance, K and $\sigma[\ln(S_{Id})]$ are fitted using (5.14), (5.15), (5.17) and (5.6) respectively. A good fitting was achieved using $N_{tr}(E_F)/\gamma$=13.1×10^9 cm^{2}eV^{-1} and $(\eta/N_{inv} + \alpha\mu)$ = 2.7×10^{-13} cm^2 for all devices dimensions.

Figure 5.8 – Area scaling of the Expected value of the LF noise, for p-channel devices in 140-nm technology, V_{gs} = −1.4 V and V_{ds} = −0.1V.

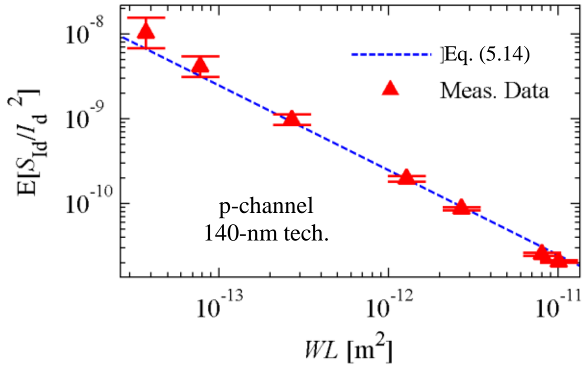

Figure 5.9 – Area scaling of the Variance of the LF noise, for p-channel devices in 140-nm technology, V_{gs} = −1.4 V and V_{ds} = −0.1V.

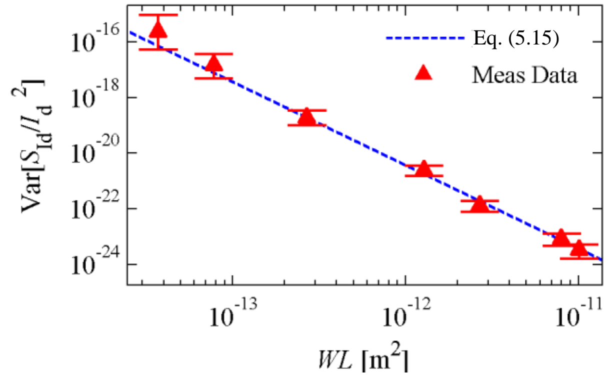

Figure 5.10 – K value for different area devices, for p-channel devices in 140-nm technology, V_{gs} = −1.4 V and V_{ds} = −0.1V.

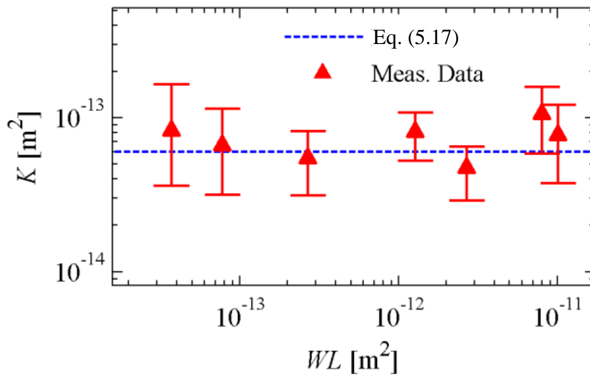

Figure 5.11 – Area scaling of the Standard Deviation of the logarithm of LF noise for p-channel devices in 140-nm technology, V_{gs}= −1.4 and V_{ds}= −0.1V.

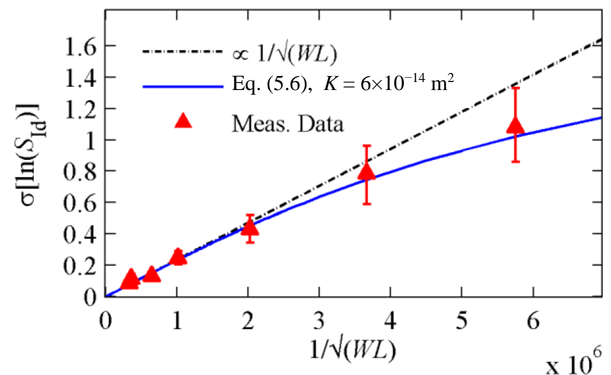

Figure 5.16 to Figure 5.15 show applications of the model for n- and p-channel devices from two additional contemporary mixed-signal CMOS technologies. For all cases, the simplified model allows an excellent fit of the noise statistics with device area. Figures 5.12 – 5.15 show the fitting for 40-nm technology with $|V_{gs}|$ = 1.1, $|V_{ds}|$ = 50 mV and W×L (μm^2) given by: 9×9, 0.9×0.9, 0.9×0.45 and 0.9×0.04. For each geometry 54 devices were measured. Figures 5.16 – 5.19 extends the low V_{ds} simplification to $|V_{ds}|$= 0.5V for the 65-nm technology with a thicker oxide (here called 65-nm GO2) – which allows a gate voltage up to 2.5 V. The fitting still holds for this case when the V_{gs} is large (hence implying a similar gradient of carriers for different device lengths). For the 65-nm GO2 technology 68 devices were measured for each geometry with W×L (μm^2) given by: 10×10, 1×5, 1×2, 1×0.5, 1×0.28, 0.4×5 and 0.4×0.28.

Figure 5.12 – Area scaling of the Expected value of the LF noise, for devices in 40-nm technology. $|V_{gs}| = 1.1$ V and $|V_{ds}| = 50$ mV.

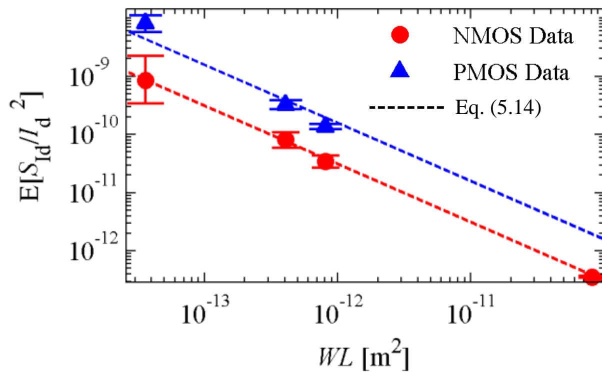

Figure 5.13 – Area scaling of the Variance of the LF noise, for devices in 40-nm technology, $V_{gs} = 1.1$ V and $V_{ds} = 50$ mV.

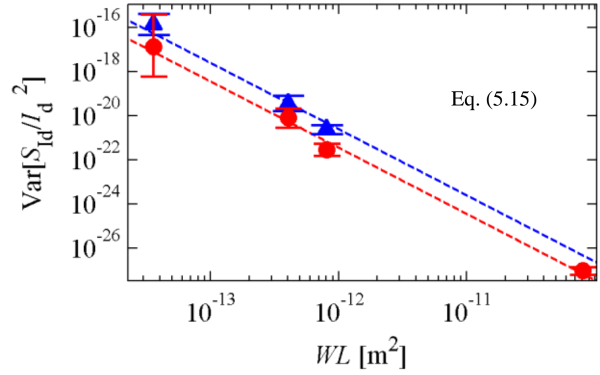

Figure 5.14 – K value for different area devices, for devices in 40-nm technology. $|V_{gs}| = 1.1$ V and $|V_{ds}| = 50$ mV.

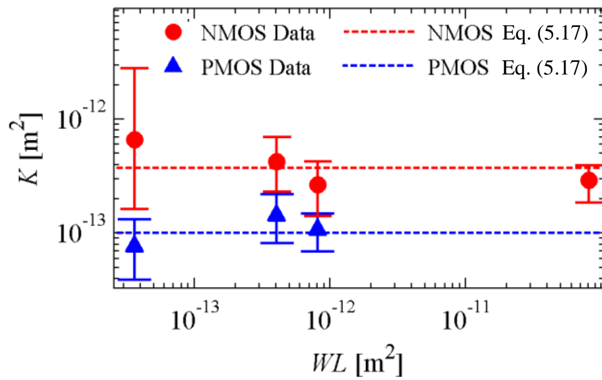

Figure 5.15 – Area scaling of the Standard Deviation of the logarithm of the LF noise for devices in 40-nm technology. Fitted using (5.6) with K=3.7×10^{-13} m^2 for NMOS and 1.2×10^{-13} m^2 for PMOS. $|V_{ds}|$ = 50mV and $|V_{gs}| = 1.1$V.

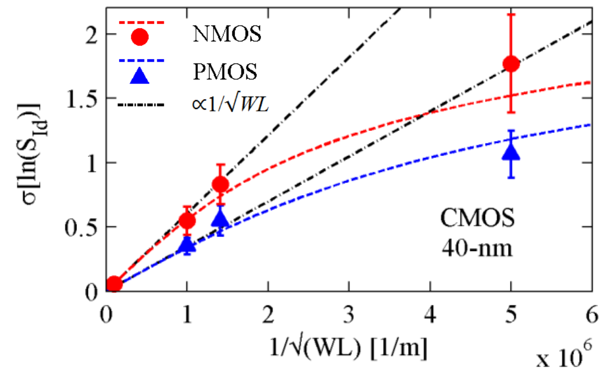

Figure 5.16 – Area scaling of the Expected value of the LF noise, for devices in 65-nm GO2 technology. $|V_{gs}| = 2.5$ V and $|V_{ds}| = 0.5$ V.

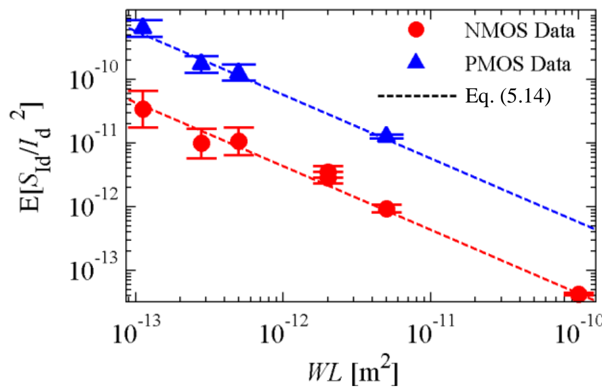

Figure 5.17 – Area scaling of the Variance of the LF noise, for devices in 65-nm GO2 technology. $|V_{gs}| = 2.5$ V and $|V_{ds}| = 0.5$ V.

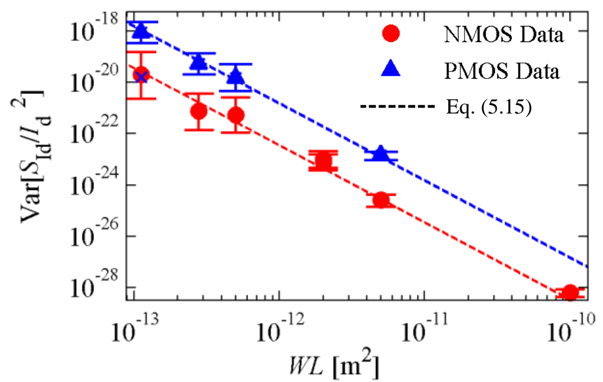

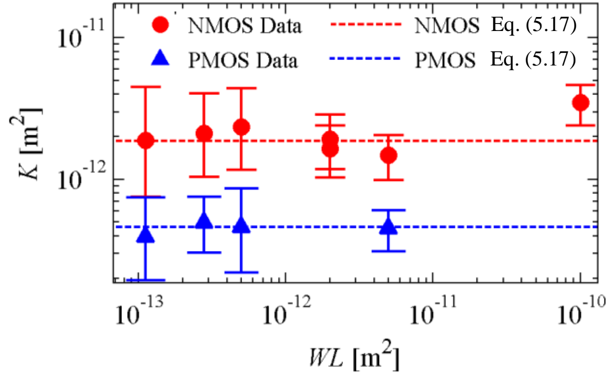

Figure 5.18 – K value for different area devices, for devices in 65-nm GO2 technology. $|V_{gs}| = 1.1$ V and $|V_{ds}| = 50$ mV.

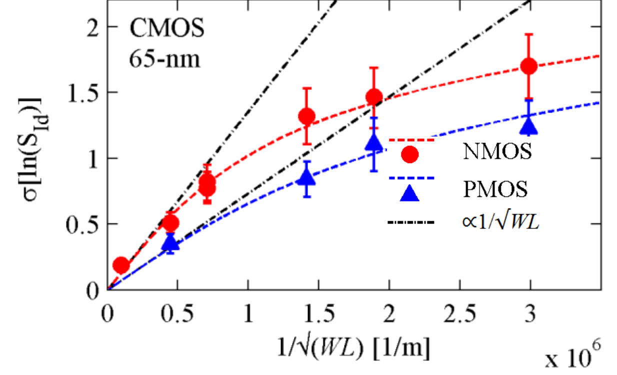

Figure 5.19 – Area scaling of the Standard Deviation of the logarithm of the LF noise for devices in 65-nm GO2 technology. Fitted using (5.6) with K = 1.9×10−12 m2 for NMOS and K = 5.4×10−13 m2 for PMOS. |Vds| = 0.5 V and |Vgs| = 2.5 V.

Comparing different technology nodes

Below, we show that we can use the uniformly charged channel condition and the proposed model to compare the parameters of different technology nodes. In the present work, we analyze the LF noise in three different technology nodes, 140-nm, 65-nm and 40-nm, all of them use silicon dioxide as dielectric and have polysilicon gate. Both NMOS and PMOS were measured. For the 65-nm node, devices with two different oxide thickness were measured, 2.5 nm and 5.6 nm, named GO1 and GO2 respectively. However, in this analysis of uniformly inverted channels the 65-nm GO1 devices are not analyzed since we only have the measurements with high drain bias applied.

Equation (5.6) shows that as higher the K value for a certain technology is, the higher the variability of the low frequency noise will be. From (5.7), the factors that distinguish K for different technologies and device dimensions are the trap density (N_{tr}/γ) and the spread of ΔI_d values. As we show in the next section, the spread of ΔI_d values are primarily due to the non-uniformity of carriers caused by either the doping gradient or the lateral electrical potential gradient (induced by V_{ds}). Using high gate bias and low drain bias voltages, we have a uniformly inverted channel, and the variability mechanisms of ΔI_d dependent on the position of the trap along the channel become irrelevant. Hence, as already discussed, for a uniformly charged channel the K value calculation is simplified to (5.17),

$$(5.17):\ K \approx \frac{2}{\pi^2 kT} \frac{\gamma}{N_{tr}(E_F)},$$

and the Expected value is reduced to (5.14), where $\delta \tilde{I}_d$ can be further simplified to $\delta \tilde{I}_d = q/(C_{ox} V_{g,eff}) + \alpha \mu_{eff}$. Hence,

$$\mathrm{E}\left[S_{Id}(f)\right] \approx 2\frac{kT}{WLf}\frac{N_{tr}(E_{Fn})}{\gamma}\left(\frac{q}{C_{ox}V_{g,eff}}+\alpha\mu_{eff}\right)^2 . \tag{5.18}$$

Equation (5.17) suggests that the trap density defines the variability in a uniformly inverted channel. Hence, the values of K used in Figures 5.3, 5.10, Figure 5.18 and 5.14 allow a comparison of the dielectric quality among the different technologies. The above equations show that the Expected value of the LF noise spectral density is directly proportional to the trap density whereas K (hence the variability) is inversely proportional to the trap density. Thereby, for a given technology, when the trap density is higher, K is lower and the Expected value is higher. When the oxide thickness (T_{ox}), the effective mobility (μ_{eff}), the mobility degradation factor (α) or V_T is higher, the Expected value of the noise is higher.

In Figures 5.1 − 5.15, we have fitted the measured data of different technologies, for both n-channel and p-channel devices, using the proposed model. Below, we use equations (5.17) and (5.18) , the quantities used in the above fittings and the parameters of each technology to extract the N_{tr}/γ and the $\alpha\mu_{eff}$ quantity. Hence, by assigning a mobility we can also extract the α parameter. Using this technique allows for some insights and comparison among the different technologies.

In Figure 5.1 to Figure 5.3, we have shown the model fit for various n-channel 140-nm devices with $V_{gs} = 1.4$ V and $V_{ds} = 0.1$ V. The fitting was done using a $N_{tr}(E_F)/\gamma = 1.5\times10^9$ cm^{-2}eV^{-1} and $(\eta/N_{inv} + \alpha\mu) = 2.8\times10^{-13}$ cm^2. The threshold voltage for this technology is assumed to be around 0.5 V and $T_{ox} = 2.9$ nm. Hence $q/(C_{ox}V_{geff}) = 1.5\times10^{-13}$ cm^2 and we can extract that $\alpha\mu_{eff}$ is around 1.3×10^{-13}. For a mobility of 200 cm^{2}Vs^{-1}, $\alpha = 0.7\times10^{-15}$ Vs. Moreover, using the extracted α and, from Chapter 4, that $\alpha = \sigma_{sc}\upsilon_{th}m^* q^{-1}$, the trap scattering cross section (σ_{sc}) is extracted to be about 2 nm. Hence, it is a reasonable physical quantity.

For the p-channel devices, in 140-nm technology, a good fitting was achieved using $N_{tr}(E_F)/\gamma = 13.1\times10^9$ cm^{2}eV^{-1} and $(\eta/N_{inv} + \alpha\mu) = 2.7\times10^{-13}$ cm^2 for all devices dimensions (Figures 5.8 − 5.11). The threshold voltage for the p-channel devices is also assumed to be around 0.5 V and $T_{ox,eff} = 2.9$ nm. Hence, $q/(C_{ox}V_{geff}) = 1.5\times10^{-13}$ cm^2 and we can extract that $\alpha\mu_{eff}$ is around 1.2×10^{-13} cm^2. For a mobility of 150 cm^{2}Vs^{-1}, $\alpha = 0.8\times10^{-15}$ Vs and the scattering cross section is also about 2 nm.

We also apply this methodology to the 40-nm and 65-nm technologies, analyzed above. The result is shown in Table 5.1 and Table 5.2, for n-channel and p-channel devices respectively.

Table 5.1 – Extracted Model Parameters for n-Channel Devices

Device	$T_{ox,eff}$ (nm)	$V_{g,eff}$ (V)	$WL\times E[S_{Id}/I_d^2]$ (cm^2 /Hz)	$(WL)^3\times Var[S_{Id}/I_d^2]$ (cm^6 /Hz^2)	K (m^2)	$\delta\tilde{I}_d$ (cm^2)	Ntr/γ (cm^{-2}eV^{-1})	$\alpha\mu_{eff}$ (cm^2)	α (Vs)
140-nm	2.9	0.9	3×10^{-19}	4.8×10^{-46}	5×10^{-13}	2.8×10^{-13}	1.56×10^{9}	1.3×10^{-13}	0.7×10^{-15}
40-nm	2.4	0.7	3.1×10^{-19}	3.65×10^{-46}	3.7×10^{-13}	2.4×10^{-13}	2.1×10^{9}	1×10^{-13}	0.5×10^{-15}
65-nm GO2	5.6	2	4.3×10^{-20}	3.5×10^{-47}	1.86×10^{-12}	2×10^{-13}	0.42×10^{9}	0.7×10^{-13}	0.4×10^{-15}

Table 5.2 – Extracted Model Parameters for p-Channel Devices

Device	$T_{ox,eff}$ (nm)	$V_{g,eff}$ (V)	$WL\times E[S_{Id}/I_d^2]$ (cm^2 /Hz)	$(WL)^3\times Var[S_{Id}/I_d^2]$ (cm^6 /Hz^2)	K (m^2)	$\delta\tilde{I}_d$ (cm^2)	Ntr/γ (cm^{-2}eV^{-1})	$\alpha\mu_{eff}$ (cm^2)	α (Vs)
140-nm	2.9	0.9	25×10^{-19}	3.6×10^{-45}	0.6×10^{-13}	2.7×10^{-13}	13.1×10^{9}	1.2×10^{-13}	0.8×10^{-15}
40-nm	2.7	0.7	16×10^{-19}	2.5×10^{-45}	1×10^{-13}	2.8×10^{-13}	7.8×10^{9}	1×10^{-13}	0.7×10^{-15}
65-nm GO2	5.6	2.1	5.7×10^{-19}	1.5×10^{-45}	4.6×10^{-13}	3.6×10^{-13}	1.7×10^{9}	2×10^{-13}	1.3×10^{-15}

5.3 Non-Uniformly Inverted Channel

When the inversion layer charge density and electrical fields are a strongly varying function of channel position, the dependence of ΔI_d on trap position will become appreciable. This makes K bias and length dependent (see equation (5.7) repeated below), which affects the noise variability given by (5.6), deviating its area scalability from the behavior predicted for uniformly charged channel, shown in Section 5.2. This length dependent behavior of K, for non-uniformly inverted channel devices, may increase the variability of large channel devices by more than an order of magnitude, which may, in some cases, cause the variability of long channel devices to be as large as that of short channel devices. Figure 6.20 shows an example of the loss of area scalability for devices with the same width ($W = 8$ μm) and with different lengths, for $V_{ds} = 0.5$V and $V_{gs} = 0.5$V. Therefore, for low V_{gs} and/or high V_{ds}, the full calculation of the proposed model equations ((5.1) − (5.7)) is required.

$$\text{(5.7):} \quad K = 6\frac{L}{3\pi^2 kT}\frac{\int_0^L \delta I_d^4(x) N_{tr}(E_F)/\gamma dx}{\left(\int_0^L \delta I_d^2(x) N_{tr}(E_F)/\gamma dx\right)^2}.$$

Figure 5.20 – LF noise PSD variability of 43 n-channel devices with $W = 8$ µm, using $V_{ds} = 0.5$ V and $V_{gs} = 0.5$ V.

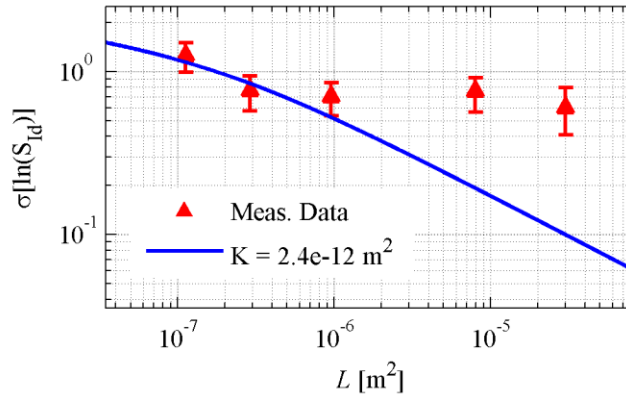

Equation (5.6) and (5.7) predict however, that when changing the W with a fixed L, the model should keep scale for any bias combination. This is only possible if the traps are uniformly distributed along the width of the devices and if there is no considerable border effect such as an increase on the trap density at the edges of the STI. According to our measurements in Figure 5.21, the width scalability is confirmed and if there is any increase in the trap density at the edges of the device, its effects on the device variability are hidden within the uncertainty of the variability.

Figure 5.21 – Variability as a function of the channel width for various bias configuration, $L = 0.32$ µm.

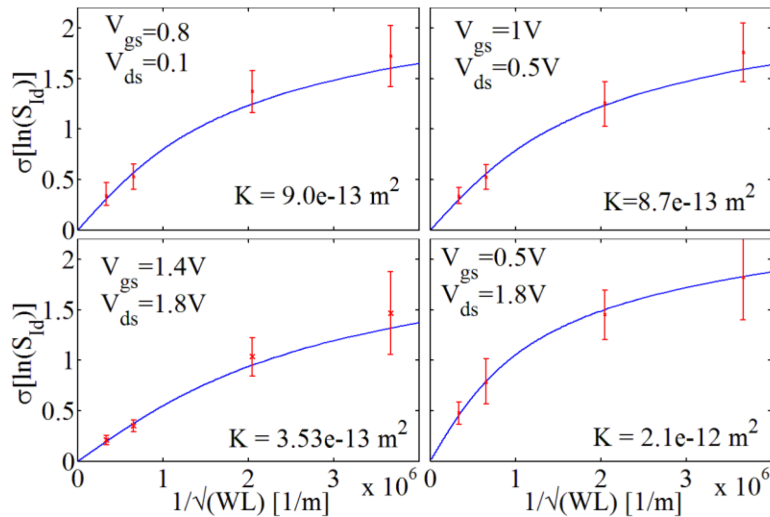

The fitted K's from this experiment (varying W, fixed L), for each bias combination, are summarized in Figure 5.22. The figure indicates a clear difference, between short and long channel devices, on the behavior of K relative to the drain bias and gate bias dependency. For long channel devices, Figure 5.22 shows that K is strongly dependent on V_{gs} and V_{ds}, which can vary by more than 2 orders of magnitude. For short channel devices, Figure 5.22 shows that the K dependence on V_{gs} is weaker than for the long channel device, and that K is practically independent on V_{ds}. In addition, for both short and long channel devices, as V_{gs} increases, K approaches the value calculated for the uniform channel condition in Section 5.2.

Following our model, the change in K with V_{gs} could either be attributable to a gate bias dependency of $N_{tr}(E_F)$, or to an increase of $E[\Delta I_d^4]/E[\Delta I_d^2]^2$ associated with a non-uniformity of the channel (e.g. non-uniform doping or source and drain potential effect). The difference in the behavior of long and short channels can be associated to the enhancement of the contribution of the halo-implanted regions in long channel devices to the noise (Paydavosi, et al., 2013), hence for short channel this dependence with V_{gs} is weaker due to the overlap of the halo-implanted regions. Moreover, the different behavior with V_{ds} can be attributed to the fact that the surface carrier concentration on the drain side of the channel is a function of V_{ds} and, due to the velocity saturation, it is also a function of the channel length. Therefore, from (5.7), K – and thus the variability – will depend on the channel length, V_{gs} and V_{ds}.

Figure 5.22 – Difference between the K behavior for short and long channel devices.

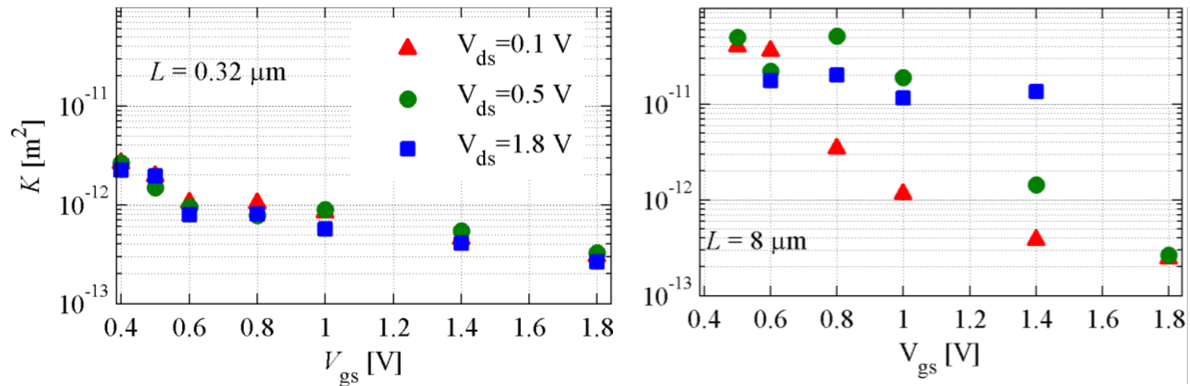

Figure 5.23 and Figure 5.24 then demonstrate how this increase on the K value is very significant for long channel devices. Figure 5.24 shows that the LF noise PSD of a large area device can easily vary by 2 orders of magnitude for certain bias configuration.

Figure 5.23 – LF noise PSD of 43 NMOS 140-nm node devices, W = 8 µm, L = 8µm, V_{gs}=1.4 and V_{ds}=0.5 V.

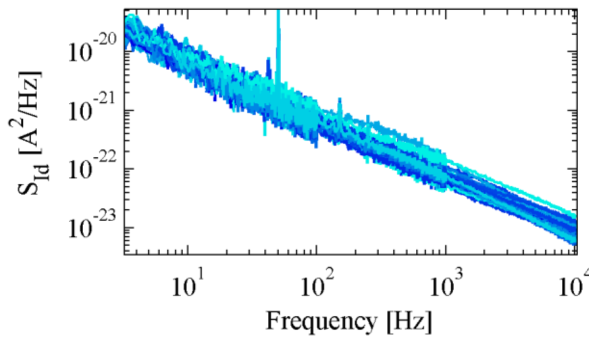

Figure 5.24 – LF noise PSD of 43 NMOS 140-nm node devices, W = 8 µm, L = 8 µm, Vgs = 0.5 and Vds = 0.5 V.

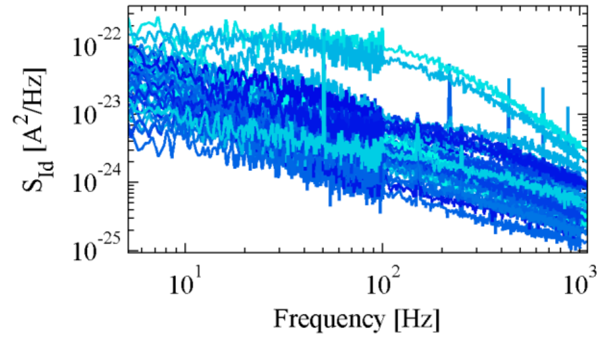

Therefore, when dealing with non-uniformly inverted channels, different device lengths have different electric field behaviors and different distribution of carriers along the channel. This leads to a different distribution of the current deviation as a function of the trap position in the channel. Hence

the integrals relation in (5.7) will have different values for different device lengths. Moreover, non-uniformly doped devices will have different δI_d in different doped regions, which enhance the variability of the current deviation and thereby increases K. Figure 5.25 to Figure 5.32 show, for 4 different technologies, that this length and bias dependent behavior of K is consistent among different device geometries and technologies.

These effects on K values will be discussed in detail in Chapter 6, where $\delta I_d(x_t)$ and K for different bias conditions will be calculated using the data extracted from TCAD simulations for long channel and short channel devices.

Figure 5.25 – Extracted K of 43 n-channel devices in 140-nm technology with V_{ds} = 0.1 V. W = 8 μm and various channel lengths.

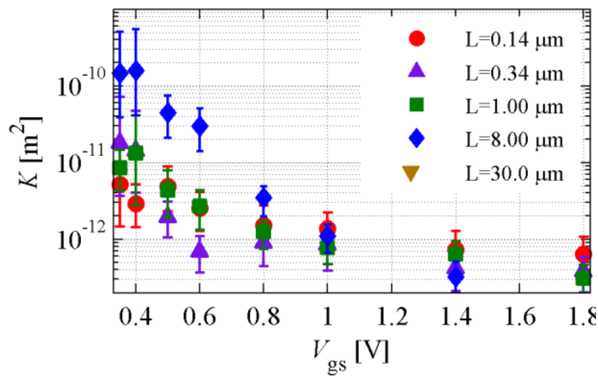

Figure 5.26 – Extracted K of 43 n-channel devices in 140-nm technology with V_{ds} = 0.5 V. W = 8 μm and various channel lengths.

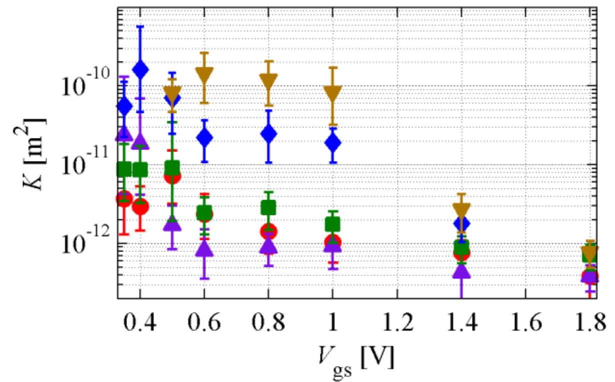

Figure 5.27 – Extracted K of 43 n-channel devices in 140-nm technology with V_{ds} = 1.8 V. W = 8 μm and various channel lengths.

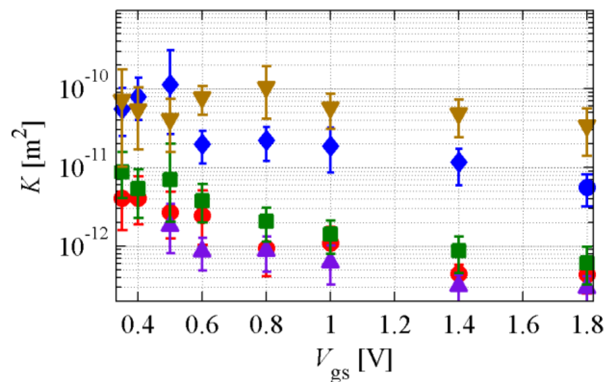

Figure 5.28 – Extracted *K* of 63 n-channel devices in 40-nm technology with V_{ds} = 0.05 V. *W* = 0.9 µm and various channel lengths. For 9-µm long devices, *W* = 9µm.

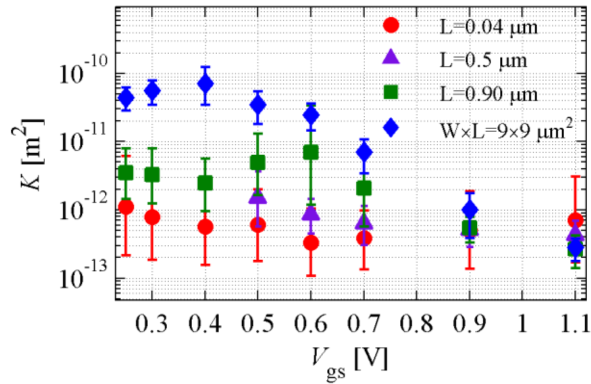

Figure 5.29 – Extracted *K* of 63 n-channel devices in 40-nm technology with V_{ds} = 0.55 V.

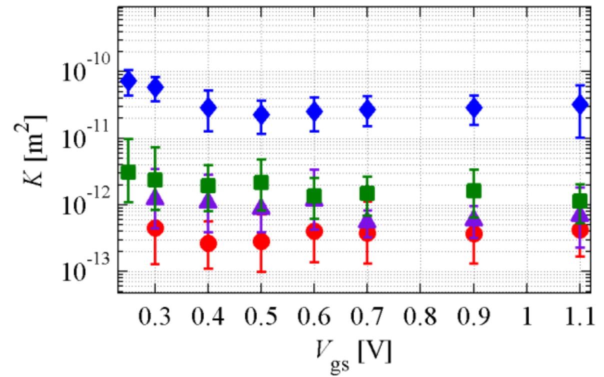

Figure 5.30 – Extracted *K* of 63 n-channel devices in 40-nm technology with V_{ds} = 1.1 V.

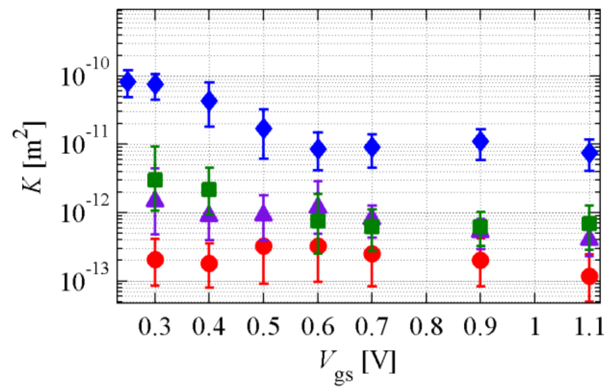

Figure 5.31 – Extracted *K* of 282 n-channel devices in 65-nm GO1 technology with V_{ds} = 0.5 V. *W* = 1 µm and various channel lengths. For the 10-µm long devices, *W* = 10µm.

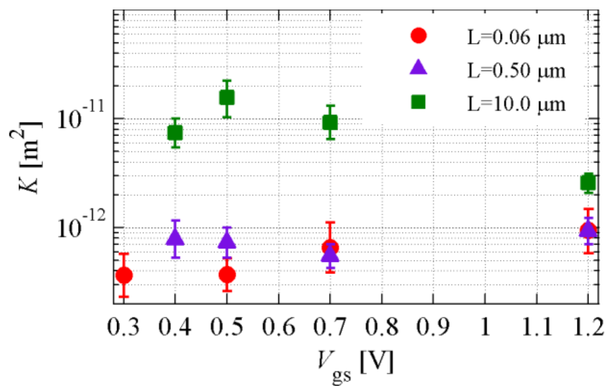

Figure 5.32 – Extracted *K* of 68 NMOS 65-nm node GO2 devices with V_{ds} = 0.5 V. *W* = 1 µm and various channel lengths. For 10-µm long devices, *W* = 10µm.

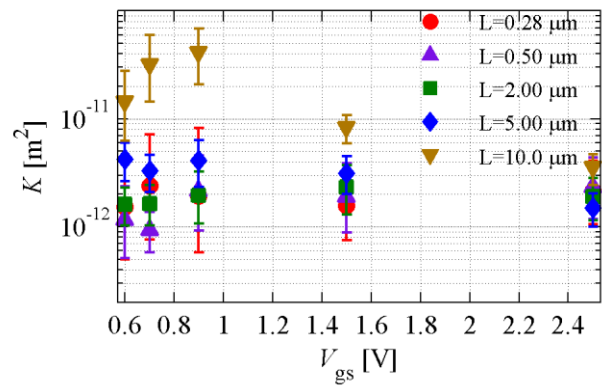

5.4 n-Channel Versus p-Channel Devices

In Section 2.5, we have discussed the difference on the behavior of the LF noise between n- and p-channel devices. We also commented that, to explain this difference, two schools of thought have emerged. One school of thought attributes the noise of NMOS transistors to trapping, and attributes the noise of PMOS transistors to a bulk mobility fluctuation (i.e Hooge model) (Vandamme, et al., 1994). The other school of thought considers the noise of both NMOS and PMOS transistors to be a consequence of the trapping mechanism, with the trap density constant for NMOS transistors and varying with the quasi-Fermi level for PMOS transistors (Scofield, et al., 1994).

Figures 5.33 and 5.34 show the Expected value and K of short channel devices (L = 0.14 um) for n-channel and p-channel devices. The figures show that for high $|V_{gs}|$ the p-channel device LF noise has a larger Expected value and a smaller K than that of the n-channel device. From our model, this strongly indicates that at energies accessible in the operation of p-channel devices the trap density is higher than the trap density at energies accessible in the operation of n-channel devices. This can be seen in Section 5.2, where for three different technologies - in uniformly inverted channel conditions - we show that p-channel devices have a higher Expected value and a smaller K and therefore we have extracted a higher trap density for p-channel devices in Tables 5.1 and 5.2.

The figures also show that the Expected value of the p-channel devices has a weaker dependence on gate bias than of the n-channel devices, and K (hence the variability) of the p-channel devices has a larger dependence on gate bias than of the n-channel devices. In Figure 5.34 we can see that even within V_{gs}=1.8 V and V_{gs} 1.4 V, which meet the uniformly inverted channel conditions, the K value of p-channel device varies by almost three times. From the mechanism described above and from (5.7), this effect can only be explained by the dependence of the trap density with the quasi-Fermi level, which supports the viewpoint of Scofield et al. (1994). This viewpoint considers the trap density to be weakly dependent on energy for n-channel devices and strongly dependent on energy for p-channel devices.

For p-channel devices, decreasing $|V_{gs}|$ therefore effectively reduces the trap density. This effect counteracts that of δI_d with V_{gs}, which increases with decreasing $|V_{gs}|$. Thus, due to these opposing effects, the dependence of $E[S_{Id}(f)]$ with V_{gs} is reduced. In turn, the trap density reduction with decreasing $|V_{gs}|$ increases the variability, as K is inversely proportional to N_{tr}/γ. This effect explains the smaller dependence of $E[S_{Id}(f)]$ and the larger dependence of the K value with the gate bias for p-channel compared to n-channel devices found in Figures 5.33 and 5.34.

Figure 5.33 – Expected value of 43 p-channel devices in 140-nm technology, with W×L = 8×0.14μm2 and |Vds| = 0.1 V.

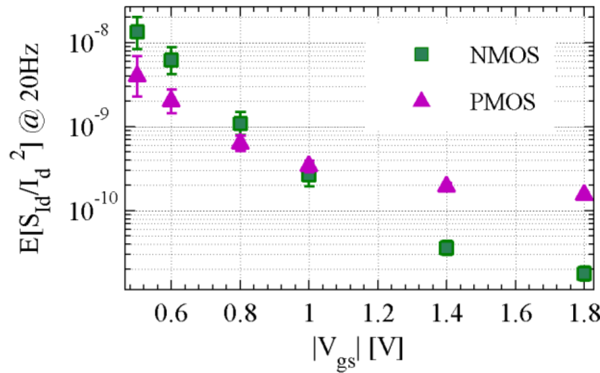

Figure 5.34 – K value of p-channel devices in 140-nm technology, with W×L = 8×0.14μm2 and |Vds| = 0.1 V.

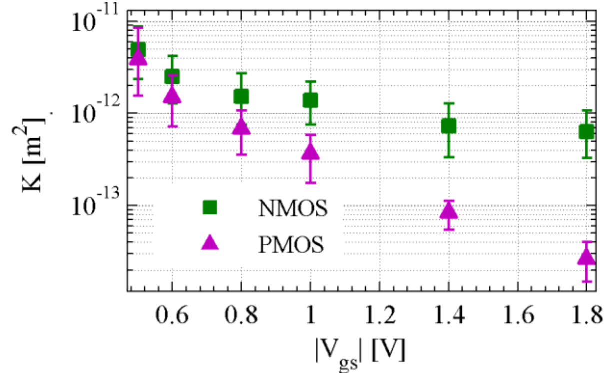

Figures 5.35 − 5.37 then show that the behavior described above is also found for p-channel devices with different geometries and drain biases.

Figure 5.35 – Extracted K of 43 p-channel devices in 140-nm node, with W = 8 μm, V_{ds} = 0.1 V and various channel lengths.

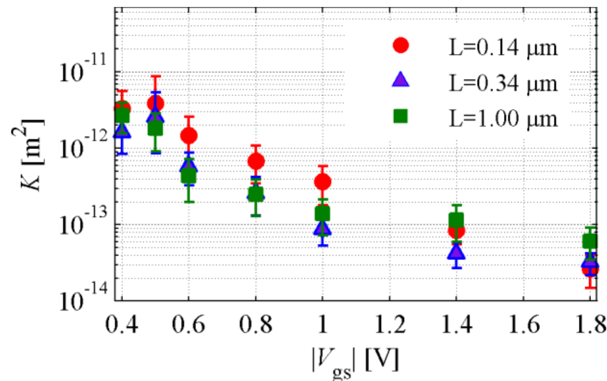

Figure 5.36 – Extracted K of 43 p-channel devices in 140-nm node, with W = 8 μm, V_{ds} = 0.5 V and various channel lengths.

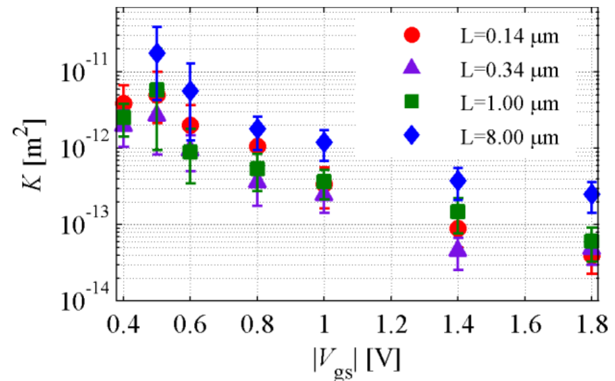

Figure 5.37 – Extracted K of 43 p-channel devices in 140-nm node, with W = 8 μm, V_{ds} = 1.8 V and various channel lengths.

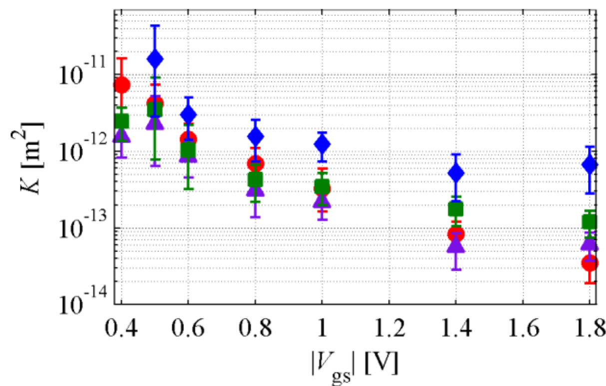

6 MODEL CALCULATION USING TCAD SIMULATIONS

In section 5.2, we were able to calculate the statistics of the Low Frequency Noise for various different technological nodes under the uniformly-inverted channel simplification. The next step is to test the proposed model for all bias situations. In section 5.3, we have explained that when the inversion charge layer has a non-uniform distribution along the device channel the variability of the noise will have a different behavior among different channel lengths devices. To test this hypothesis, we need to properly calculate the current deviation as a function of the trap position along the channel given by (5.3). To that end, in this chapter we use a TCAD tool for extracting the trap impact at different channel positions.

In this chapter, we show that with the help of a TCAD simulator we can analyze the influence of the halo-implanted regions and the bias on the LF noise statistics. We also show that we can properly calculate K, the Expected value and Variance of the noise using the quantities (δI_d, N_{inv}, μ, E_F …) extracted from the TCAD simulator, with a TCAD deck carefully calibrated to reproduce the measured DC IV characteristics.

6.1 TCAD Deck Calibration

To do this analysis, first we need to replicate the transistor characteristics in the TCAD simulator. The TCAD simulation is divided in two steps: the process simulation and the device simulation. The process simulation was done using the TSUPREM-4 tool. In this step, all major process steps were simulated in 2-D, such as oxidation, implantation, deposition, diffusion, etc. After the process simulation, a 2-D cross section of the device containing the doping profiles and device structure is generated. Then, the generated 2-D structure is simulated in the MEDICI device simulator where the electrical transport models and related parameters are defined. The device simulation then gives the potentials and currents at the device electrodes. This information is compared to the measured data of real devices and the process information or the device parameters are tuned until the DC IV characteristics of the real devices are reproduced in the device simulator. Figure 6.1 demonstrates a schematic of this calibration process.

Figure 6.1 – Schematic of the calibration process.

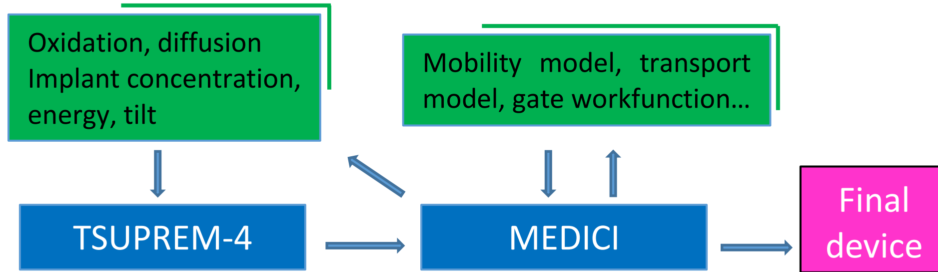

After reaching a good process description, with the right doping profiles and device structure, we compare the CV and IV characteristics. This comparison not only allows us to check the process information but also allows us to calibrate some of the device parameters such as the mobility parameters, the gate workfunction and permittivity of the dielectric. All device simulations were done using the Modified Local Density Approximation (MLDA) quantum correction model – which gives a better estimation of the real carrier density in the device – and using the drift diffusion transport model.

As demonstrated in Figure 6.2, we use the CV curve to check the doping profiles by comparing the depletion capacitance, given by the bottom part of the curve. We can also use the CV curve to compare the gate work function, the permittivity of the dielectric and the depletion of the polysilicon. Figure 6.2 shows an example of the CV curve of a long n-channel device in 140-nm technology, from the figure we see that we must increase the gate work function and must decrease the oxide capacitance to have a better fit. The gate work function was tuned by increasing the polysilicon electron affinity parameter, since the process simulation includes the polysilicon deposition step. The oxide capacitance was tuned by decreasing the oxide permittivity. The final result is also shown in Figure 6.2.

Figure 6.2 – CV curve comparison for the n-channel 140-nm technology.

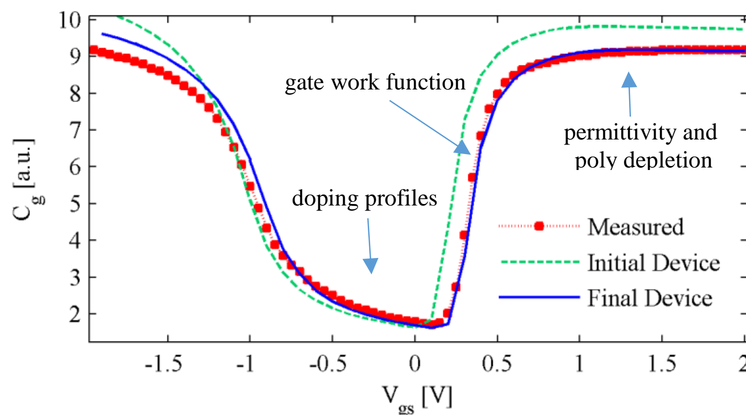

After reaching a good CV curve fit, the next step is to check the $I_{ds}\times V_{gs}$ curves to fine-tune the mobility parameters. The following mobility models were used in the simulation: Lombardi model

(which includes doping dependence and the transversal field dependence) and the High Lateral Field model (which accounts for velocity saturation). The steps used to check and tune the mobility parameters are as follows:

1. Long channel device with low drain bias (Figure 6.3) – to check the surface roughness parameter and surface phonon degradation parameter.
2. Short channel with low drain bias (Figure 6.4) – to check contact or/and lumped resistance.
3. Short channel high drain bias (Figure 6.5) – to check high field mobility model.

Figure 6.3 – IV curve of a large channel device with low drain bias.

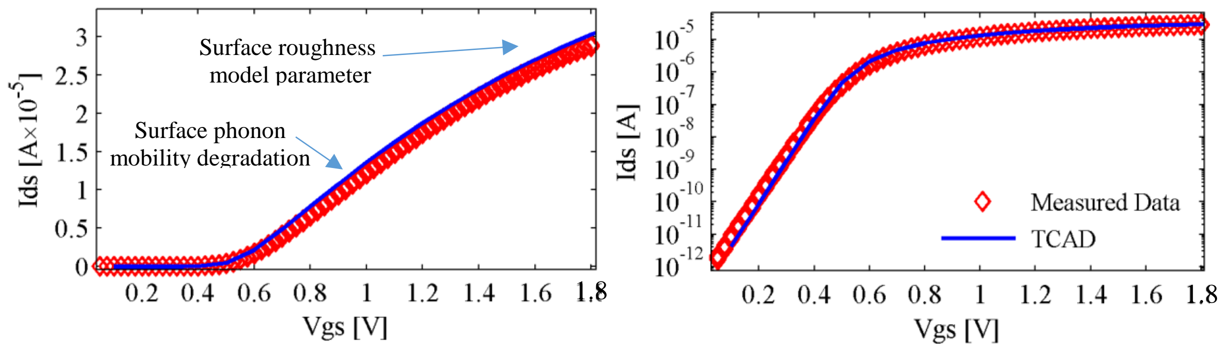

Figure 6.4 – IV curve of a short channel device with low drain bias.

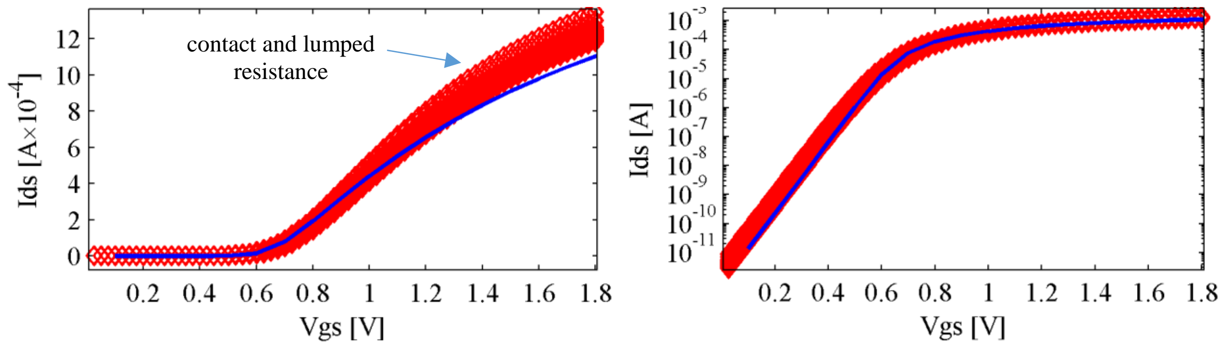

Figure 6.5 – IV curve of a short channel device with high drain bias.

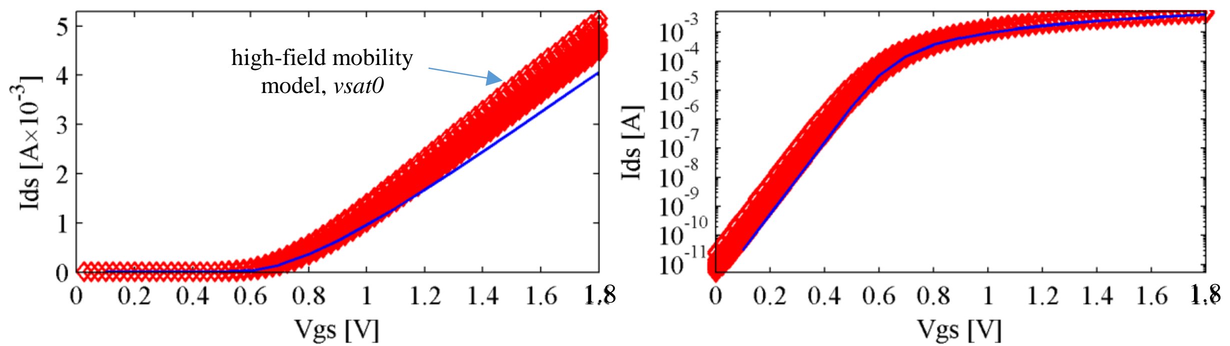

6.2 Current Deviation Extraction Method

To extract $\delta I_d(x_t)$ using the MEDICI tool the following procedure is done:

1. The current with no interface charge is evaluated, I_{d0}.
2. A small charge density Q_t (C/cm^2) is introduced between the interface nodes x_{n-1} and x_{n+1}
3. The new current is measured, I_d.
4. $\delta I_d(x_t)$ is then calculated as $\delta I_d(x_n) = q(I_d\text{-}I_{d0})/(W\times Q_t\times(x_{n+1}-x_{n-1}))$.
5. Repeat steps 2 to 4 for $n = n + 1$.

To understand step 4, let's first understand what happens with the current when we introduce a small quantity of charge in a small rectangle region ($L_t\times W_t$) of the Si-SiO$_2$ interface, along the length (L_t) and width (W_t) of the device. Using (4.9) one has that in a uniform channel device with length equal to Δx, and width equal to W,

$$\frac{\Delta i_x}{i_x} \approx \frac{W_t \times L_t}{W\Delta x}\frac{\eta \Delta Q_t}{Q_{inv}}. \tag{6.1}$$

Hence, the current deviation is directly proportional to the charged area, $L_t\times W_t$, and the charge density introduced in this area, Q_t.

If the potential drop across L_t is negligible, we can generalize (6.1) for a non-uniformly inverted channel and non-uniformly doped channel using (4.36).

$$\text{(4.36):}\ \delta I_d = \frac{f(x)}{\int_0^L f(x)dx}\Delta i_x \Delta x.$$

For only one captured electron, $Q_t = q/L_t^2$, and (6.1) becomes (4.12), repeated below.

$$\text{(4.12):}\ \frac{\Delta i_x}{i_x} = \frac{\eta}{W\Delta_x N_{inv}}$$

Therefore, comparing (6.1) with (4.12) one can normalize the current deviation for one electron using

$$\delta I_{d,\text{1-elec}} = \delta I_{d,Q_t}\frac{q}{Q_t W L_t}, \tag{6.2}$$

where $\delta I_{d,Q_t}$ is the current deviation extracted in the TCAD after the introduction of a charge density, Q_t, in an area given by $W\times L_t$ (here we use $W_t = W$ because in a 2-D device simulation the introduced charge is distributed in the whole width of the device). From step 2, the charge density is introduced between the mesh nodes x_{n+1} and x_{n-1}. Hence, $L_t = x_{n+1}-x_{n-1}$ and (6.2) is the normalization used in step 4.

Figure 6.6 and Figure 6.7 show the results of the normalization using (6.2) for various mesh sizes and charge densities respectively. The simulation was performed in a uniformly doped 2-µm long n-channel device, created for this experiment, with T_{ox} = 2.5 nm, N_a =3e17 and polysilicon gate. Figure 6.6 clearly shows that the normalization works independent of the mesh size as long as the mesh size is small enough to consider the potential drop across x_{n+1} and x_{n-1} negligible. When V_{ds} is high, Figure 6.6 clearly shows that mesh size of 20 nm, 100 nm and 200 nm are too large to account for the large potential drop close to the drain side. Although, when the potential drop is small all the mesh sizes used gives similar results.

Figure 6.7 shows the normalization result for different charge densities with a fixed 4-nm mesh. From the derivations of (6.1) in Chapter 4 the normalization should work as long as the introduced charge density can be considered to cause a small signal perturbation in the channel potential beneath it, otherwise the small signals simplification used in the derivation of (6.1) is no longer valid. The figure shows that the normalization works for different charge densities and does not work for $Q_t/q = 200\times10^{10}$ cm^{-2}. When the charge density is too small, the current deviation is so small that it can barely be detected because of the simulator resolution. This causes the normalized current deviation for one electron to show some quantization effects, as seen when $Q_t/q = 0.02\times10^{10}$ cm^{-2}.

Figure 6.6 – One-electron normalization of the current deviation for different mesh sizes. $Q_t/q = 2\times10^{10}$ cm^{-2}.

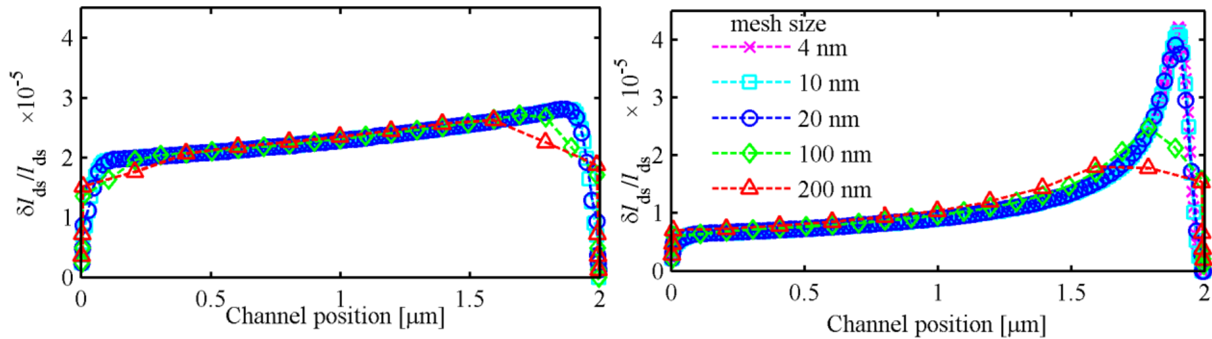

Figure 6.7 – One-electron normalization of the current deviation for different mesh sizes.

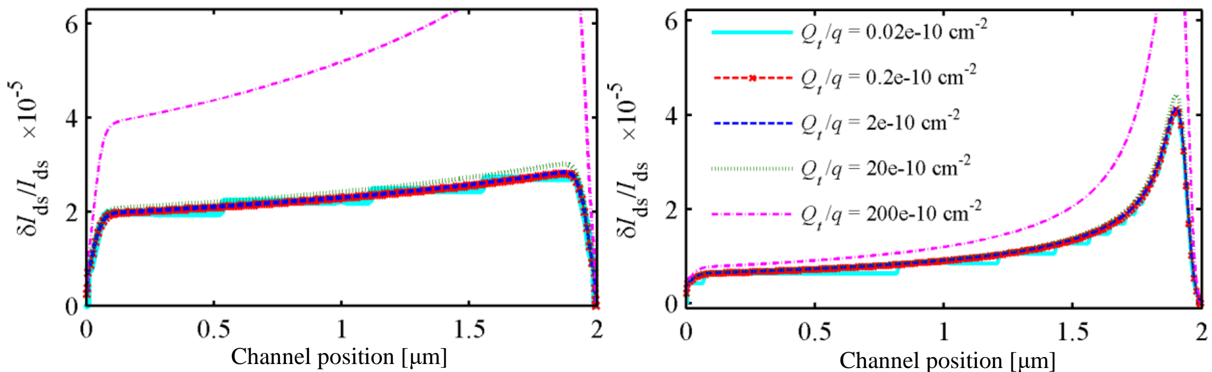

Therefore, (6.2) can be used to calculate the current deviation for any mesh size – as long as the mesh is not so coarse that there is a large potential drop across its nodes – and for any charge density – as long as the charge density is small enough for the potential perturbation stays in the small signal regime and large enough so there is a measurable current deviation.

The TCAD simulation does not account the mobility degradation when a charge is introduced in the Si−SiO_2 interface. Due to this limitation on the TCAD tool, only the number fluctuation part of the δI_d equation, (4.38), is extracted using the above methodology. In Chapter 4 we demonstrated that the mobility degradation caused by a trap is only relevant at strong inversion. As will become clear along this work, the term given by the non-uniformity of the doping, shown in Figure 6.8, is the responsible to increase δI_d in the halo-implanted regions. This term is larger in the halo-implanted regions when the channel is in weak inversion and can be approximated to $1/L$ for all channel positions when the channel is strongly inverted.

Figure 6.8 – Description of the current deviation equation.

In order to account for the mobility fluctuation in the calculation of the current deviation, we use the characteristics of the current deviation equation described above to approximate $\delta I_d(x_t)$ as

$$\delta I_d(x_t) \approx \frac{I_d}{W}\frac{f(x_t)}{\int_0^L f(x_t)dx_t}\left(\frac{\eta(x_t)}{N_{inv}(x_t)}\right) + \frac{I_d}{WL}\alpha\mu(x_t)\,. \tag{6.3}$$

Where the effective $\mu(x)$ is also extracted from TCAD by

$$\mu(x) = \frac{1}{N_{inv}(x)}\int_0^{y_d}\mu(x,y)n(x,y)dy\,, \tag{6.4}$$

and the carrier density by

$$N_{inv}(x) = \int_0^{y_d} n(x,y)dy\ . \tag{6.5}$$

After extracting the quantities from the TCAD simulation, the only fitting parameters left to fit the measured data with our proposed model, equations (5.1) to (5.8), are the N_{tr}/γ and the α parameter.

6.3 Current Deviation

In Section 5.4, we showed that there is a clear difference between the behavior of the variability of large and small channel devices. The variability of large devices has a larger dependence with both V_{ds} and V_{gs} than the variability of short channel devices. We have addressed this difference in Section 5.4 as being caused by the difference in the carrier distribution along the channel and by the halo regions. This behavior of the variability is clarified when analyzing the current deviation extracted using the TCAD simulation and (6.3).

We extracted the current deviation for long and short channel devices from the 140-nm TCAD deck, carefully tuned as demonstrated above. For this experiment, we simulate n-channel devices with $L = 8$ µm, $L = 0.32$ µm and $L = 0.14$ µm, to represent different device geometries. The current deviation is analyzed for four different bias configurations: linear region, weak inversion, saturation and weak inversion with high V_{ds} applied.

Long Channel (8 µm)

Figure 6.9 shows the 2-D cross section of the net doping gradient of a long channel device. In the figure, the dark-blue regions are strongly doped regions. It demonstrates that the regions with halo implantation represent a small amount of the channel and are far apart.

Figure 6.9 – 2-D cross-section of a long channel device (1 µm), showing the net doping gradient. Halo-implanted regions are far apart.

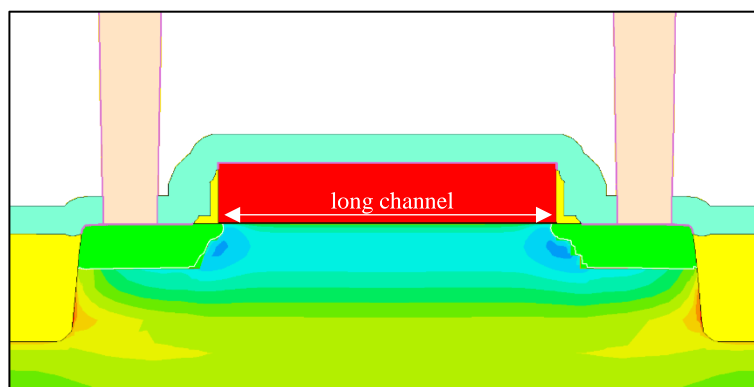

The current deviation extracted for the long channel device is shown from Figure 6.10 to Figure 6.13. Figure 6.10 shows that using high V_{gs} and low $V_{ds,}$ the impact on a large device is almost constant from source to drain, confirming the uniformly-charged channel consideration in Section 5.2. Analyzing the equation in Figure 6.8, when V_{gs} is high, the term highlighted in blue, which

accounts for the non-uniformity in the doping concentration, is almost constant along the channel and approximately $1/L$. In addition, the term in the parentheses can also be considered constant, because V_{ds} is low.

Figure 6.11 shows a much larger impact at the halo regions when V_{gs} is low and the device is operated close to the weak inversion regime, where the term highlighted in blue increases the current deviation at highly doped regions.

Figure 6.12 shows the device in the saturation regime, with high V_{gs} and high V_{ds}. On this condition the trap with the highest impact is situated at the onset of the pinch-off region due to the small number of carriers at the drain side (η/N_{inv} is large) and because the drain-side halo region is in weak inversion (blue highlighted term is large).

When decreasing V_{gs} and keeping V_{ds} high, the term $\eta(x)/N_{inv}(x) \approx \left(\left(kT/q^2\right)(C_{ox}+C_D)\right)^{-1}$ – according to Section 4.5 – hence it is saturated along the channel and the difference of δI_d as a function of the trap position is given only by the influence of the halo region, as shown in Figure 6.13. The figure also shows that the impact at the drain side halo is smaller; this is caused by the lowering of the halo-implanted region barrier induced by V_{ds}.

Therefore, the high impacts at small regions of the channel, shown in Figure 6.11 to Figure 6.13, are the responsible for the strong increase in the K value – hence the variability – when the large channel device operates in weak inversion or in saturation.

Figure 6.10 – Normalized impact vs. channel position, high V_{gs}, low V_{ds}, L = 8 µm.

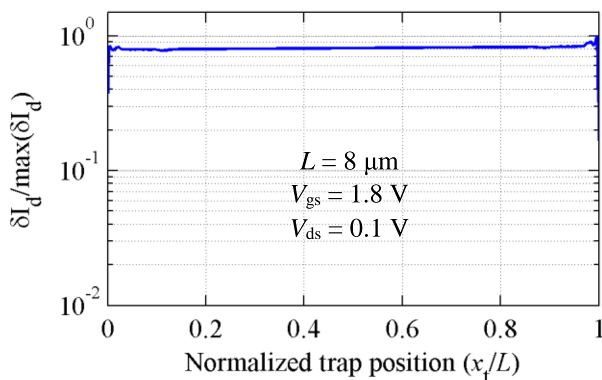

Figure 6.11 – Normalized impact vs channel position, low V_{gs}, low V_{ds}, L = 8 µm.

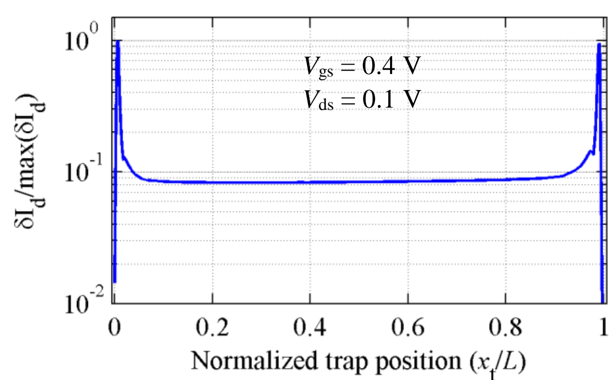

Figure 6.12 – Normalized impact vs. channel position, high V_{gs}, high V_{ds}, L = 8 µm.

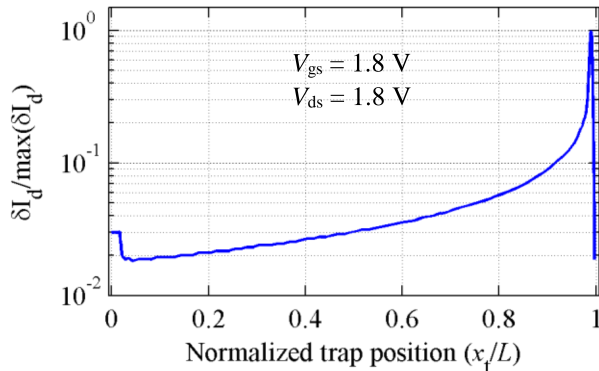

Figure 6.13 – Normalized impact vs. channel position, low V_{gs}, high V_{ds}, L = 8 µm.

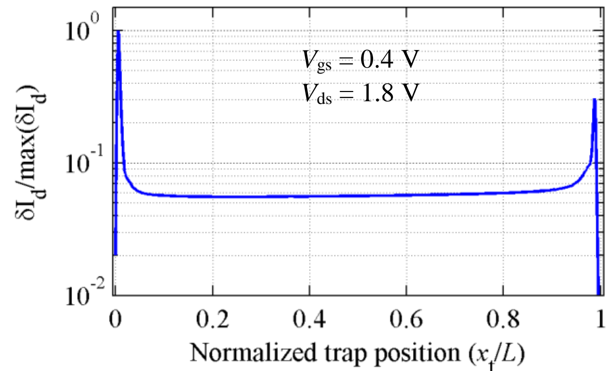

Short Channel (0.32 µm)

Figure 6.14 shows the cross section of the net doping gradient of a 0.32-µm device, representing a short channel device with the halo-implanted regions very close to each other.

Figure 6.14 – 2-D cross-section of a 0.32-µm device showing the net doping gradient. Halo-implanted regions are very close to each other.

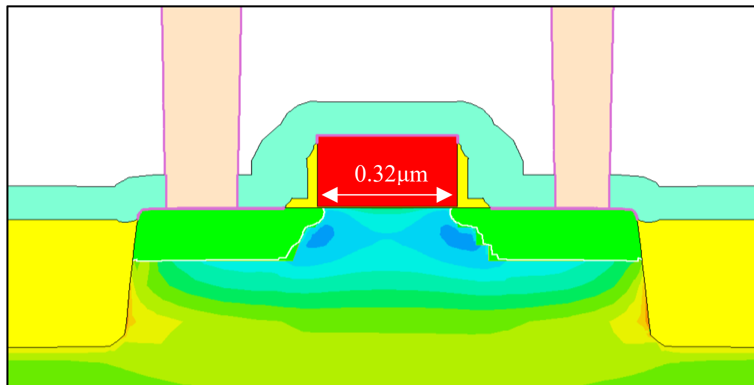

The current deviation extracted for the short channel device is shown from Figure 6.21 to Figure 6.24. The current deviation as a function of the trap position is very similar to the 8-µm long device. However, it has two main differences. In weak inversion, the peaks in δI_d at the halo-implanted regions represent a large percentage of the channel, which in turn makes K weaker dependent with V_{gs} than the 8-µm device. In saturation, Figure 6.17, the difference from the impact at the onset of the pinch-off to the impact close to the source are smaller than this difference in the 8-µm long device. This is due to the velocity saturation, which makes the carrier's density at the onset of pinch-off to be a function of the channel length (as shown in

Figure 6.19). Therefore, the lower peak in the saturation condition and the fact that the peak also represents a large percentage of the channel makes the variability to also have a smaller dependency with V_{ds}.

Figure 6.15 – Normalized impact vs. channel position, high V_{gs}, low V_{ds}, $L = 0.32$ µm.

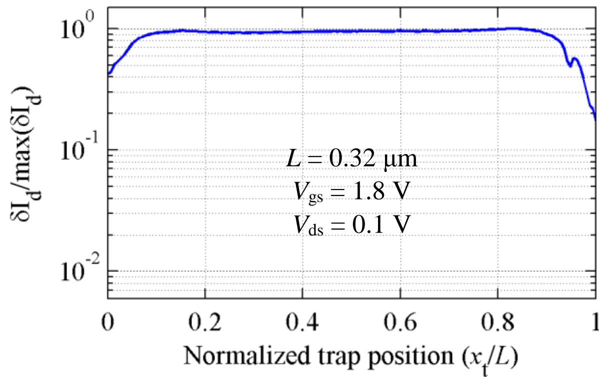

Figure 6.16 – Normalized impact vs channel position, low V_{gs}, low V_{ds}, $L = 0.32$ µm.

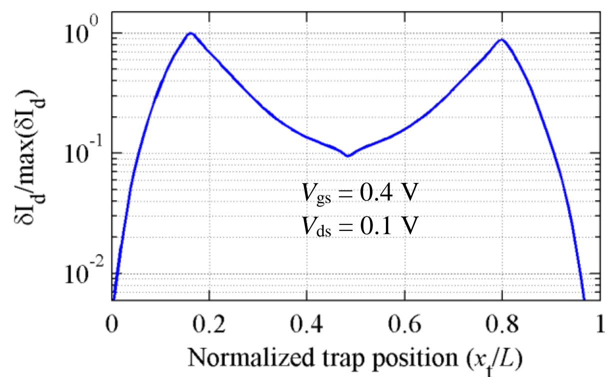

Figure 6.17 – Normalized impact vs. channel position, high V_{gs}, high V_{ds}, $L = 0.32$ µm.

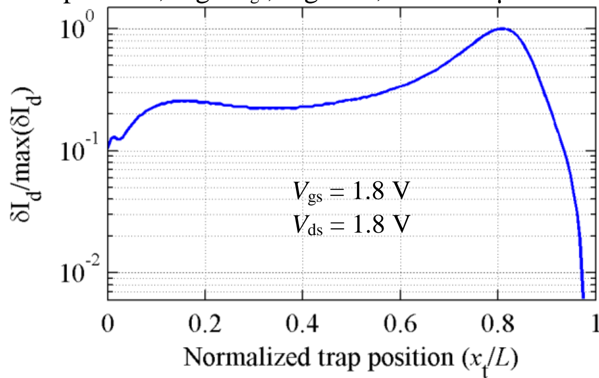

Figure 6.18 – Normalized impact vs. channel position, low V_{gs}, high V_{ds}, $L = 0.32$ µm.

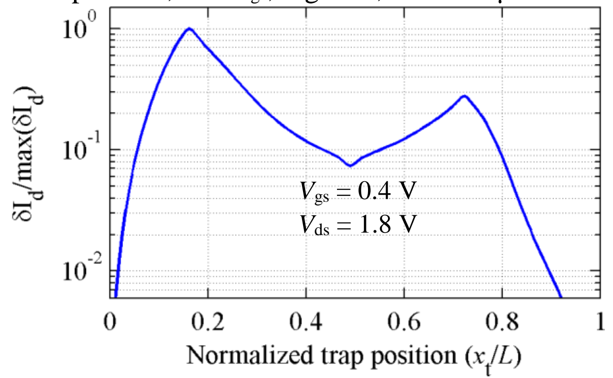

Figure 6.19 – Carriers density as a function of the normalized channel position for three different channel lengths. $V_{gs} = 1.8$ V and V_{ds}=1.8 V.

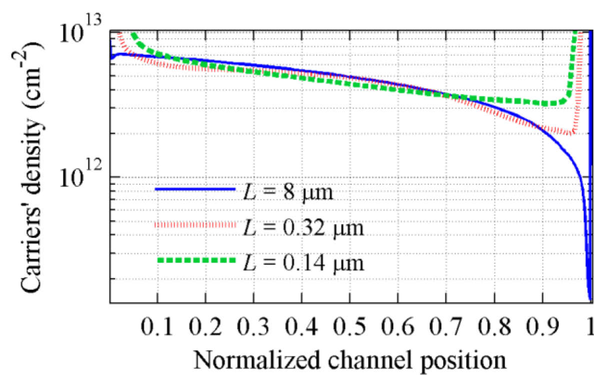

Short Channel (0.14 µm)

Figure 6.20 – 2-D cross-section of a 0.14-µm device showing the net doping gradient. Halo-implanted regions are overlapped.

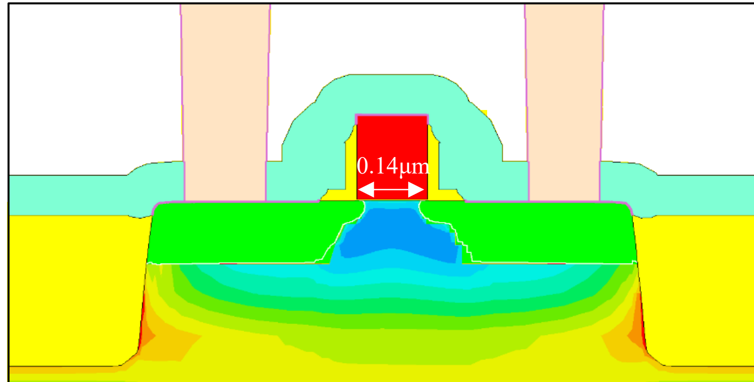

The current deviation extracted for the short channel device is shown from Figure 6.21 to Figure 6.24. For the small channel device, the comparison between Figure 6.21 and Figure 6.23 shows that, the change of V_{ds} cause a minor change on the impact of the trap close to the drain.

In such small channel device, the halo regions are overlapped. Hence, we do not see the behavior of the current deviation present in the halo regions. However, for low V_{gs} the effect of the depletion region of the source and drain affects δI_d, creating the behavior shown in Figure 6.22 and in Figure 6.24, which slightly increases the value of K.

Figure 6.21 – Normalized impact vs. channel position, high V_{gs}, low V_{ds}, $L = 0.14$ µm.

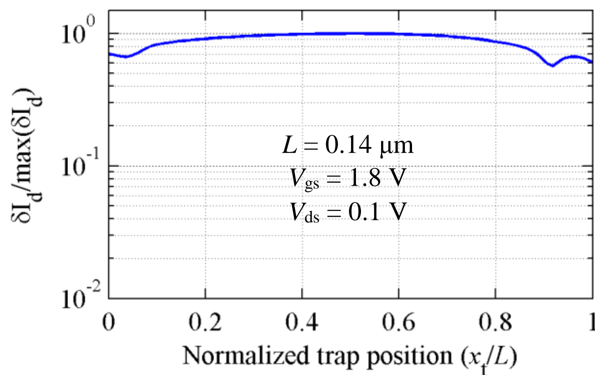

Figure 6.22 – Normalized impact vs channel position, low V_{gs}, low V_{ds}, $L = 0.14$ µm.

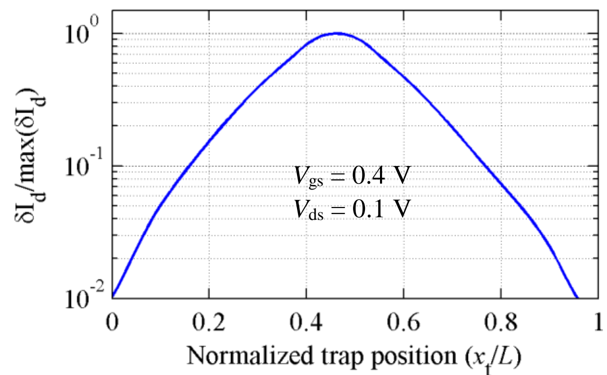

Figure 6.23 – Normalized impact vs. channel position, high V_{gs}, high V_{ds}, L = 0.14 µm.

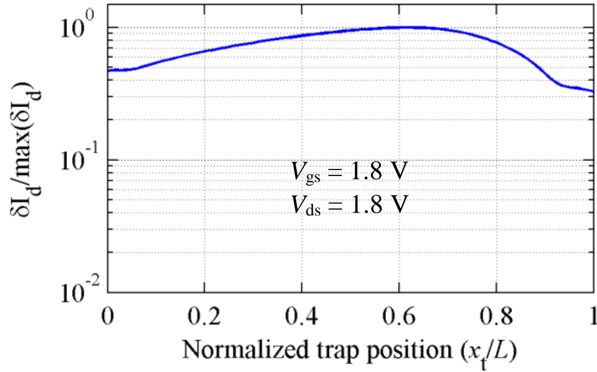

Figure 6.24 – Normalized impact vs. channel position, low V_{gs}, high V_{ds}, L = 0.14 µm.

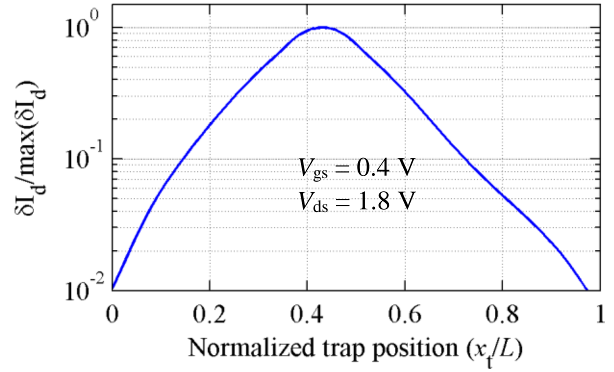

6.4 Model Fit for n-channel devices in 140-nm node

The next step is to use the current deviations extracted with the help of the TCAD tool, shown above, to calculate the proposed model equations, (5.1) to (5.8), and to test the validation of the model for different bias configuration. After extracting the quantities from the TCAD simulation, there are two parameters left to be defined, N_{tr}/γ and α, which are carefully chosen to fit the model with the measured data. To test the validation of the proposed model we, compare the model with the measured data from devices with different channel lengths and using different gate and drain bias. Below we show the comparison of devices fabricated in a 140-nm CMOS technology with $W\times L$ (µm^2) given by: 8×0.14, 8×0.32, 8×1 and 8×8. Each geometry has 43 measured devices. We chose wide devices with W = 8µm, to have a smaller uncertainty on the extraction of the Expected value, Variance, K and $\sigma[\ln(S_{id})]$.

L = 0.14 µm

The comparison between the measurements and our model for devices with L = 0.14 µm is shown from Figure 6.25 to Figure 6.28. To calculate the model, we use a constant trap density of N_{tr}/γ = 1.3×10^9 cm^{-1}eV^{-1} and a mobility degradation coefficient of $\alpha = 0.8\times10^{-15}$ Vs. The extracted values from the measured data are represented by symbols and the values calculated – using the proposed model – are represented by dashed lines. Figure 6.25 show the comparison of the extracted K value from the measured data and the K calculated using (5.7). Figure 6.26 shows the comparison of $\sigma[\ln(S_{id})]$, calculated using (5.6). According to (5.6), K and $\sigma[\ln(S_{id})]$ have similar behaviors. The figures show that the behavior of the current deviation shown above and the proposed model can nicely predict the behavior of the LF noise variability of the 0.14-µm device as a function of V_{gs} and V_{ds}.

Figure 6.27 and Figure 6.28 show the comparison of the measured data and the calculated values using (5.1) and (5.2) for the Expected value and Variance of the LF noise respectively. The figures also show a good fit between the model and the measured data for both Expected value and Variance.

Figure 6.25 – Measured versus calculated K. L=0.14 µm.

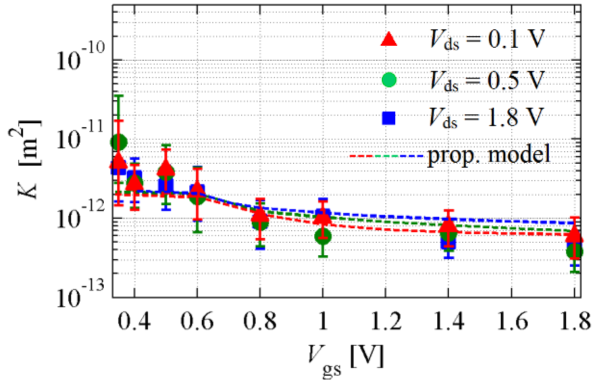

Figure 6.26 – Measured versus calculated Standard Deviation. W = 8 µm, L = 0.14 µm.

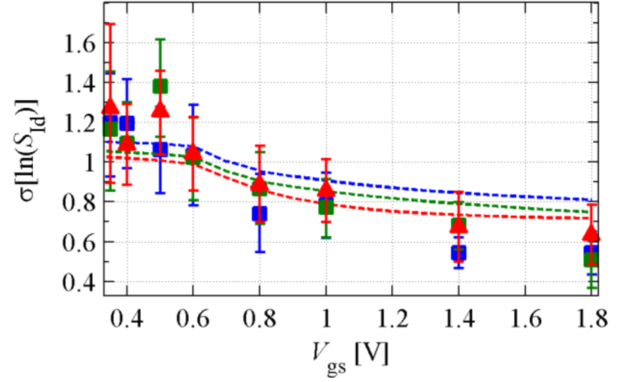

Figure 6.27 – Measured versus calculated Expected value. L=0.14 µm.

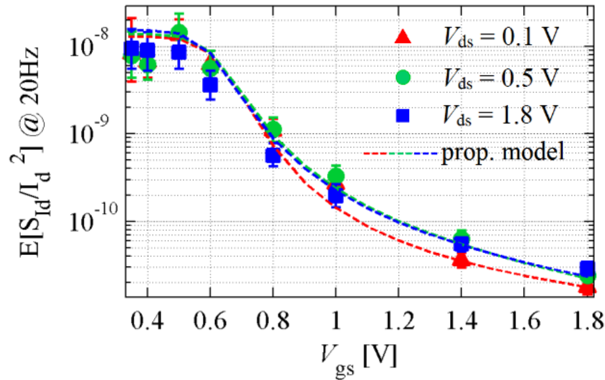

Figure 6.28 – Measured versus calculated Variance. L = 0.14 µm.

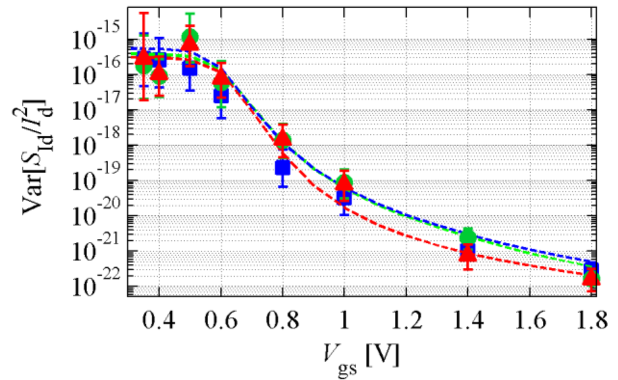

***L* = 0.32 µm**

For the 0.32-µm long device, the comparison between the measurements and our model is shown from Figure 6.29 to Figure 6.32. Using a constant trap density of $N_{tr}/\gamma = 1.1\times10^9$ cm^{-1}eV^{-1} and a mobility degradation coefficient of $\alpha = 0.8\times10^{-15}$ Vs our proposed model provides a very good prediction of the Expected value and Variability of the noise.

Figure 6.29 – Measured versus calculated Expected value. L=0.32 µm.

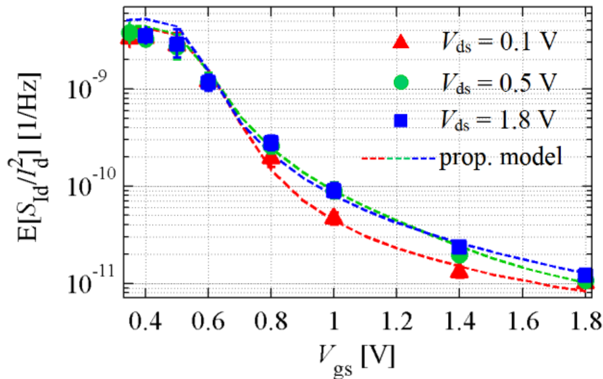

Figure 6.30 – Measured versus calculated Variance. L=0.32 µm.

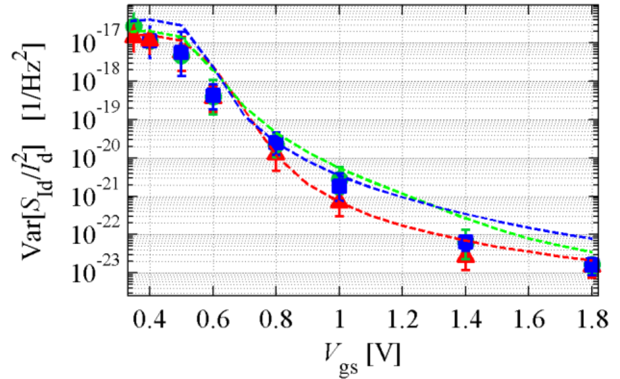

Figure 6.31 – Measured versus calculated K. L=0.32 µm.

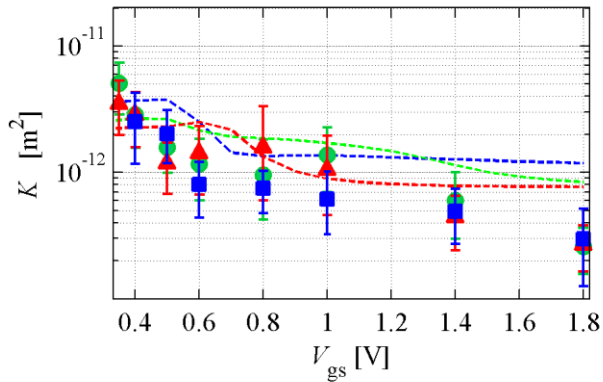

Figure 6.32 – Measured versus calculated Standard Deviation. L=0.32 µm.

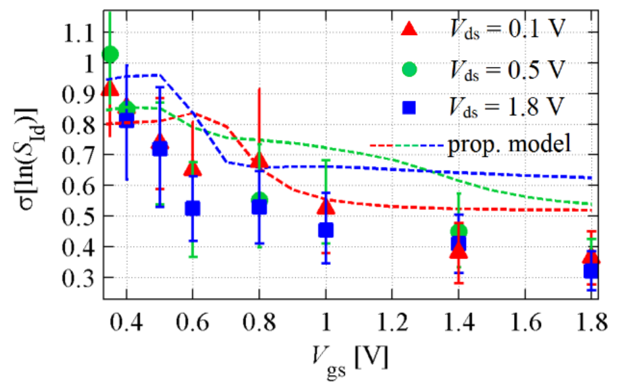

L = 1 µm

For the 1-µm long device, the comparison between the measurements and the proposed model is shown in Figures 6.33 − 6.36. The proposed model is calculated using a constant trap density of $N_{tr}/\gamma = 1.1\times10^{9}$ cm^{-1}eV^{-1} and a mobility degradation coefficient of $\alpha = 0.8\times10^{-15}$ Vs.

Figure 6.33 – Measured versus calculated Expected value. L=1 µm.

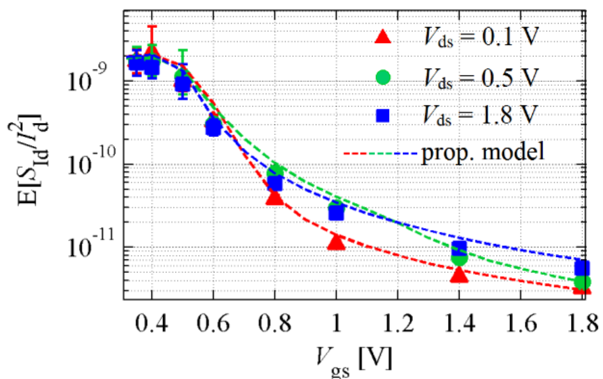

Figure 6.34 – Measured versus calculated Variance. L=1 µm.

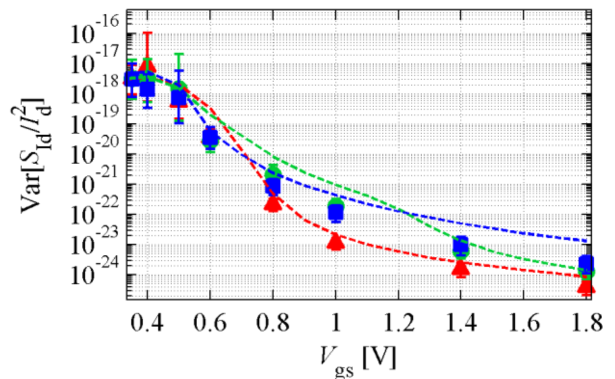

Figure 6.35 – Measured versus calculated K. L=1 µm.

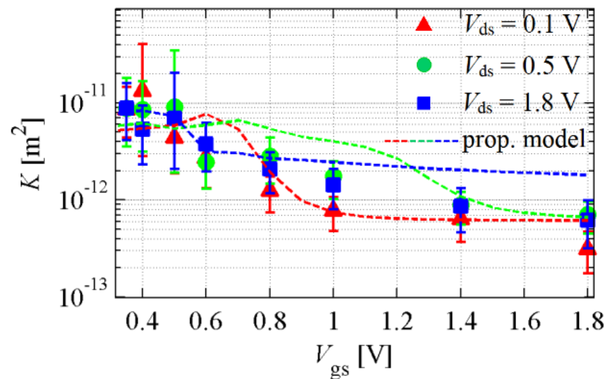

Figure 6.36 – Measured versus calculated Standard deviation. L=1 µm.

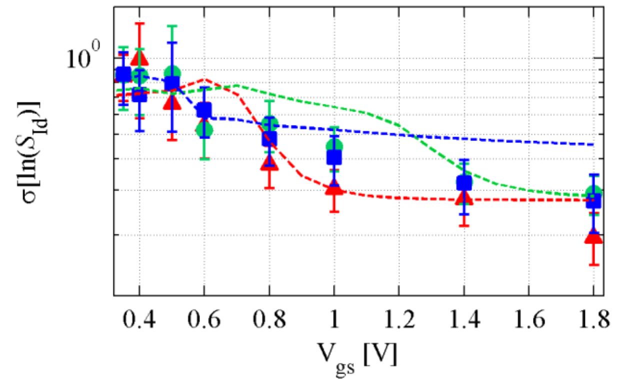

L = 8 µm

For the 8-µm long device, the comparison between the measurements and the proposed model is shown in Figures 6.37 − 6.40 using the data of 43 devices with $WL = 8\times8\mu m^2$. The model provides a very good fitting using a constant trap density of $N_{tr}/\gamma = 1.1\times10^9$ cm^{-1}eV^{-1} and a mobility degradation coefficient of $\alpha = 0.8\times10^{-15}$ Vs. Figure 6.37 and Figure 6.38 show the Expected value and Variance of the LF noise respectively. The dashed lines in the figures are the fitting calculated using (5.1) and (5.2).

The behavior of δI_d described in Figure 6.10 to Figure 6.13 can explain the bias dependence of K for large devices shown in Figure 6.39. Analyzing Figure 6.39 one can see that for V_{ds} = 0.1 V, when V_{gs} decreases the value of K increases due to the increase of the influence of the halo regions, as shown in Figure 6.13. For V_{ds} = 0.5 V, K increases as V_{gs} decreases, first because of the decrease of the carrier concentration at the drain side and then, due to the influence of the halo regions as V_{gs} approaches the threshold voltage, as shown in Figure 6.12 and Figure 6.13.

Figure 6.37 – Measured vs calculated Expected value. L=8 µm

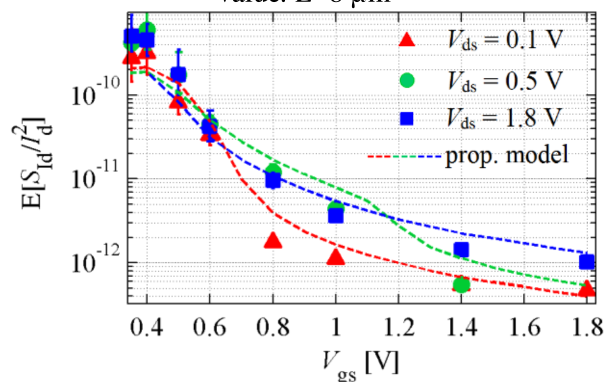

Figure 6.38 – Measured vs calculated Variance. L=8 µm

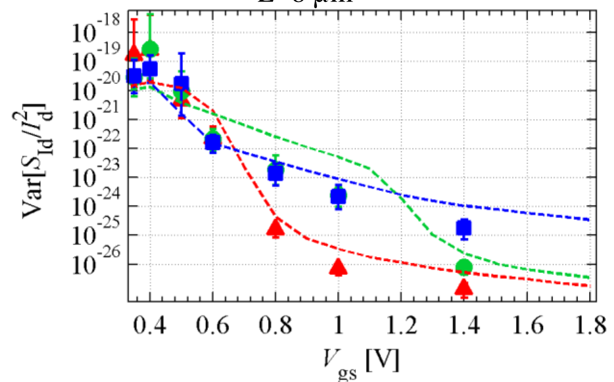

Figure 6.39. – Measured versus calculated K. L=8 μm

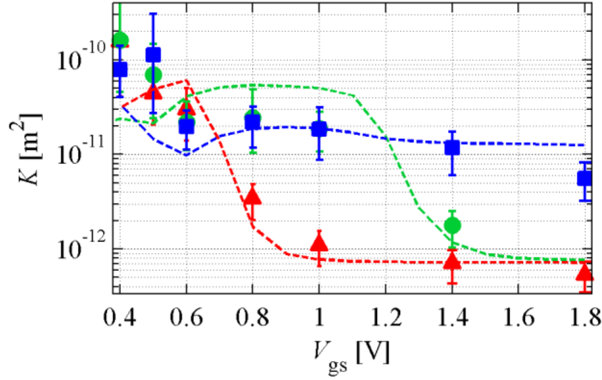

Figure 6.40 – Measured vs calculated Standard Deviation. L=8 μm

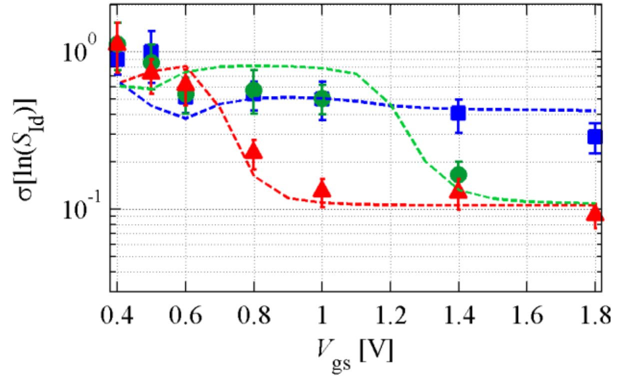

6.5 Model Fit for p-channel devices in 140-nm node

As we already analyzed, the p-channel device has a different noise behavior than the n-channel device. Using the proposed model, we explain this difference with the trap density behavior as a function of the energy. For n-channel devices, the trap density can be considered constant and, for the p-channel, the trap density varies strongly with the energy. Moreover, Figure 6.41 shows that the difference between the K value for different channel length devices are not as large as the difference found in n-channel devices. We can understand this by analyzing Figure 6.42, which shows that the halo-implanted regions have a smaller impact when compared to the n-channel device in Figure 6.11.

Figure 6.41 – Extracted K of 43 PMOS 140-nm node devices with V_{ds} = 0.5 V.

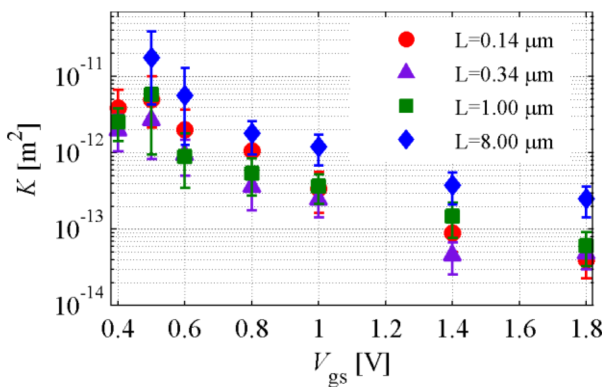

Figure 6.42 – Normalized impact versus channel position for an 8-μm long p-channel device with low V_{gs} and low V_{ds}.

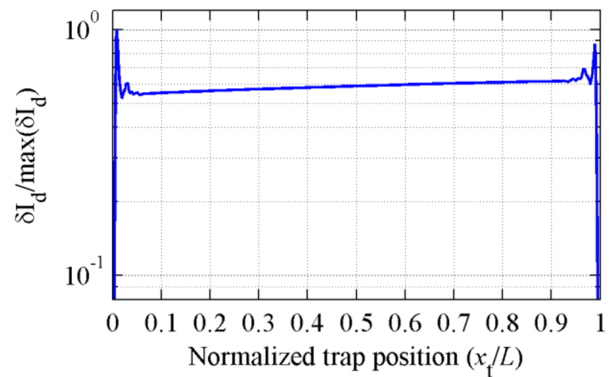

To account the energy dependency, for all p-channel devices geometries analyzed, we assume that the trap density is given by

$$\frac{N_{tr}(E)}{\gamma} = D_l + D_h e^{-(E-E_h)/l_c} \tag{6.6}$$

where, $l_c = (E_m - E_h)/\log(D_h/D_l)$, $D_h = 6.5\times10^{10}$ cm^{-2}eV^{-1}, $D_l = 3.6\times10^{8}$ cm^{-2}eV^{-1}, $E_h = -0.76$ eV and $E_m = -0.54$eV. The resultant distribution is shown in Figure 6.43. We also demonstrate in the figure a

comparison with the trap density used in the NMOS analysis. Moreover, the mobility degradation coefficient used for all dimensions is $\alpha = 1\times10^{-15}$ Vs.

Figure 6.43 – Trap distribution used for the calculation of PMOS devices.

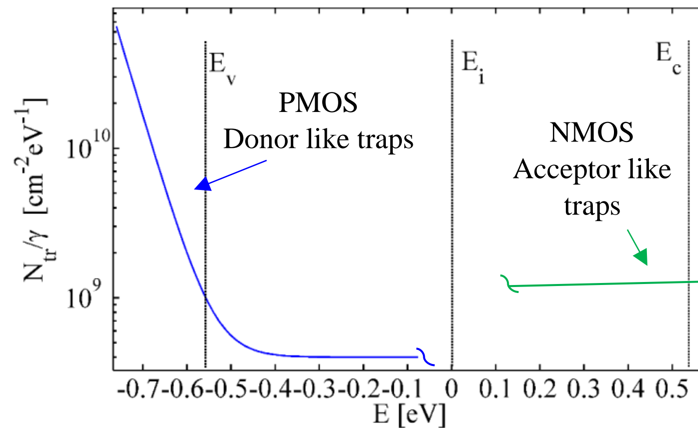

Different authors did also observe an increased trap density close to the edges of the Si bandgap, leading to a defect band or U-shape trap distribution. For instance, it was observed in the context of NBTI in SiGe pFETs with a high-k stack (Scofield, et al., 1994), as well as it agrees to recent RTN noise measurements by other groups (Nour, et al., 2016). It was also observed in the context of transient capacitance spectroscopy (Wang, 1980), as well as in charge pumping in different technologies and using different techniques. See, for instance, the work of Kim et al. (2011) and references therein.

To account the trap density as a function of energy in the integrals of (5.1), (5.2) and (5.7), the trap density must be converted as a function of channel position. An example of such translation is given in Figure 6.44, for three different bias configurations. The conversion is done by extracting the holes quasi-Fermi energy as a function of the channel position and then by applying it in (6.6).

Figure 6.44 – Conversion from trap density as a function of quasi-Fermi level to trap density as a function of channel position.

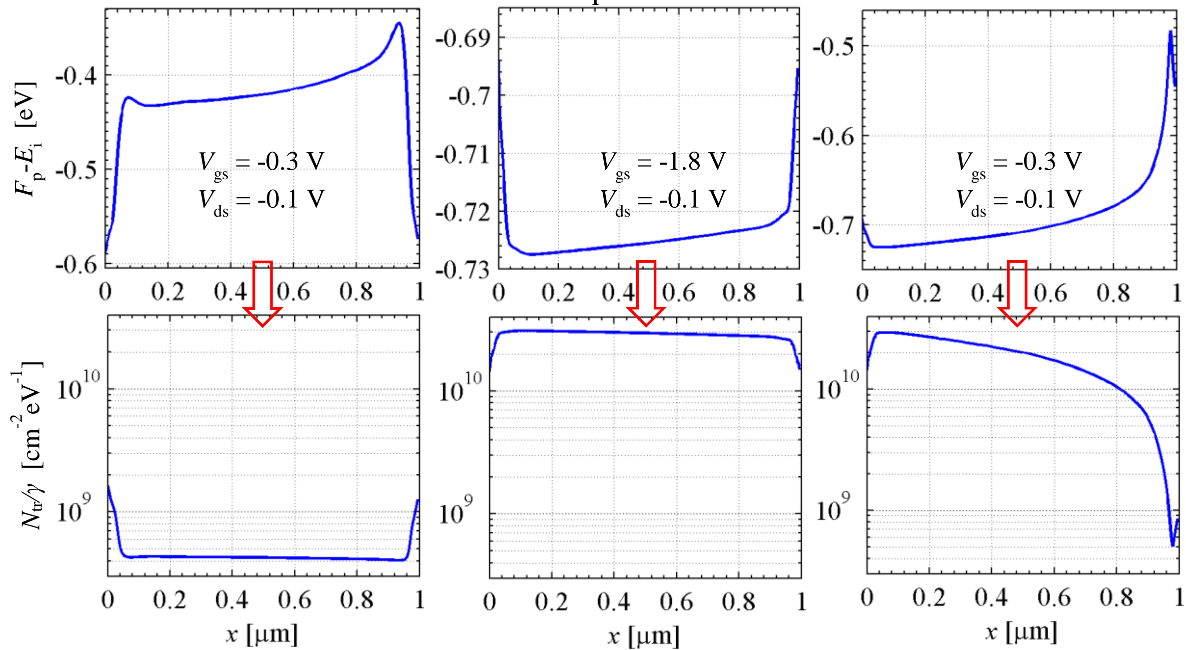

Using the parameters and the methodology explained above we compare our proposed model to the measured data. For this analysis, we use the measurements of 48 PMOS devices for each dimension ($8\times1\mu m^2$, $8\times0.316\mu m^2$ and $8\times0.14\mu m^2$). The results of this comparison are shown from Figure 6.45 to Figure 6.47 for the 1-µm, 0.32-µm and 0.14-µm long devices respectively. The comparison show very good agreement between our model and the measured data. In the figures, the dashed lines are calculated using our proposed model and the symbols are the data extracted from the LF noise measurements.

L = 1 µm

Figure 6.45 – LFN Measurements versus proposed model, for p-channel devices with L=1µm.

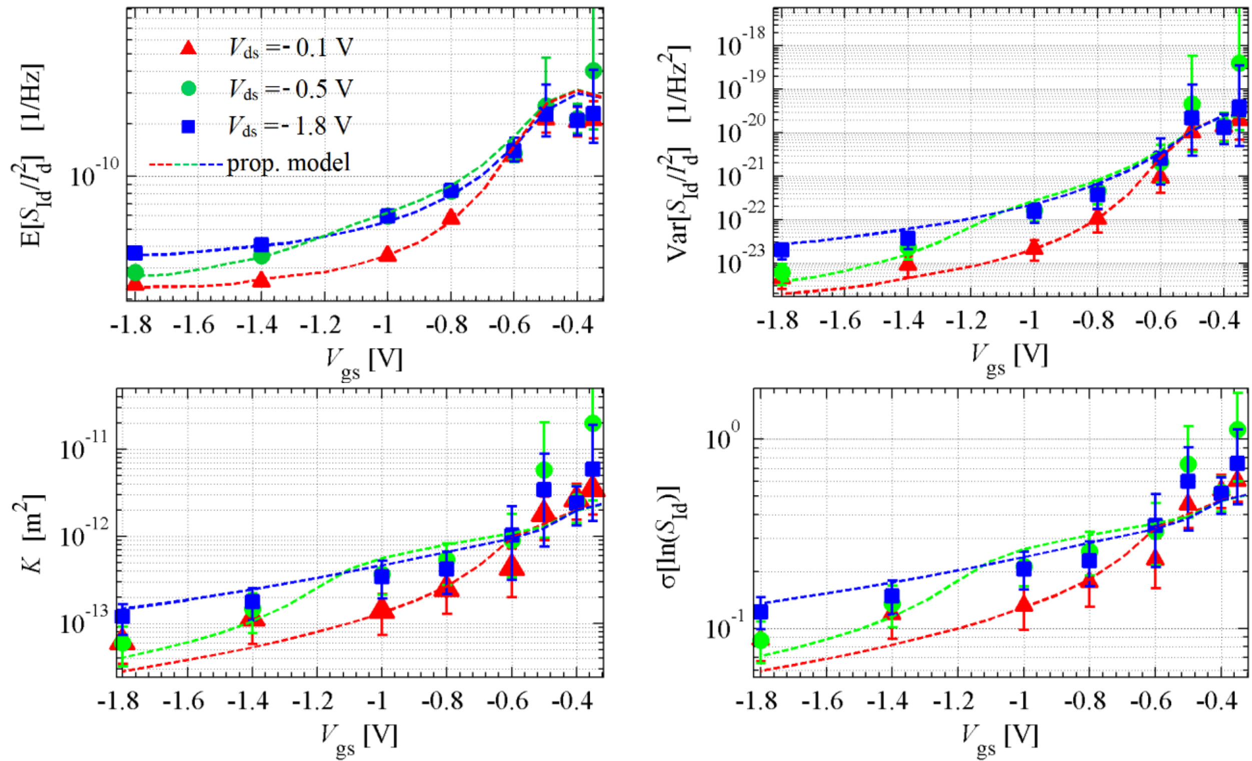

L = 0.336 µm

Figure 6.46 – LFN Measurements versus proposed model, for p-channel devices with L=0.316µm.

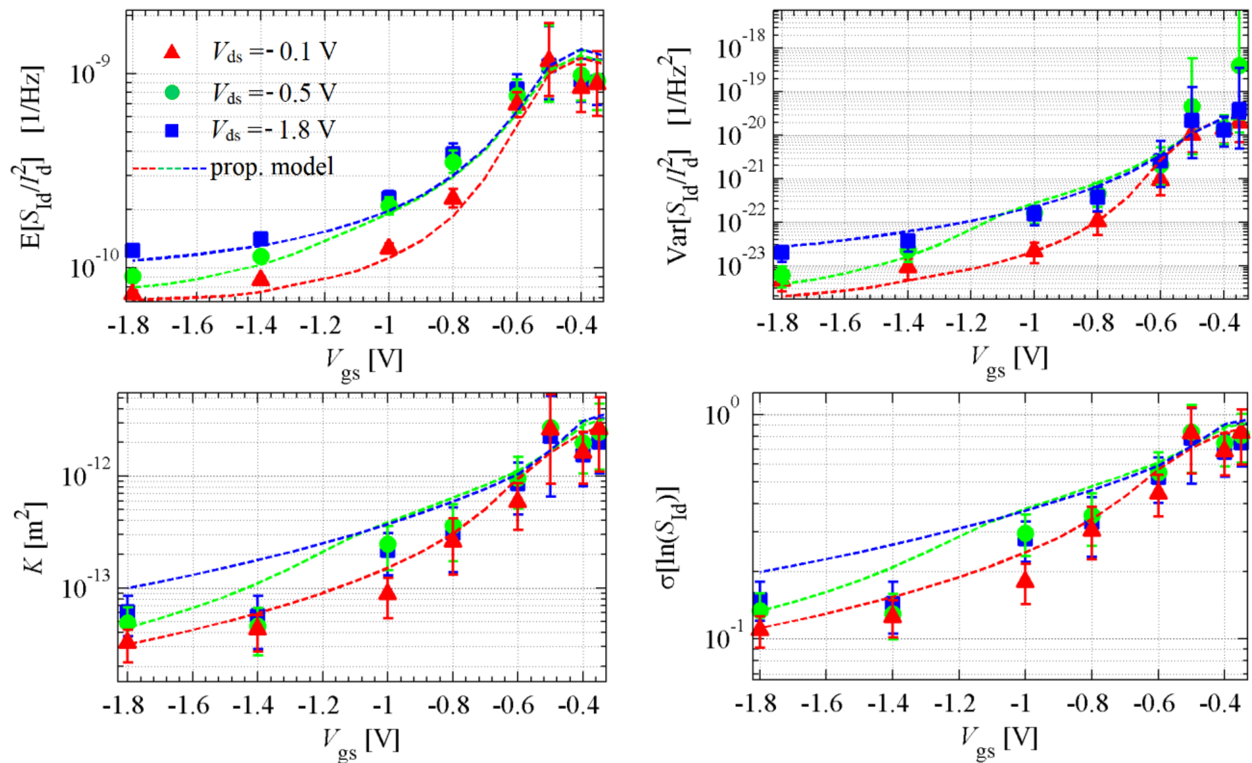

L = 0.14 μm

Figure 6.47 – LFN Measurements versus proposed model, for p-channel devices with L = 0.14 μm.

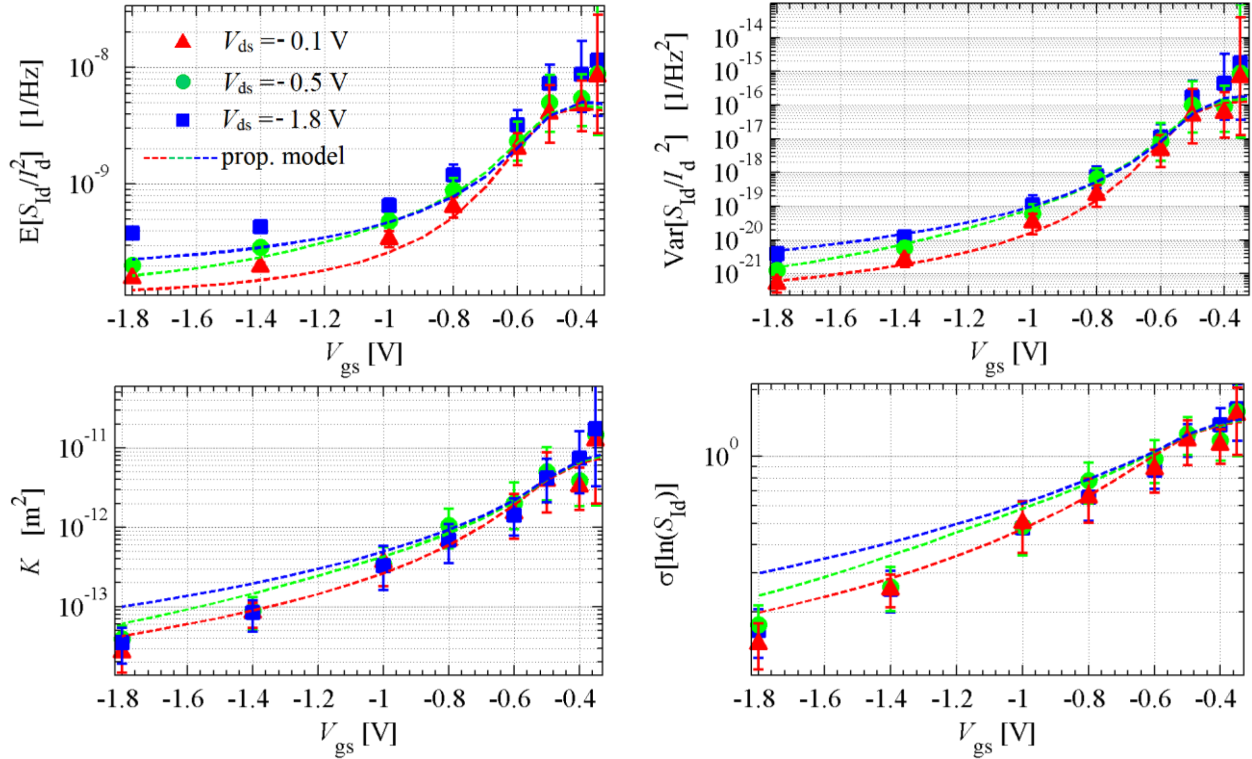

Figure 6.48 shows that a better fit, for the 0.14-μm devices can be achieved by using trap density that is 20% higher than the one shown in Figure 6.43.

Figure 6.48 – LFN Measurements versus proposed model using the trap density 20% higher, for p-channel devices with L=0.14μm.

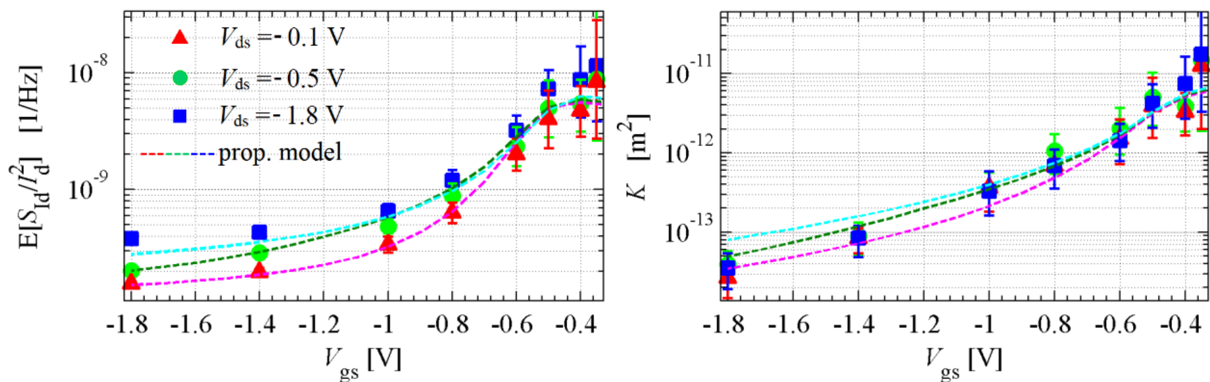

6.6 Model Fit for n-channel devices in 40-nm node

We also tested the model using the TCAD deck of the 40-nm technology. The results of the comparison between the measurements and the calculated values using the proposed model are shown in Figures 6.49 – 6.51. In the calibration process of the DC-IV characteristic of the 40-nm TCAD deck, we could not achieve a perfect calibration. Because of this, we believe that the proposed model

for the 40-nm technology does not give a fit as good as the fit achieved for the 140-nm technology. Anyhow, it predicts very well the behavior of the noise statistics, such as the increase in two order of magnitude of K when the 9-µm long device is operated in weak inversion. The fittings were done using a constant trap density of $N_{tr}/\gamma = 1.7\times10^{9}$ cm^{-1}eV^{-1} and a mobility degradation coefficient of $\alpha = 0.8\times10^{-15}$ Vs.

L = 9 µm

Figure 6.49 – LFN Measurements versus proposed model, for 9-µm long n-channel devices in 40-nm technology.

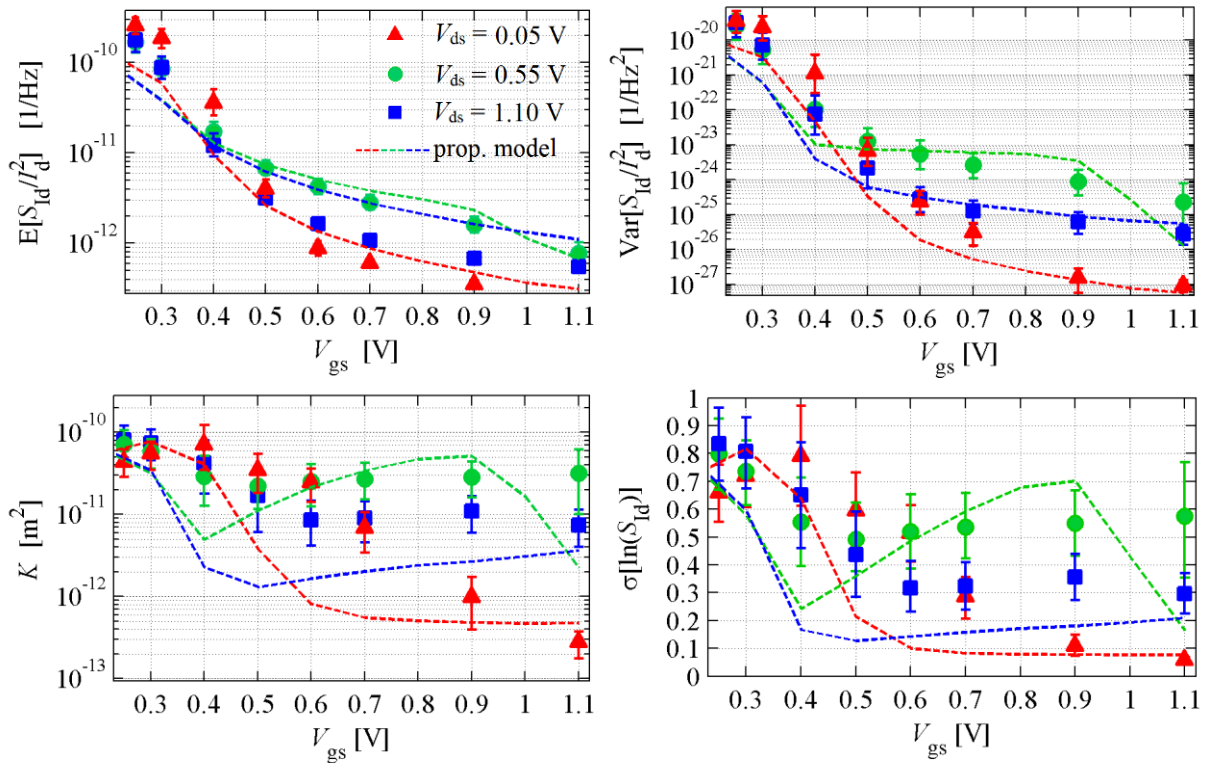

L = 0.9 µm

Figure 6.50 – LFN Measurements versus proposed model, for 0.9-µm long n-channel devices in 40-nm technology.

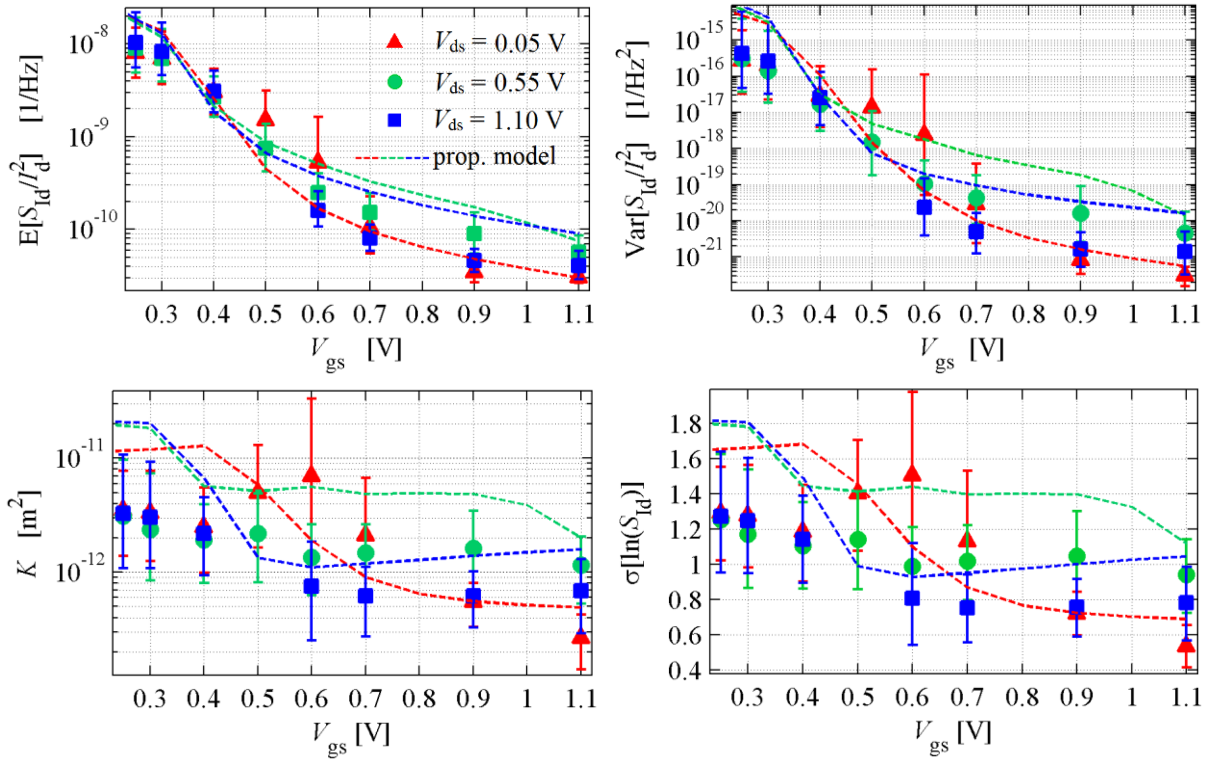

L = 0.04 µm

Figure 6.51 – LFN Measurements versus proposed model, for 0.04-µm long n-channel devices in 40-nm technology.

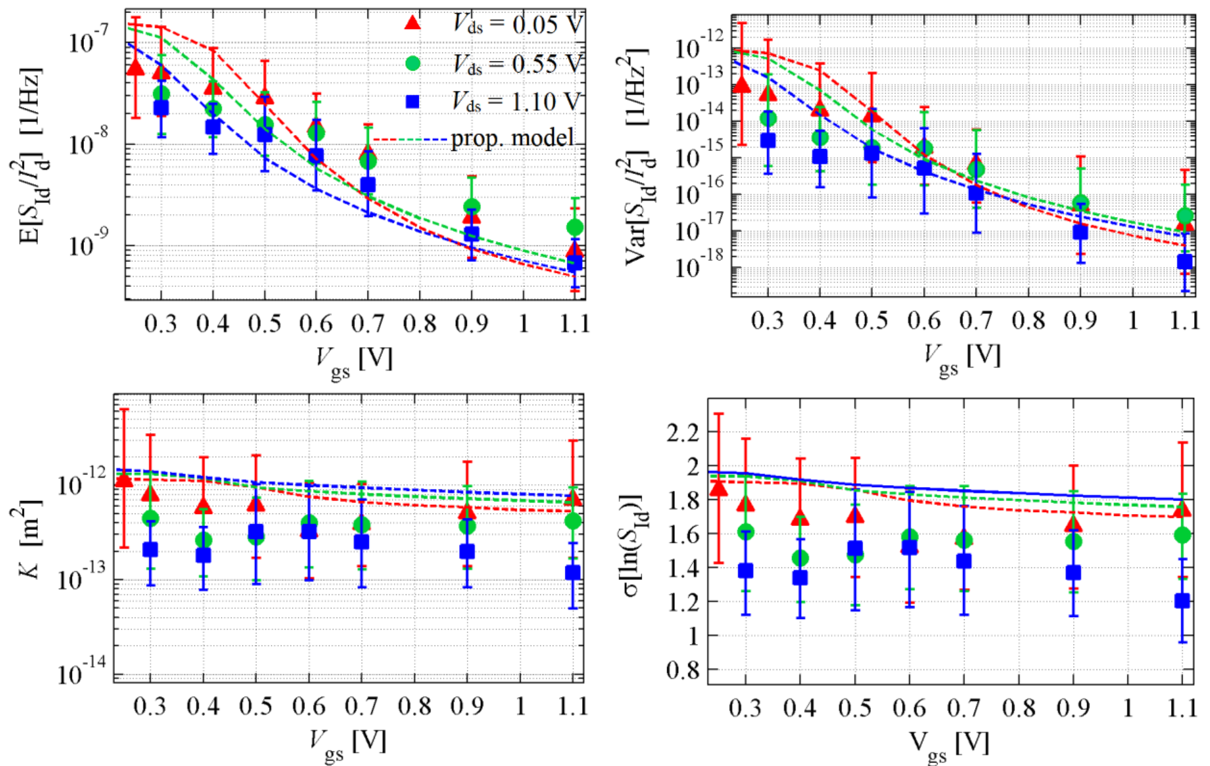

6.7 Discussion

This chapter shows that our proposed model can be used to calculate the statistics of the LF noise for both large and small devices and is well suited for both $1/f$ like and Lorentzian dominated spectra. The fitting with the measured data was done using only two parameters, N_{tr}/γ and α. The other physical quantities, used to calculate δI_d, were extracted from TCAD simulations, which reinforce the physics-based characteristic of our proposed model.

The difference in the behavior of LFN variability for small and large devices with the bias voltage was attributed to the presence of the halo implant and the different dependence of the carrier density at the drain side with V_{ds}, for long and short devices.

Moreover, the difference in the noise behavior for NMOS and PMOS devices is explained using our proposed model and considering the trap density of PMOS devices to be strongly dependent on the energy, while the NMOS device has a trap density that is weakly dependent on the energy.

To have a better fit, a 15%-30% variation on the trap density between large devices and short devices was considered in the 140-nm technology. This can be an evidence of a slightly increase on the trap density close to the source and drain. Although, this small difference can be also explained due to discrepancies between the TCAD devices and the measured devices.

Furthermore, despite our model be derived from RTN only, we do not mean that RTN is the only noise mechanism present in the transistor. However, the experimental results and analysis done in this chapter indicate that it is the major noise mechanism, and that it is adequate to explain and model the experimental observations. In Section 8.2 we briefly comment how other noise sources can possibly affect the left tail of the noise distribution in very small area devices.

Finally, the proposed model can be easily transformed into a compact model, suited for circuit simulators, by just modeling the current deviation calculation in (5.3). In the next Chapter, we discuss some possibilities for implementing the proposed model in a compact model.

7 ANALYTICAL ANALYSIS & COMPACT MODELING

In this chapter, we discuss the possibilities to formulate our proposed model into a compact analytical form that can be incorporated into standard compact electrical simulators.

7.1 Uniformly doped devices

In Section 5.1 we have shown that the proposed model for the LFN Expected value in uniformly doped devices (Equation (5.10)) is similar to the proposed by Hung et al. (1990) (Hung, et al., 1990) for the total LFN (Equation (5.11)). The work of Hung et al. (1990) proposed an analytical and a compact calculation for (5.11). The same methodology can be used in our proposed model. For convenience (5.10) and (5.11) are repeated below.

$$\text{(5.10):}\quad E\left[S_{Id}(f)\right]=2\frac{kT}{\gamma f}\frac{I_d^2}{WL^2}\int_0^L\left(\frac{\eta(x)}{N_{inv}(x)}+\alpha\mu(x)\right)^2 N_{tr}(E_{Fn})dx\,.$$

$$\text{(5.11):}\quad S_{Id}(f)=\frac{kT}{\gamma_a f}\frac{I_d^2}{WL^2}\int_0^L\left(\frac{\eta(x)}{N_{inv}(x)}+\alpha\mu(x)\right)^2 N_{t}(E_{Fn})dx\,.$$

In the derivation of (5.10) we use that for a uniformly doped device the normalized current deviation is simplified to

$$\frac{WL}{I_d}\delta I_d=\delta\tilde{I}_d=\left(\frac{\eta}{N_{inv}}+\alpha\mu\right). \tag{6.7}$$

We showed in (4.5) that $\eta/N_{\mathrm{inv}} \approx 1/(N_{\mathrm{inv}} + (kT/q^2)(C_{\mathrm{ox}}+C_{\mathrm{d}}))$. Hence, in this section, for a matter of simplicity and consistency with the compact model proposed by Hung et al. (1990), we use that $\eta/N_{\mathrm{inv}} = 1/(N_{\mathrm{inv}} + N^*)$ with $N^* = (kT/q^2)(C_{\mathrm{ox}}+C_{\mathrm{d}})$.

Using our model, the Variance of the LF noise for a uniformly doped device is given by

$$\mathrm{Var}\left[S_{Id}(f)\right]=24\frac{kT}{3\pi^2\gamma f^2}\frac{I_d^4}{W^3L^4}\int_0^L\left(\frac{\eta(x)}{N_{inv}(x)}+\alpha\mu(x)\right)^4 N_{tr}(E_{Fn})dx\ . \tag{6.8}$$

In (Hung, et al., 1990) the following empirical relation is used, $N_{\mathrm{t}}(1 + \alpha\mu_{\mathrm{eff}}N_{\mathrm{inv}}/\eta)^2 \approx \mathbf{A} + \mathbf{B}N_{inv} + \mathbf{C}N_{\mathrm{inv}}^2$. Hence,

$$\left(\eta/N_{inv}+\alpha\mu\right)^2 N_t(E_{Fn})\approx\left(\mathbf{A}+\mathbf{B}N_{inv}+\mathbf{C}N_{inv}^2\right)\Big/\left(N_{inv}+N^*\right)^2 \tag{6.9}$$

where **A**, **B** and **C** are the model parameters. Analyzing (6.9) one can see that the empirical function must account for the trap density as a function of the quasi-Fermi level and also the normalized current

deviation ($\delta\tilde{I}_d = \eta/N_{inv} + \alpha\mu$) as a function of the carrier density. If the trap density is constant, $\mathbf{A} = N_t$, $\mathbf{B} = 2N_t\alpha\mu\eta^{-1}$ and $\mathbf{C} = N_t(\alpha\mu\eta^{-1})^2$. Hence, for a constant trap density $\mathbf{C} = \mathbf{B}^2/(4\mathbf{A})$ and it is a redundant parameter.

Substituting (6.9) in (5.11),

$$S_{Id}(f) = \frac{kT}{\gamma_a f}\frac{I_d^2}{WL^2}\int_0^L \left(\mathbf{A} + \mathbf{B}N_{inv}(x) + \mathbf{C}N_{inv}^2(x)\right) \Big/ \left(N_{inv}(x) + N^*\right)^2 dx \,. \tag{6.10}$$

Using $I_{ds} = WqN_{inv}\mu_{eff}\, dV/dx$ and the carrier density linearization, $dN_{inv}\,(q/aC_{ox} + \Phi_t/N_{inv}) = dV$, we can calculate the noise in all operation regions as

$$S_{Id}(f) = \frac{q^2\mu_{eff}kT}{aC_{ox}\gamma_a f}\frac{I_d}{L^2}\int_{N_L}^{N_0} \left(\mathbf{A} + \mathbf{B}N_{inv} + \mathbf{C}N_{inv}^2\right) \Big/ \left(N_{inv} + N^*\right) dN_{inv} \,, \tag{6.11}$$

where a is the slope factor that accounts the bulk charge effect on the threshold voltage, N_0 and N_L are the carrier density at the source side and drain side respectively. In the original derivation in (Hung, et al., 1990) the carrier linearization is not used and the calculation of the noise is divided in the linear region, saturation and weak inversion. One should note that for the calculation of (6.11) we use $aC_{ox} = C_{ox}+C_d$ hence $(q/aC_{ox} + \Phi_t/N_{inv}) = (q/aC_{ox}N_{inv})(N_{inv} + N^*)$.

The integral in (6.11) is readily evaluated in a closed form given by

$$S_{Id}(f) = \frac{q^2\mu_{eff}kTI_d}{aC_{ox}\gamma_a fL^2}\left[\frac{\mathbf{C}}{2}(N_0^2 - N_L^2) + (\mathbf{B} - \mathbf{C}N^*)(N_0 - N_L) + (\mathbf{A} - \mathbf{B}N^* + \mathbf{C}N^{*2})\ln\left(\frac{N_0 + N^*}{N_L + N^*}\right)\right]. \tag{6.12}$$

It is straightforward to demonstrate that the same transformation used in (6.11) can be applied in the calculation of the Expected value and Variance of our proposed model. Which become

$$\mathrm{E}[S_{Id}(f)] = 2\frac{q^2\mu_{eff}kT}{aC_{ox}\gamma f}\frac{I_d}{L^2}\int_{N_L}^{N_0} N_{tr}\delta\tilde{I}_d^{\,2}(N_{inv} + N^*)dN_{inv} \,, \tag{6.13}$$

$$\mathrm{Var}\left[S_{Id}(f)\right] = 24\frac{q^2\mu_{eff}kT}{aC_{ox}3\pi^2\gamma f^2}\frac{I_d^3}{W^2L^4}\int_{N_L}^{N_0} N_{tr}\delta\tilde{I}_d^{\,4}(N_{inv} + N^*)dN_{inv} \;. \tag{6.14}$$

However, one cannot readily use (6.9) for the calculation of the Variance. First, the trap density term must be separated. For devices with a constant trap density, the Variance can be calculated using the same set of parameters **A**, **B** and **C**. For the Expected value $N_t(1 + \alpha\mu N_{inv}/\eta)^2 \approx \mathbf{A}(1 + (\mathbf{B}/\mathbf{A})N + (\mathbf{C}/\mathbf{A})N^2)$ then for the Variance $N_t(1 + \alpha\mu N_{inv}/\eta)^4 \approx \mathbf{A}(1 + (\mathbf{B}/\mathbf{A})N + (\mathbf{C}/\mathbf{A})N^2)^2$. However, as is shown in Section 5.4 and Section 6.5, to describe the behavior of p-channel devices we need to vary the trap density and for that we need to introduce a new set of parameters. In order that the integrals in (6.13) and (6.14) have a closed form, the traps density can be described as a polynomial,

$$N_{tr}(N_{inv}) = \mathbf{N_{TA}} + \mathbf{N_{TB}} \times N_{inv} + \mathbf{N_{TC}} \times N_{inv}^2 \ \ldots \tag{6.15}$$

Instead of using (6.9), the normalized current deviation can be calculated using one parameter for $\alpha\mu$. Hence,

$$\delta\tilde{I}_d = \left(\frac{1}{N_{inv}+N^*} + \alpha\mu\right) = \left(\frac{1}{N_{inv}+N^*} + \mathbf{N_I}\right). \tag{6.16}$$

Using $N_{tr} = \mathbf{N_{TA}}$ and (6.16) in (6.13), and in (6.14), to calculate the Expected value and Variance respectively, one has that

$$\mathrm{E}[S_{Id}(f)] = 2\frac{q^2\mu_{eff}kT}{aC_{ox}\gamma f}\frac{I_d}{L^2}\mathbf{N_{TA}}\left(\log\frac{N_0+N^*}{N_L+N^*} + 2\mathbf{N_I}(N_0-N_L) + \frac{\mathbf{N_I^2}}{2}(N_0^2-N_L^2) + \mathbf{N_I^2}N^*(N_0-N_L)\right), \tag{6.17}$$

$$Var[S_{Id}(f)] = 24\frac{q^2\mu_{eff}kT}{3\pi^2 aC_{ox}\gamma f}\frac{I_d^3}{W^2L^4}\mathbf{N_{TA}}\left(6\mathbf{N_I^2}\log\frac{N_0+N^*}{N_L+N^*} + 4\mathbf{N_I^3}(N_0-N_L) + \frac{\mathbf{N_I^4}}{2}(N_0^2-N_L^2) + \mathbf{N_I^4}N^*(N_0-N_L)\right.$$
$$\left. + 2(N_L+N^*)^{-2} - 2(N_0+N^*)^{-2} + \frac{4\mathbf{N_I}}{(N_L+N^*)} - \frac{4\mathbf{N_I}}{(N_0+N^*)}\right). \tag{6.18}$$

Therefore, using only a set of two parameters we can describe in a compact form all the noise statistics (E, Var, K ...) of a uniformly doped device with a uniformly distributed trap density in energy.

Figures 7.1 and 7.2 show, respectively, the behavior of the LF noise Expected value and K of uniformly doped devices with an ideal long channel (channel doping Na =6e17 and oxide thickness T_{ox} = 3 nm and $V_{fb} = -0.8$V). The figures show a comparison between the original calculation of the model ((5.10) and (6.11)) and the compact form in (6.17) and (6.18), for $N_{tr}/\gamma = \mathbf{N_{TA}} = 1\times10^9$ cm^{-2}eV^{-1} and $\alpha\mu_{eff} = \mathbf{N_I} = 1\times10^{-13}$ cm^2.

Figure 7.1 – Expected value of long channel and uniformly doped devices, calculated using the full model in (5.10) (solid lines) and the compact model in (6.17) (dashed lines).

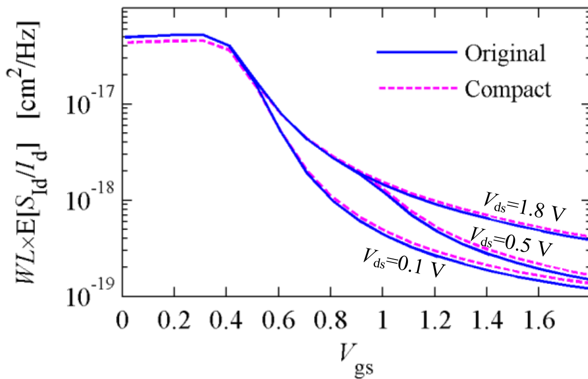

Figure 7.2 – K value of long channel and uniformly doped devices calculated using the full model in (6.11) (solid lines) and the compact model in (6.18) (dashed lines).

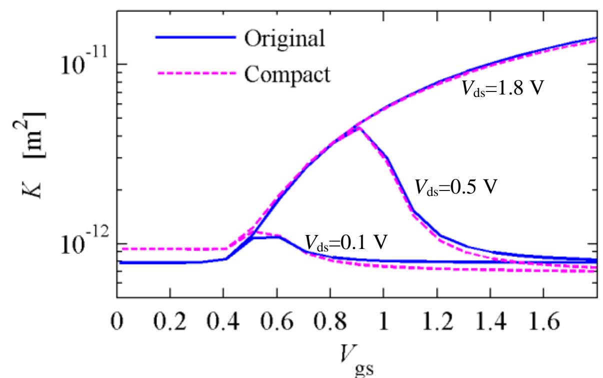

As we have shown in Section 6.5 the halo implants of the p-channel devices in 140-nm technology does not cause a large impact on the statistics of the LF noise. Therefore, we use the N_0

and N_L extracted from the TCAD simulations, in Section 6.5, to calculate the Expected value and K using the compact form of the uniformly doped channel model. In Figures 7.3 and 7.4 we compare the calculated values using the compact form with the measured data. The trap density of the p-channel devices in 140-nm technology is a function of the Fermi-level hence in the derivation of the compact form we use that $N_{tr} = \mathbf{N_{TA}} + \mathbf{N_{TB}} \times N_{inv}$.

The compact form is calculated using N_0 and N_L extracted from the TCAD simulator, although in modern compact models such as BSIM6 (Chauhan, et al., 2013) and PSP (Aarts, et al., 2008) N_0 and N_L can also be extracted taking into account short channel effects and velocity saturation. N_0 and N_L are extracted, from the TCAD, a few nanometers away from the source and drain. Hence the depletion region of the source and drain does not impact the extraction of N_0 and N_L.

The full compact form using $\mathbf{N_{TA}}$ and $\mathbf{N_{TB}}$ is shown in (6.19) and (6.20). A good fitting was possible using $\mathbf{N_{TA}} = 4.6\times10^{8}$ cm^{-2}eV^{-1}, $\mathbf{N_{TB}} = 2.8\times10^{-3}$ eV^{-1} and $\mathbf{N_I} = 0.8\times10^{-13}$ cm^2.

Figure 7.3 – Expected value of 8×1µm² p-channel devices in 140-nm technology. Comparison between measured data (solid symbols) and calculated using the compact model (dashed lines).

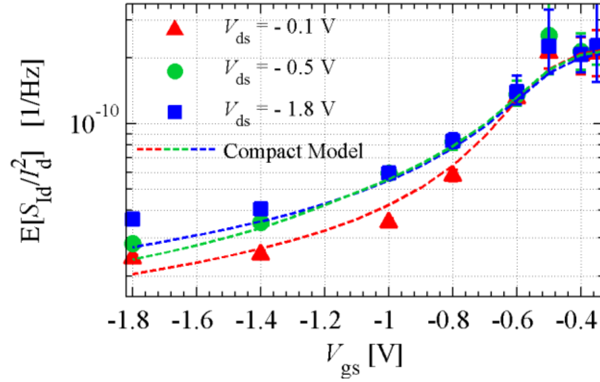

Figure 7.4 – K value of 8×1µm² p-channel devices in 140-nm technology. Comparison between measured data (solid symbols) and calculated using the compact model (dashed lines).

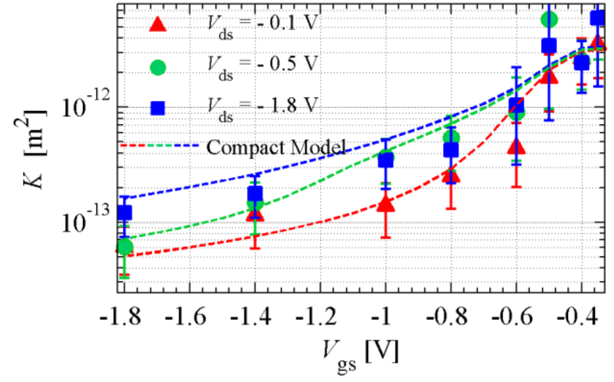

Full compact form using $\mathbf{N_{TA}}$ and $\mathbf{N_{TB}}$

$$\mathrm{E}[S_{Id}(f)] = 2\frac{q^2\mu_{eff}kT}{aC_{ox}\gamma f}\frac{I_d}{L^2}\left[\mathbf{N_{TA}}\left(\ln\frac{N_0+N^*}{N_L+N^*} + 2\mathbf{N_I}(N_0-N_L) + \frac{\mathbf{N_I^2}}{2}(N_0^2-N_L^2) + \mathbf{N_I^2}N^*(N_0-N_L)\right)\right.$$
$$\left. +\mathbf{N_{TB}}\left(N^*\ln\frac{N_L+N^*}{N_0+N^*} + (N_0-N_L) + \mathbf{N_I}(N_0^2-N_L^2) + \frac{\mathbf{N_I^2}N^*}{2}(N_0^2-N_L^2) + \frac{\mathbf{N_I^2}}{3}(N_0^3-N_L^3)\right)\right] \tag{6.19}$$

$$\mathrm{Var}[S_{Id}(f)] = 24\frac{q^2\mu_{eff}kT}{3\pi^2 aC_{ox}\gamma f}\frac{I_d^3}{W^2L^4}\left[\mathbf{N_{TA}}\left(6\mathbf{N_I^2}\ln\frac{N_0+N^*}{N_L+N^*}+4\mathbf{N_I^3}(N_0-N_L)+\frac{\mathbf{N_I^4}}{2}(N_0^2-N_L^2)+\mathbf{N_I^4}N^*(N_0-N_L)\right.\right.$$
$$\left.+2(N_L+N^*)^{-2}-2(N_0+N^*)^{-2}+\frac{4\mathbf{N_I}}{(N_L+N^*)}-\frac{4\mathbf{N_I}}{(N_0+N^*)}\right)+\mathbf{N_{TB}}\left(2\mathbf{N_I^2}N^*\ln\frac{N_L+N^*}{N_0+N^*}+6\mathbf{N_I^2}(N_0-N_L)\right.$$
$$+\frac{4\mathbf{N_I^3}}{2}(N_0^2-N_L^2)+\frac{\mathbf{N_I^4}N^*}{2}(N_0^2-N_L^2)+\frac{\mathbf{N_I^4}}{3}(N_0^3-N_L^3)+\frac{N_0^2(2N_L+N^*)-N_L^2(2N_0+N^*)}{2(N_0+N^*)^2(N_L+N^*)^2}+ \tag{6.20}$$
$$\left.\left.4\mathbf{N_I}\left(\ln\frac{N_0+N^*}{N_L+N^*}+\frac{N^*}{(N_0+N^*)}-\frac{N^*}{(N_L+N^*)}\right)\right)\right]$$

7.2 Halo-implanted Devices

For devices with lateral doping gradient the current deviation caused by a trap at position x_t along the channel is given by (4.38), repeated below.

$$\Delta I_d(x_t) = \frac{I_d}{W}\left(\frac{f(x_t)}{\int_0^L f(x)dx}\right)\left(\frac{\eta(x_t)}{N_{inv}(x_t)}+\alpha\mu(x_t)\right) \tag{7.1}$$

where, $f(x)=\exp\left[-\int_0^x \frac{1}{g}\frac{\partial g}{\partial x}dx\right]$, $g(x,V(x))=\mu(x,V(x))Q(x,V(x))$ is the channel conductance and the first parenthesis of the equation accounts for the lateral doping gradient.

In modern MOSFETs, the lateral doping gradient is introduced by the halo or pocket implants at the drain and source side of the transistor, as shown in Figure 7.5. In the figure, L_h is the extension of the halo-implanted region and L_{eff} is the effective channel length.

Figure 7.5 – Example of the lateral doping gradient introduced by the halo implants.

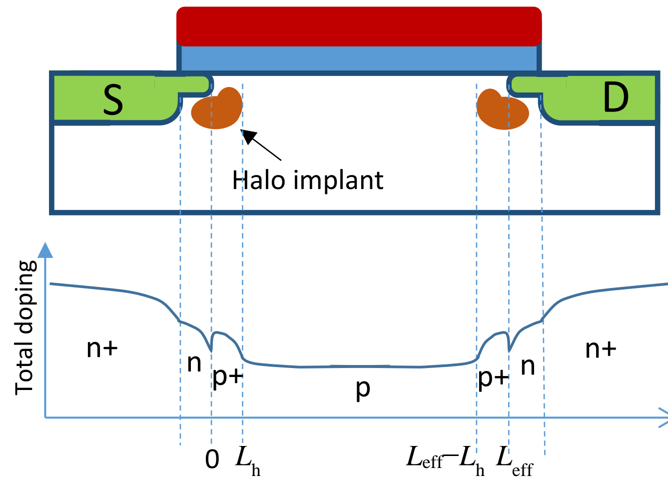

In the form of (7.1) the current deviation of halo-implanted devices is very difficult to be analytically analyzed. Therefore, in this section, we propose some simplifications that allow us to quickly analyze the impact of halo-implanted regions in the statistics of the LF noise.

In Figure 7.6, the long channel transistor (where $L_{eff} > 2L_h$) is simplified by 3 different uniformly doped regions. Hence, the halo-implanted regions is described by an effective doping ($N_{ah,eff}$) and an effective length ($L_{h,eff}$), and the channel region without halo-implants (we'll call it channel region) is also described by an effective doping ($N_{ach,eff}$) and an effective length ($L_{eff} - 2L_{h,eff}$). Using these simplifications, the surface potential along the channel is given by three different regions with step transitions among them, as shown in Figure 7.6. The figure also shows the channel potential for this simplification, where V_1 and V_2 are the potentials at halo-channel transitions. In the following nomenclature, we use the index 1 to refer to the source-side halo region and 2 to refer to the drain-side halo region. In this simplification, we also consider that the mobility is the same for all regions.

Figure 7.6 – Simplification of the halo-implanted device in three different uniform regions.

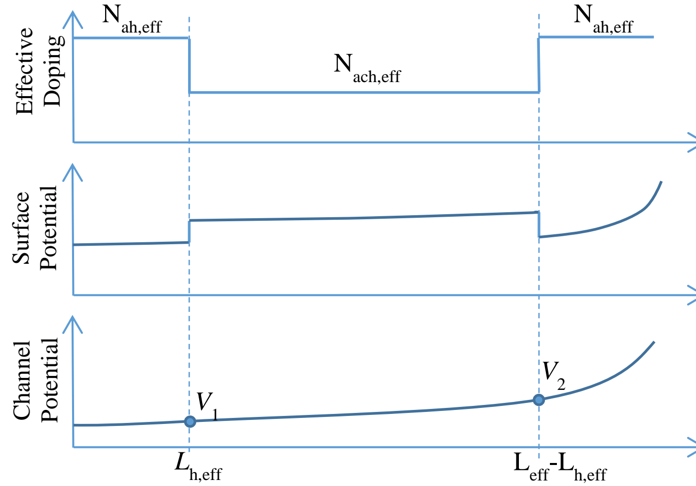

Using the simplifications described above, $f(x)$ can be simplified from weak to strong inversion regions as

$$f(x) = \begin{cases} 1, & \text{for } x < L_h \\ \dfrac{N_{h1}(V_1)}{N_{ch}(V_1)}, & \text{for } L_h < x < L - L_h \\ \dfrac{N_{h1}(V_1)}{N_{ch}(V_1)} \dfrac{N_{ch}(V_2)}{N_{h2}(V_2)}, & \text{for } L - L_h < x < L \end{cases} \tag{7.2}$$

where $N_{h1}(V)$ and $N_{h2}(V)$ are, respectively, the carrier density at the source and drain side halo as a function of the channel potential, and $N_{ch}(V)$ is the carriers density at the channel region as a function of the channel potential. The problem is now simplified in finding V_1 and V_2 potentials and then

calculate N_{h1}, N_{h2} and N_{ch} at these potentials. To simplify the nomenclature, in the following equations we use L and L_h instead of L_{eff} and $L_{h,eff}$, hence one should remember that in this section L and L_h are actually effective lengths.

Using the proposed simplification, the calculation of the Expected value of the noise can be also separated in 3 different regions and it is given by:

$$E\left[S_{Id}(f)\right]=2\frac{kT}{\gamma f}\frac{I_d^2}{W}\frac{1}{l^2}\left(\begin{array}{l}1\int_0^{L_h}\left(\frac{\eta}{N_{h1}}+\alpha\mu\right)^2 N_{tr}dx+A^2\int_{L_h}^{L-L_h}\left(\frac{\eta}{N_{ch}}+\alpha\mu\right)^2 N_{tr}dx\\+B^2\int_{L-L_h}^{L}\left(\frac{\eta}{N_{h2}}+\alpha\mu\right)^2 N_{tr}dx\end{array}\right), \tag{7.3}$$

where $l=1L_h+A(L-2L_h)+BL_h$, $A=\frac{N_{h1}(V_1)}{N_{ch}(V_1)}$ and $B=\frac{N_{h1}(V_1)}{N_{ch}(V_1)}\frac{N_{ch}(V_2)}{N_{h2}(V_2)}$,

And the Variance,

$$\mathrm{Var}\left[S_{Id}(f)\right]=24\frac{kT}{3\pi^2\gamma f^2}\frac{I_d^4}{W^3l^4}\left(\begin{array}{l}1\int_0^{L_h}\left(\frac{\eta}{N_{h1}}+\alpha\mu\right)^4 N_{tr}dx+A^4\int_{L_h}^{L-L_h}\left(\frac{\eta}{N_{ch}}+\alpha\mu\right)^4 N_{tr}dx\\+B^4\int_{L-L_h}^{L}\left(\frac{\eta}{N_{h2}}+\alpha\mu\right)^4 N_{tr}dx\end{array}\right) \tag{7.4}$$

By now, one can realized that the simplification in Figure 7.6 allows that the halo-implanted transistor be described by three transistors in series. In Section 7.3 we show the derivation of (7.3) and (7.4) using a three transistor model. Although, in this section we continue to analyze the model in the form of (4.38) and (7.2).

In order to find an analytical expression for (7.3) and (7.4), we need to find and analytical expression for A and B. The dependencies with V_1 and V_2 turn this task very challenging. However, as is shown in Chapter 6, the halo-implanted regions influence is higher in weak inversion. This allows us to construct some simplifications to analyze the halo-implanted regions impact in the LF noise statistics.

In weak inversion, the carrier density is approximated as

$$N_{inv}(x)\approx\frac{1}{q}(n-1)C_{ox}\phi_t e^{\frac{V_{gb}-V_T}{n\phi_t}-\frac{V_{cb}(x)}{\phi_t}}, \tag{7.5}$$

where n is the slope factor. Using (7.5) it becomes clear that in weak inversion A and B become independent of the channel potential (V_1 and V_2). A in weak inversion is given by

$$A_{wi} = \frac{(n_h - 1)}{(n_{ch} - 1)} \exp\left(\frac{V_{gb} - V_{T,h1}}{n_h kT / q} - \frac{V_{gb} - V_{T,ch}}{n_{ch} kT / q} \right), \tag{7.6}$$

where n_h, n_{ch} $V_{T,h}$, $V_{T,ch}$ are the slope factor of the halo and channel region, and the threshold voltage of the halo and channel regions respectively. To easy understand the behavior of the halo-implanted region in weak inversion, we rough approximate $n_h \approx n_{ch} = 1 + C_d/C_{ox}$. Hence,

$$A_{wi} = \exp\left(\frac{V_{T,ch} - V_{T,h1}}{n_h \, kT / q} \right) \tag{7.7}$$

and

$$B_{wi} = A_{wi} \exp\left(\frac{V_{T,h2} - V_{T,ch}}{n_h \, kT / q} \right). \tag{7.8}$$

Hence, the amplification of the current deviation at the halo-implanted region is given by the exponential of the difference between the threshold voltage from the halo region and channel region, and also by the exponential of the temperature.

If the threshold voltage of the source-side halo is equal to the threshold voltage of the drain-side halo ($V_{T,h1} = V_{T,h2}$), an approximated condition where there is no barrier lowering on the drain-side halo induced by V_{ds}, one has that $B_{wi} = 1$. Using this condition, equation (7.3) and the fact that in weak inversion $\eta/N_{inv} + \alpha\mu \approx q^2/(kT(C_{ox}+C_d))$ (see Section 4.5) one finally has that the Expected value of the LFN in weak inversion is approximated as

$$\mathrm{E}\left[S_{Id}(f)\right]_{wi} = 2kT \frac{N_{tr}(E_F)}{\gamma} \frac{I_d^2}{fW} \frac{\left(2L_h + A_{wi}^2 (L - 2L_h)\right)}{\left(2L_h + A_{wi} (L - 2L_h)\right)^2} \left(\frac{q^2}{kT(C_{ox} + C_d)} \right)^2, \tag{7.9}$$

and using the same condition in (7.4), one can calculate K in weak inversion as

$$K_{wi} = \frac{6}{3\pi^2 kT} \frac{\gamma}{N_{tr}(E_F)} \frac{L\left(2L_h + A_{wi}^4 (L - 2L_h)\right)}{\left(2L_h + A_{wi}^2 (L - 2L_h)\right)^2}. \tag{7.10}$$

Therefore, in weak inversion, K becomes dependent on the channel length and (7.10) gives an analytical expression to analyze this dependency.

Figures 7.7 – 7.10 show the Expected value normalized by the device area and K, calculated using (7.9) and (7.10) respectively, and compare with the measured data for three different channel lengths. Figures 7.7 and 7.8 show the comparison for n-channel devices in 40-nm technology and Figures 7.9 and 7.10 show the comparison for n-channel devices in 140-nm technology. The 40-nm devices fit was done using $V_{T,h} = 0.43$ V, $V_{T,ch} = 0.3$ V, $C_d = 0.45C_{ox}$, $T_{ox} = 2.1$ nm. $N_{tr} = 1.7\times10^9$

cm^{-2}eV^{-1} and L_h= 80 nm. The 140-nm devices fit was done using $V_{T,h}$ = 0.54 V, $V_{T,ch}$ = 0.45 V, C_d = 0.3C$_{ox}$, T_{ox} = 2.9 nm, N_{tr}= 1.1×10^9 cm^{-2}eV^{-1} and L_h = 50 nm.

Figure 7.7 – Weak inversion approximation for the Expected value of n-channel 40-nm devices. V_{ds} = 50 mV.

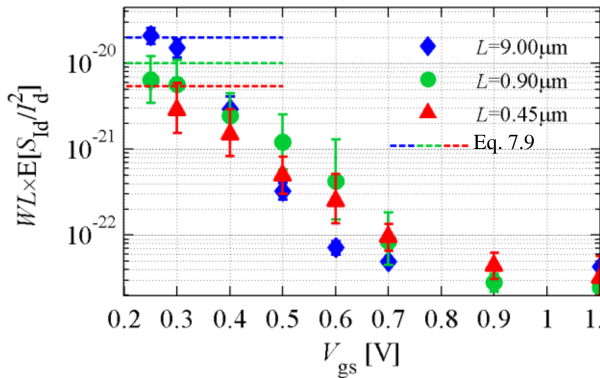

Figure 7.8 – Weak inversion approximation for K value of n-channel 40-nm devices. V_{ds} = 50 mV.

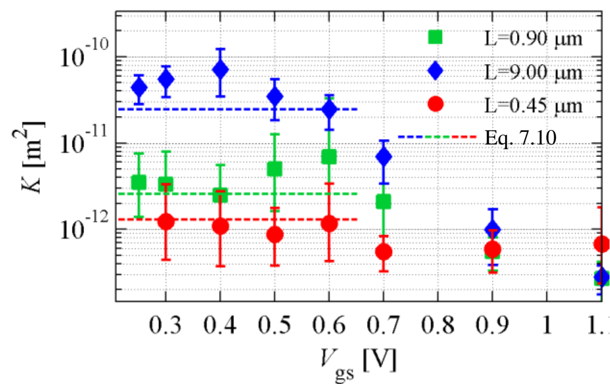

Figure 7.9 – Weak inversion approximation for the Expected value of n-channel 140-nm devices. V_{ds} = 0.1 V.

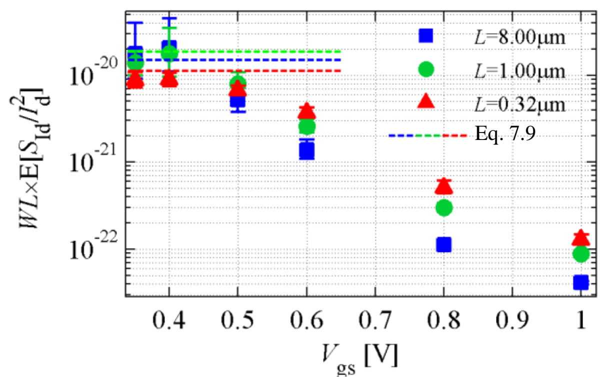

Figure 7.10 – Weak inversion approximation for K value of n-channel 140-nm devices. V_{ds} = 0.1 V.

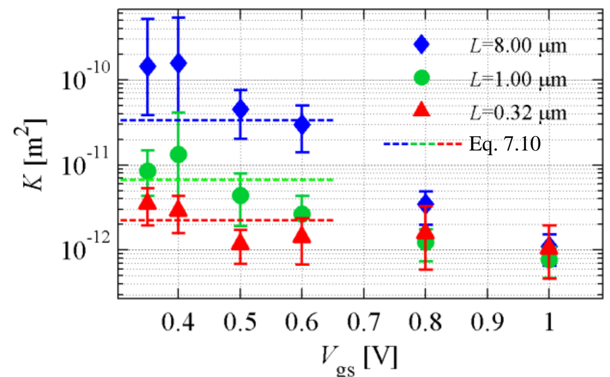

Figure 7.11 show how in practice the σ[ln(S_{Id})] as a function of the channel length is calculated using the K calculated from (7.10), for n-channel devices in 140-nm technology with V_{gs}=0.5 V and V_{ds} = 0.1V. The figure shows a good fitting with the measured data, when using the same parameters as used in Figures 7.9 and 7.10.

Figure 7.11 – Comparison between the measured (solid symbols) and calculated (dashed lines) Standard Deviation of the logarithm of the LFN for different channel lengths. $V_{gs} = 0.5$ V and $V_{ds} = 0.1$V.

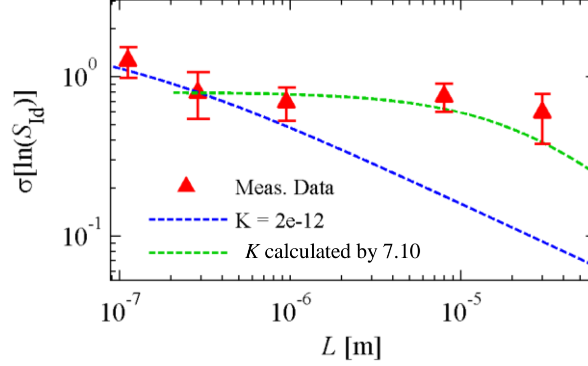

Figure 7.12 shows a comparison between the current deviation extracted from the TCAD simulation (same as in Section 6.4) and the current deviation calculated using (7.1) with the simplification in (7.2), for 1-μm long devices in 140-nm technology. For the calculation, the same parameters used in the fittings of Figures 7.9 and 7.10 were used ($V_{T,h} = 0.54$ V, $V_{T,ch} = 0.45$ V, $C_d = 0.3C_{ox}$, $T_{ox} = 2.9$ nm, $N_{tr}/\gamma=1.1\times10^9$ cm^{-2}eV^{-1}). Moreover, Figure 7.13 shows the effect of the barrier lowering at the drain-side halo when V_{ds} is high. This effect decreases the threshold voltage of the drain-side halo, which makes $B_{wi} \neq 1$. For the fitting in Figure 7.13 B_{wi} is calculated using $V_{T,h2} = 0.49$ V.

Figure 7.12 – Weak inversion approximation of the current deviation for 1-μm long devices in 140-nm technology with $V_{gs} = 0.4$ V and $V_{ds} = 0.1$ V.

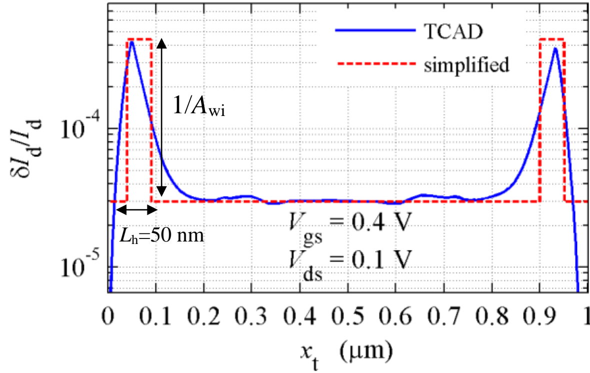

Figure 7.13 – Weak inversion approximation of the current deviation for 1-μm long devices in 140-nm technology with V_{gs}=0.4V and V_{ds}=1.8V.

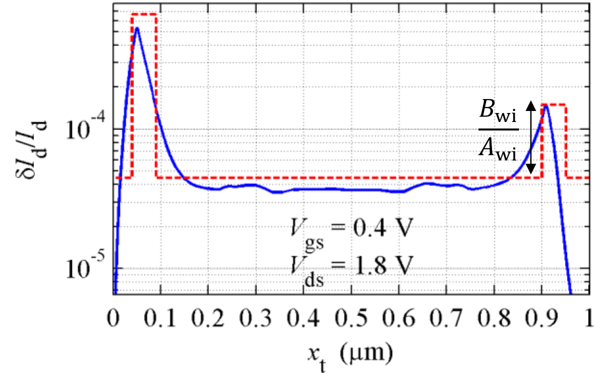

In strong inversion the carrier density can be approximated as

$$qN_{inv}(x) \approx C_{ox}(V_{gb} - V_T - nV_{cb}(x)). \qquad (7.11)$$

Using (7.11) it become clear that in strong inversion A and B become dependent of the channel potential ($V_{cb}=V_1$ and $V_{cb}=V_2$) and A and B is given by:

$$A_{si} = \frac{(V_{gb} - V_{T,h} - n_h V_1)}{(V_{gb} - V_{T,ch} - n_{ch} V_1)} \qquad (7.12)$$

and

$$B_{si} = A_{si} \frac{(V_{gb} - V_{T,ch} - n_{ch}V_2)}{(V_{gb} - V_{T,h2} - n_{h2}V_2)} \quad . \tag{7.13}$$

Figure 7.14 shows a comparison between the A calculated using a 1D Poisson solver and using the weak inversion simplifications in (7.6) and (7.7), and the strong inversion simplification in (7.12).

Figure 7.14 – A calculated using the proposed simplifications and calculated solving the 1D Poisson equation with $V_{fb} = -0.82$ V, $N_{a,ch} = 4.5\times10^{17}$ cm^{-2}, $N_{a,h} = 8\times10^{17}$ cm^{-2} and $Tox = 3$ nm.

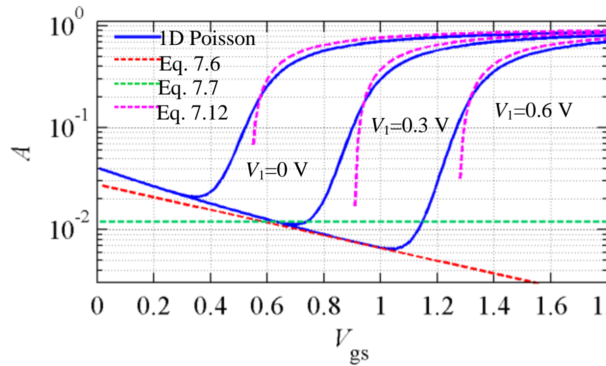

Using the proposed simplifications in (7.2), the problem in finding a compact model of (7.3) and (7.4) is reduced in applying the methodology used in Section 7.1 to the three different integrals of (7.3) and (7.4), and finding an analytical expression for A and B that works from strong to weak inversion. In the next Section, we show that the LF noise statistics of the halo implanted device can be simulated in compact simulators using three uniform doped transistors in series, where the noise statistics of each individual transistor can be calculated using the compact form in Section 7.1.

7.3 The Three Transistors Model

Using the simplifications of the previous section, the halo-implanted transistor can be described as three transistors in series (M_{h1}, M_{ch} and M_{h2}) as shown in Figure 7.15.

Figure 7.15 – Schematic of the three transistors model.

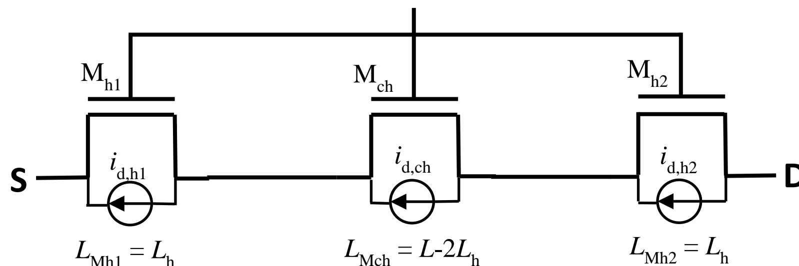

In the schematic of Figure 7.15 the noise of each individual transistor is added to the current at the terminals S and D, and the Expected value of the total LF noise in the I_d current can be calculated as a sum of the Expected value of each transistor noise given by

$$\mathrm{E}[S_{Id}] = \left(\frac{g_{s,ch}}{g_{s,ch} + g_{d,h1} + g_{d,h1}\dfrac{g_{d,ch}}{g_{s,h2}}} \right)^2 \mathrm{E}[S_{Id,h1}] + \left(\frac{1}{1 + \dfrac{g_{s,ch}}{g_{d,h1}} + \dfrac{g_{d,ch}}{g_{s,h2}}} \right)^2 \mathrm{E}[S_{Id,ch}] + \left(\frac{g_{d,ch} / g_{s,h2}}{1 + \dfrac{g_{s,ch}}{g_{d,h1}} + \dfrac{g_{d,ch}}{g_{s,h2}}} \right)^2 \mathrm{E}[S_{Id,h2}]$$

(7.14)

where $g_{s,ch}$ and $g_{s,h2}$ are the source transconductance of the M_{ch} and M_{h2} transistors respectively; $g_{d,ch}$ and $g_{d,h1}$ are the drain transconductance of the M_{ch} and M_{h1} transistors respectively. The transconductances are calculated by

$$\begin{aligned} g_{s,ch} &= -q\mu \frac{W}{L-2L_h} N_{inv,Sch} \qquad & g_{d,ch} &= -q\mu \frac{W}{L-2L_h} N_{inv,Dch} \\ g_{d,h1} &= -q\mu \frac{W}{L_h} N_{inv,Dh1} \qquad & g_{d,ch} &= -q\mu \frac{W}{L_h} N_{inv,Sh2} \end{aligned} \tag{7.15}$$

where $N_{inv,Sch}$ and $N_{inv,Dch}$ are, respectively, the inversion carrier density at the source and drain side of the transistor M_{ch}; $N_{inv,Dh1}$ and $N_{inv,Sh2}$ are the inversion carrier density at the drain of the transistor M_{h1} and at the source of transistor M_{h2}, respectively.

Using some algebra one can show that (7.15) and (7.3) are the same and can be rewritten as

$$\mathrm{E}[S_{Id}] = \frac{L_h^2\,\mathrm{E}[S_{Id,h1}] + (L-2L_h)^2 A^2\,\mathrm{E}[S_{Id,ch}] + B^2 L_h^2\,\mathrm{E}[S_{Id,h2}]}{(L_h + A(L-2L_h) + BL_h)^2}\,. \tag{7.16}$$

Therefore, the Expected value of the noise introduced by the transistors representing the halo regions is

$$\mathrm{E}[S_{Id}]_{halo} = \frac{L_h^2\,\mathrm{E}[S_{Id,h1}] + B^2 L_h^2\,\mathrm{E}[S_{Id,h2}]}{(L_h + A(L-2L_h) + BL_h)^2}\,, \tag{7.17}$$

and the Expected value of the noise introduced by the transistor representing the region without halo implants is

$$\mathrm{E}[S_{Id}]_{channel} = \frac{L(L-2L_h)^2 A^2\,\mathrm{E}[S_{Id,ch}]}{(L_h + A(L-2L_h) + BL_h)^2}\,. \tag{7.18}$$

The Variance can also be calculated using the methodology above. Therefore,

$$\mathrm{Var}[S_{Id}] = \frac{L_h^4\,\mathrm{Var}[S_{Id,h1}] + (L-2L_h)^4 A^4\,\mathrm{Var}[S_{Id,ch}] + B^4 L_h^4\,\mathrm{Var}[S_{Id,h2}]}{(L_h + A(L-2L_h) + BL_h)^4}\,. \tag{7.19}$$

Hence, the Variance of the noise introduced by the halo region and channel region are, respectively,

$$\mathrm{Var}[S_{Id}]_{halo} = \frac{L_h^4\,\mathrm{Var}[S_{Id,h1}] + B^4 L_h^4\,\mathrm{Var}[S_{Id,h2}]}{(L_h + A(L-2L_h) + BL_h)^4}, \tag{7.20}$$

$$\mathrm{Var}[S_{Id}]_{channel} = \frac{L(L-2L_h)^4 A^4\,\mathrm{Var}[S_{Id,ch}]}{(L_h + A(L-2L_h) + BL_h)^4}. \tag{7.21}$$

Using the transistors transconductances, A and B can be calculated as

$$A = \frac{g_{d,h1}}{g_{s,ch}} \frac{L_h}{(L-2L_h)} \tag{7.22}$$

and

$$B = A \frac{g_{d,ch}}{g_{s,h2}} \frac{(L-2L_h)}{L_h}. \tag{7.23}$$

Using the method proposed above, the noise statistics of halo-implanted devices can be implemented in compact simulators. To that end, the calculation of the statistics of each equivalent transistor must be done by implementing the compact calculation of the uniformly doped transistor, described in Section 7.1, and by implementing (7.16), (7.19), (7.22) and (7.23). The drawback of this method is that each transistor is now modeled as three transistors and the equivalent halo-region and channel-region transistors must be fully modeled, not only to give good IV and CV curves of the complete transistor but also to properly characterize the noise effect.

8 DISCUSSIONS ON THE LFN DISTRIBUTION

In the previous chapters, we have shown that the proposed model can predict the noise statistics. On this chapter, we take a more detailed look in the LF noise distribution and analyze if the assumptions used to derive the model combined with Monte Carlo (MC) simulations can also predict the LFN distribution shape.

8.1 Large area devices

In Section 3.2, we have shown that the RTN (or LFN) distribution can be well approximated by a lognormal distribution. However, in weak inversion and in saturation conditions it is expected that the behavior of current deviation as a function of the trap position in the channel (shown in Figures 6.16 and 6.17), with high impacts at small regions of the channel, can cause some deviations in the distribution of the noise. Although the distribution can still be roughly simplified as a lognormal, as depicted in Figures 8.1 and 8.2, where the Q-Q plot is shown for 10×10 μm^2 devices in 65-nm GO1 technology with V_{gs} = 1.2 V and V_{gs} = 0.4 V respectively. In the Q-Q plot of the logarithm of the noise, the straight line fit shows that the distribution is lognormal and the derivative of this line is given by the standard deviation of the logarithm of the noise (σ[ln(S_{Id})]).

In Chapter 6 we showed that using our proposed model to calculated K and then applying it in a lognormal distribution to calculate σ[ln(S_{Id})] gives a good prediction of the measured σ[ln(S_{Id})]. However, as shown in Figure 8.2 the lognormal simplification (dashed line), in some cases, can underestimate the probability of high LFN values.

Figure 8.1 – Q-Q plot of ln(S_{Id}) for 10×10 μm^2 devices in 65-nm GO1 technology with V_{gs} = 1.2 V. Dashed lines represent the lognormal fit, symbols represent the measured data.

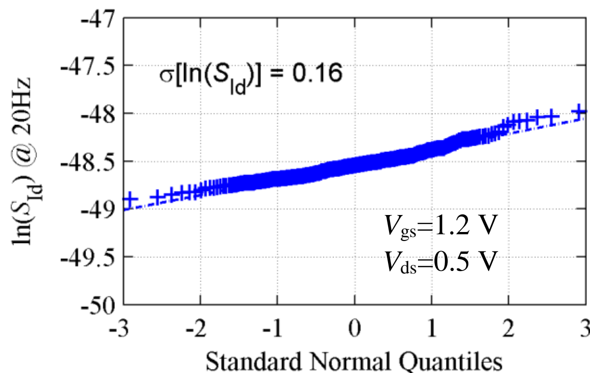

Figure 8.2 – Q-Q plot of ln(S_{Id}) for 10×10 μm^2 devices in 65-nm GO1 technology with V_{gs} = 0.4 V. Dashed lines represent the lognormal fit, symbols represent the measured data.

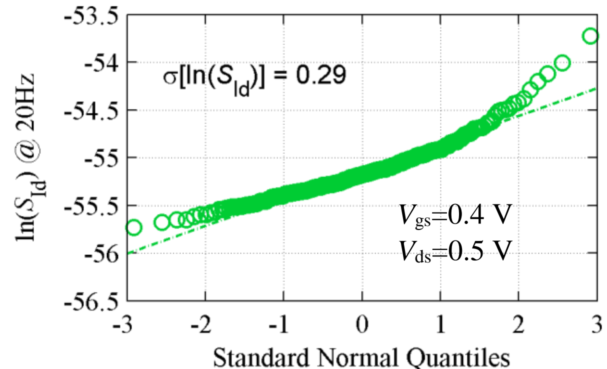

In Figure 8.3 we normalized the measured data to make the left tail of the two distribution (in Figures 8.1 and 8.2) to have the same values. Using this technique, the figure shows the distortion of the original lognormal distribution, this distortion is given by the high impacts at the halo-implanted regions, which introduce high S_{Id} values in the right tail of the distribution.

Figure 8.4 shows that the distribution can be described by the sum of two independent lognormal distributions. In the simplifications used in Sections 7.2 and 7.3, we separated the device channel in three different regions, two regions representing the halo implants and the other region representing the channel without halo implants. From this simplification, one can infer that the final distribution is given by the sum of the lognormal distribution representing the halo regions and the lognormal distribution representing the channel without halo implants.

Figure 8.3 – Q-Q plot of the normalized $\ln(S_{Id})$. The normalization is done to coincide the left tails of both distributions.

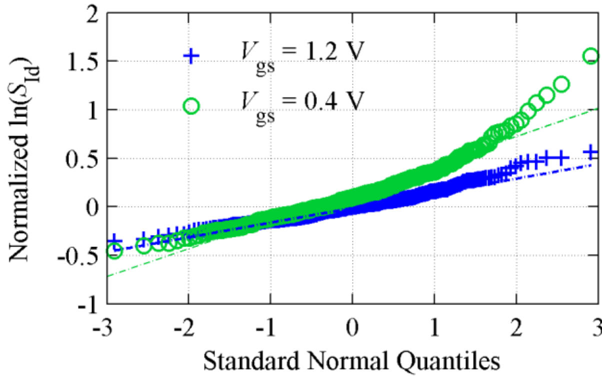

Figure 8.4 – Distribution made by summing two independents lognormal distributions with $\sigma_1 = 0.16$, $\mu_1 = -55.35$, $\sigma_2 = 1.1$ and $\mu_2 = -57.35$.

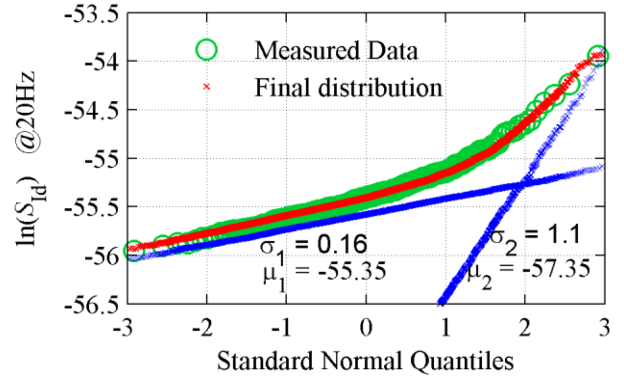

Since, in weak inversion, the current deviation can be separated in three uniform regions, as is shown in Figure 7.12, the *K* value of the lognormal distribution of each region will only depend on the trap density of each region. Considering the trap density the same for all the regions, the standard deviation ($\sigma[\ln(S_{Id})]$) of the lognormal distribution introduced by each region is determined by the length of the region.

Considering the area of the channel region without halo implants to be approximated by $W\times L = 10\times10\ \mu m^2$, we can use the value of $\sigma_1 = 0.16$ to extract the trap density $N_{tr}/\gamma = 0.5\times10^9\ cm^{-2}eV^{-1}$, using (5.6) and (5.17). Using $\sigma_2 = 1.1$, equation (5.17) and that the trap density is the same in the halo-implanted region, we can extract the area of the halo-implanted region as $W\times L = 10\times0.86\ \mu m^2$. Hence, we can extract that each halo has an effective length of approximately 43 nm.

Using (3.3) and (7.9) one has that

$$\frac{E[S_{Id}]_{channel}}{E[S_{Id}]_{halo}} = \frac{e^{\mu_1+0.5\sigma_1^2}}{e^{\mu_2+0.5\sigma_2^2}} \approx \frac{A_{wi}^2(L-2L_H)}{2L_H}\ . \tag{7.24}$$

Therefore, using (7.24), we can extract that $A_{wi} = 0.17$.

To test the extracted quantities, above, we use the Monte Carlo simulation described in Section 3.6. For this Monte Carlo simulation, we assume the average trap impact as a function of its position along the channel ($\delta I_d(x_t)$) as given by Figure 8.5, and the traps are uniformly distributed from source to drain. As in Section 3.6, the trap impacts (ΔI_d) are exponentially distributed. Differently from Section 3.6, the energy of the traps are uniformly distributed, $N_{tr}/\gamma = 0.5\times10^9$ cm^{-2}eV^{-1} at any energy. In Figure 8.6, we compare the distribution of the Measured Data and the distribution of the Monte Carlo simulation of 400 devices. The figure shows that the Monte Carlo simulation (with the same assumptions used in the derivation of the proposed model) fits well the measured distribution.

Moreover, using a constant current deviation along the channel, depicted in Figure 8.7, the Monte Carlo simulation can also fit well the distribution of the LF noise when V_{gs} = 1.2 V and V_{ds} = 0.5 V, shown in Figure 8.8. Figure 8.8 also shows that, using a constant current deviation along the channel, the Monte Carlo simulation results in a distribution that closely resembles a lognormal distribution. Some small deviation in the right tail of the measured distribution is expected since at V_{ds} = 0.5 V the channel is not completely uniform as simplified in Figure 8.7.

Figure 8.5. – Current deviation as a function of the trap position used in the Monte Carlo simulation, for V_{gs}=0.4 V.

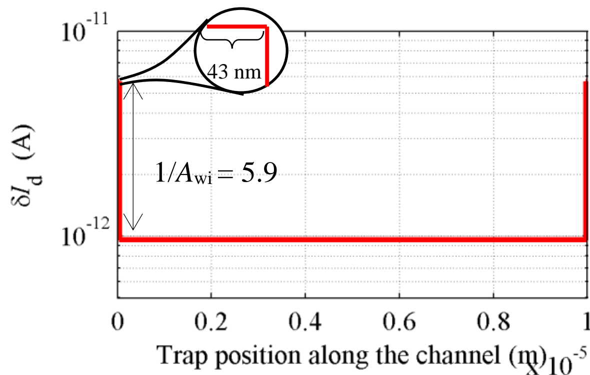

Figure 8.6 – Comparison of the measured data distribution and the generated distribution using Monte Carlo simulations for, 10×10 μm^2 devices with V_{gs} = 0.4V.

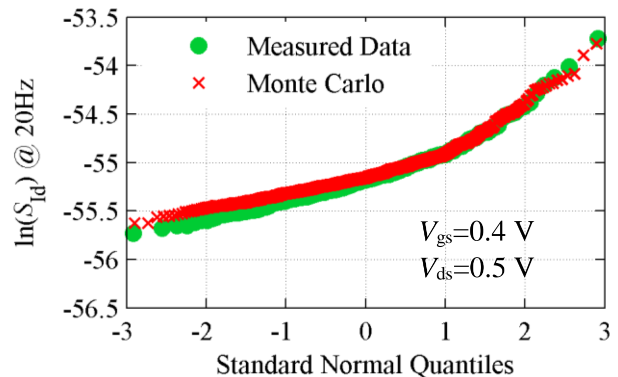

Figure 8.7 – Current deviation as a function of the trap position used in the Monte Carlo simulation, for $V_{gs} = 1.2$ V.

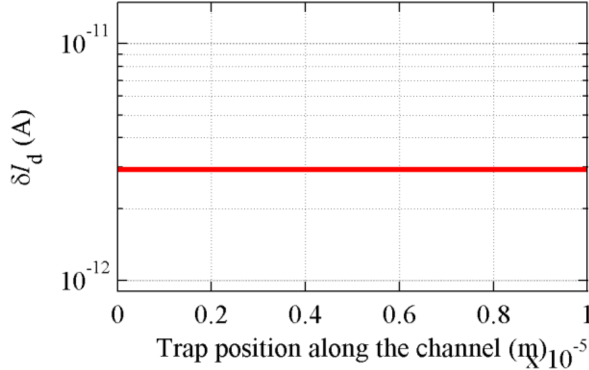

Figure 8.8 – Comparison of the measured data distribution and the generated distribution using Monte Carlo simulations, for 10×10 µm² devices with $V_{gs} = 0.4$V.

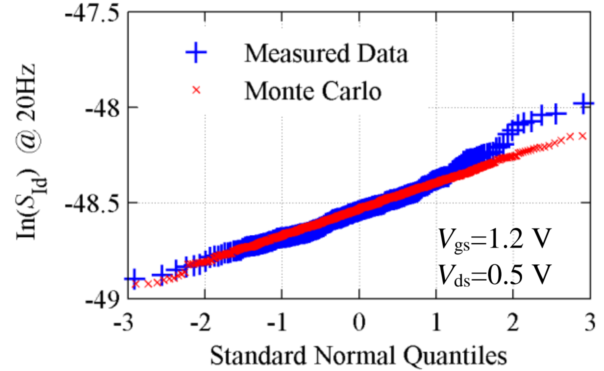

In Figures 8.9 – 8.14, the $\delta I_d(x_t)$ extracted from the TCAD simulation for the 140-nm technology, described in Chapter 6, is used in Monte Carlo simulations. Then, we compare the resultant Monte Carlo distribution with the distribution of the measured LFN. In these Monte Carlo simulations we use $N_{tr}/\gamma = 1.1\times10^9$ cm^{-2}eV^{-1}. In Figure 8.10, we compare the Monte Carlo distribution with the measured distribution of $W\times L$=8×1 µm² devices with V_{gs}=0.4 V and V_{ds}=1.8 V, where the $\delta I_d/I_d$ used in the Monte Carlo simulation is depicted in Figure 8.9. In Figure 8.12 we compare the distributions of $W\times L$=8×0.14 µm² devices with V_{gs}=0.4 V and V_{ds}=0.1 V, and $\delta I_d/I_d$ depicted in Figure 8.11. In Figure 8.14 we compare the distributions of $W\times L$=0.8×8 µm² devices with V_{gs}=1.8 V and V_{ds}=1.8 V, and $\delta I_d/I_d$ depicted in Figure 8.13.

In Figure 8.10, despite the high impacts at the halo-implanted regions the noise distribution does not have two distinguishable lognormal distributions as shown in Figure 8.4. This happens because usually the sum of two lognormal distributions can be well approximated by one lognormal distribution (Beaulieu & Xie, 2004) and the effect shown in Figure 8.4 is given by a relation among the values of σ_1, σ_2, μ_1 and μ_2.

Figure 8.9 – Current deviation used in the Monte Carlo simulation for 8×1 μm² devices in 140-nm node with V_{gs} = 0.4 V and V_{ds} = 1.8 V.

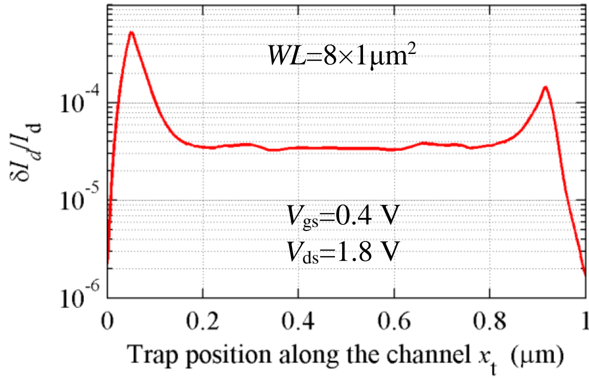

Figure 8.10 – Comparison of the Q-Q plot of measured and simulated ln(S_{Id}/I_d^2), for 8×1 μm² devices in 140-nm node with V_{gs} = 0.4 V and V_{ds} = 1.8 V.

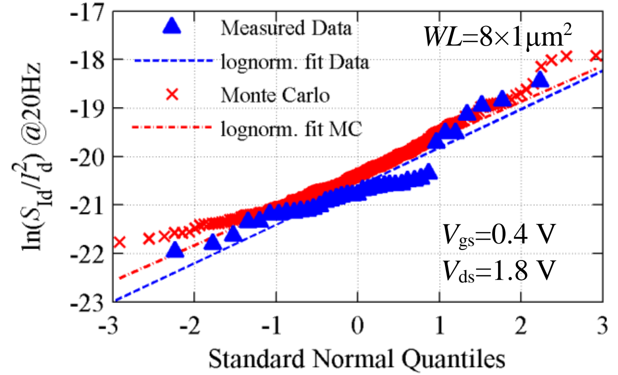

Figure 8.11 – Current deviation used in the Monte Carlo simulation for 8×0.14 μm² devices in 140-nm node with V_{gs} = 0.4 V and V_{ds} = 0.1 V.

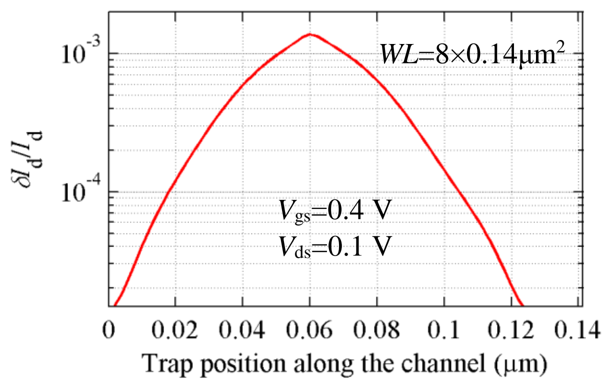

Figure 8.12 – Comparison of the Q-Q plot of measured and simulated ln(S_{Id}/I_d^2), for 8×0.14 μm² devices in 140-nm node with V_{gs} = 0.4 V and V_{ds} = 0.1 V.

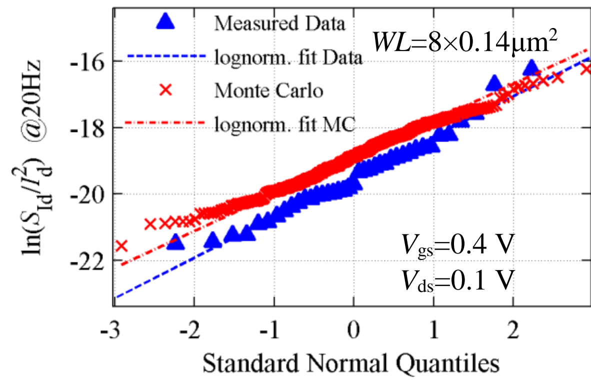

Figure 8.13 – Current deviation used in the Monte Carlo simulation for 0.8×8 μm² devices in 140-nm node with V_{gs}= 1.8 V and V_{ds}=1.8 V.

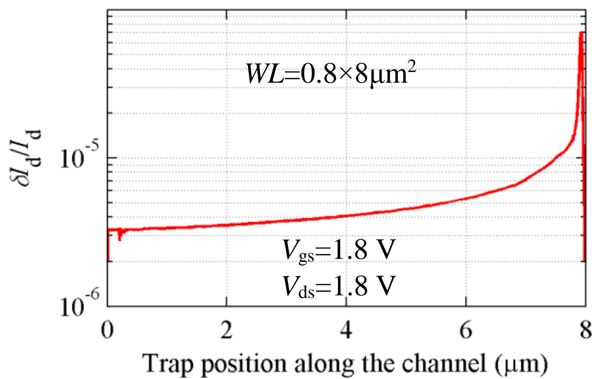

Figure 8.14 – Comparison of the Q-Q plot of measured and simulated ln(S_{Id}/I_d^2), for 0.8×8 μm² devices in 140-nm node with V_{gs}= 1.8 V and V_{ds}=1.8 V.

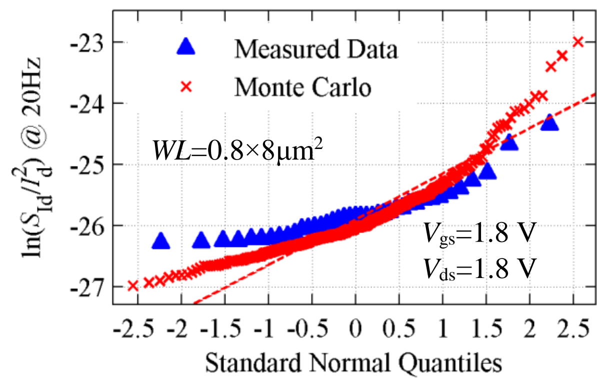

8.2 Very small area devices

As shown in Figure 8.15 in very small area devices the distribution of the LFN from the Monte Carlo simulation is no longer lognormal. However, as shown in the figure the distributions of the measured data are still lognormal. This causes a deviation, on the left tail of the distribution, between the Monte Carlo and the measured data.

Very small area devices have a very small number of traps per neper (or decade). For instance, n-channel devices in 140-nm technology with $W \times L$=0.232×0.14 μm^2, have $WL \times N_{tr}/\gamma$ = 0.49 traps per eV, which translate in a trap density per decade per eV of 1.12. Therefore, there is a high probability that some devices will have no traps with a time constant close to the analyzed frequency (f = 20 Hz in our analysis). This effect makes some devices to have a very low noise PSD, distorting the left tail of the distribution in the Monte Carlo simulation. However, such effect is not visible in the measured data.

There are some possible explanations from this deviation: in the measured devices, there are more traps with low noise power than simulated in the Monte Carlo; or there is another noise source in addition to RTN, which is responsible to increase the values of the left tail of the distribution hence making the final distribution lognormal. Figure 8.15 shows that neither the system noise floor nor the device white noise can explain these higher values.

Figure 8.15 – Q-Q plot of 43 measured devices with $W \times L$=0.232×0.14 μm^2 and the Q-Q plot of 100,000 Monte Carlo simulations with a constant trap density in energy of N_{tr}/γ = 1.5×10^9 cm^{-2}eV^{-1} and $\delta\tilde{I}_d$ = 2.8×10^{-13} cm^2 uniform from source to drain.

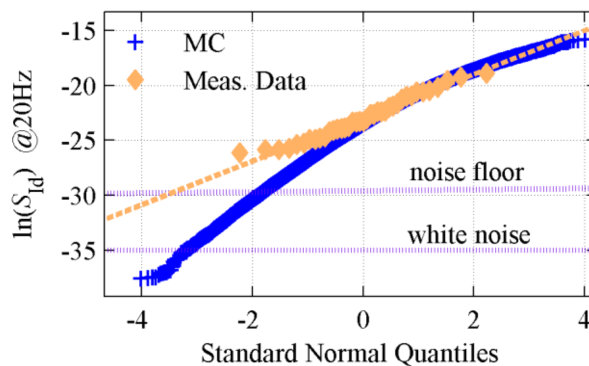

Despite the possibility of this effect be a consequence of additional noise sources we keep our efforts in explaining this deviation, in the Monte Carlo simulation, in the context of RTN, by considering that in the simulations depicted in Figure 8.15 the number of traps with very low noise power used was lower than in the actual device. There are two possible explanations for the measured device to have more traps with a lower noise power than simulated.

1) There is a high number of traps with energies away from the Fermi level. Traps with energies away from the Fermi level have a very low power due to the $\beta/(\beta+1)^2$ relation.

Due to this, as we show in Section 3.2, the Expected value, the Variance and K can be calculated using the trap density at the Fermi-level with a good precision. However, the very low values at the left tail of the distribution are sensitive to the trap density at energies away from the Fermi-level (in the Monte Carlo simulations of Figure 8.15 the trap densities are uniformly distributed in energy).

2) There is a higher number of traps with small ΔI_d than expected by the exponential distribution.

The first explanation is tested in the Monte Carlo simulation shown in Figure 8.16. The trap density in energy used is depicted in Figure 8.17. At the Fermi-level used in this simulation, the trap density is the same as the one used in the simulation of Figure 8.15. Hence, the Expected value, Variance and K are effectively the same from the original Monte Carlo. This can be verified in Figure 8.16 where the values of the right tail are approximately the same for the two different Monte Carlo simulations and for the measured data.

Figure 8.16 – Q-Q plot of the MC simulation using a varying trap density in energy.

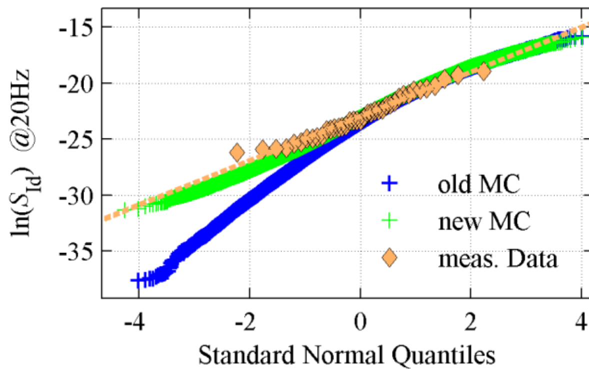

Figure 8.17 – Distribution of the trap density in energy and the arbitrary Fermi-level used for the MC simulation of Figure 8.16.

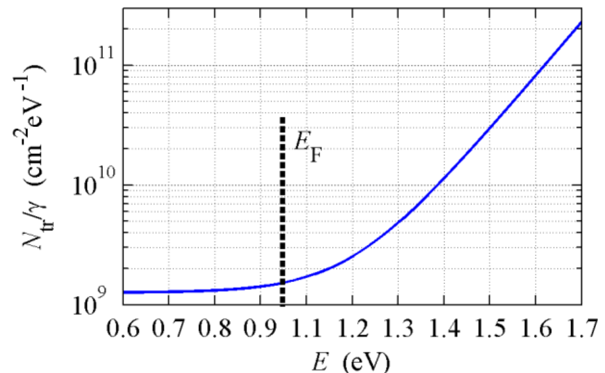

The second explanation can be interpreted in two different ways. In one interpretation, there is another independent set of traps with a lower δI_d. This set of traps can be originated from the edges of the device or in a region in the oxide away from the Si−SiO_2 interface (closer to the oxide-polysilicon interface). This interpretation is shown in Figure 8.18, in which another set of traps with 4 times the number of traps than the original set and δI_d 10 times smaller is added to the Monte Carlo simulation.

In the other interpretation, the nature of the ΔI_d distribution is not exponential but approximated as a Weibull distribution with the shape parameter (k_w) smaller than one (in the exponential distribution $k_w = 1$). In the derivation of K for the uniformly inverted channel we have

$$K = \frac{\mathrm{E}[\Delta I_d{}^4]}{\mathrm{E}[\Delta I_d{}^2]^2} \frac{1}{3\pi^2 kT} \frac{\gamma}{N_{tr}(E_F)} = \frac{6}{3\pi^2 kT} \frac{\gamma}{N_{tr}(E_F)}, \tag{7.25}$$

where the factor 6 comes from the relation between the fourth raw moment and the square of the second raw moment of the ΔI_d distribution, $E[\Delta I_d^4]/ E[\Delta I_d^2]^2$, which is equal to 6 for the Exponential distribution.

The Expected value is directly proportional to the second raw moment of the ΔI_d distribution ($E[\Delta I_d^2]$), which is equal to $2E[\Delta I_d]^2$ for the exponential distribution. Moreover, in the derivation of the model we considered that $E[\Delta I_d] = \delta I_d$, where δI_d is the current deviation calculated with a point charge at the Si−SiO_2 interface in a homogeneous channel (no random dopants effects).

Using (4.43), if $k_w = 0.51$, $E[\Delta I_d^4]/E[\Delta I_d^2]^2 \approx 60$ and $E[\Delta I_d^2] \approx 20E[\Delta I_d]^2$. By consequence the trap density extracted, using the Weibull distribution and (7.25), is 10 times larger than the one extracted by considering ΔI_d exponentially distributed. Therefore, in the Expected value equation the trap density used will be 10 times larger, also $E[\Delta I_d^2] = 20E[\Delta I_d]^2$ and as consequence $E[\Delta I_d]$ must be equal to $\delta I_d/10$ for the model to give the same Expected values. The result of the Monte Carlo simulation using $k_w = 0.51$ and $E[\Delta I_d] = \delta I_d/10$ is shown in Figure 8.19.

Although there is a nice fitting between the measured distribution and the distribution given by the Monte Carlo simulation using the Weibull distribution for ΔI_d, there is no experimental evidence in the literature showing that ΔI_d follows a Weibull distribution with $k_w < 1$. This can be explained in part because the measurement resolution used in the literature can be possibly incapable of measuring such large number of traps with such small ΔI_d, given by the Weibull with $k_w < 1$. Moreover, there is a lack of physical meaning in using $E[\Delta I_d] = \delta I_d/10$. Therefore, this is a topic that needs further investigations, especially in extracting the values and distribution of ΔI_d from measurements or from atomistic simulators.

Figure 8.18 – Resultant MC distribution after adding another set of traps with 4 times the trap density and δI_d 10 times smaller.

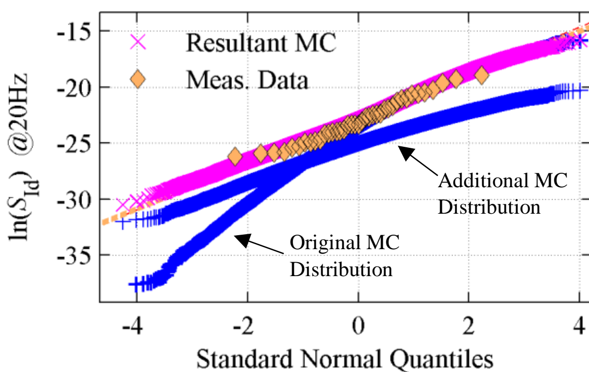

Figure 8.19 – Monte Carlo distribution considering ΔI_d with a Weibull distribution with k_w=0.51.

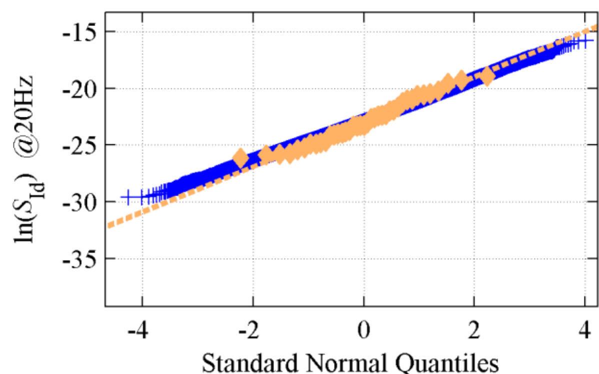

It is important to note that all possible solutions shown above, to give the measured lognormal shape to the MC simulation of small area devices, does not affect the LFN distributions of large area devices shown in the previous section. It, also, does not change the values calculated, using the proposed LFN model, for the Expected value, Variance and K, shown in previous chapters, for any device size.

9 MEASUREMENT & DATA ANALYSIS

9.1 Low Frequency Noise Characterization

In this work, in order to calculate the Low Frequency Noise statistics, we measured large populations of devices from different technologies, for various devices geometries and different bias configuration. All LF noise and DC measurements were done with the EDGE^{TM} system from Cascade Microtech depicted in Figure 9.1. The fully integrated measurement system provides the combination of LFN and DC IV measurements. It also offers an automatic multi-die and multi-site wafer stepping (Hansen, 2009). This provides a great automation of the LFN characterization and allows the acquisition of such large diversity of data.

Figure 9.1 – EDGE Low Frequency Noise system.

(Tuinhout & Duijnhoven, 2013)

Figure 9.2 shows the configuration of the LF noise measurement. The R_{load} resistor provides a load for the device such that a voltage divider is constructed from the drain and the bias supply. The center of this voltage divider is the point where the voltage is measured by the LNA. Hence, the data in the FFT represents the voltage-squared data taken at the drain of the device. This data is then converted to the equivalent noise input current of the device using

$$\overline{i^2} = \frac{\overline{v^2}}{R_{eq}^2}, \quad R_{eq} = \frac{R_{load} \cdot r_{ds}}{R_{load} + r_{ds}} \tag{8.1}$$

and r_{ds} is the drain to source resistance of the MOS transistor.

Figure 9.2 – Schematic of the LFN test setup.

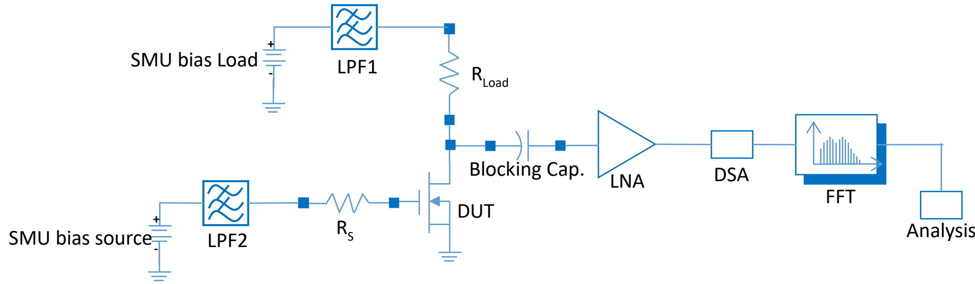

Adapted from (Hansen, 2009)

The measurement setup includes the possibility to set the gate and drain bias, and the source resistor (Rs) and the load resistors. The load resistor in conjunction with the parasitic capacitances of the devices and of the measurement equipment determines the system roll-off frequency. The roll-off frequency is the frequency at which the frequency response of the system dominates the behavior of the noise PSD and can be calculated as

$$F_{rolloff} = \frac{1}{2\pi RC} , \qquad (8.2)$$

where R is the Thevenin equivalent of the resistive loads and C is the capacitance of the measuring system and cables. Hence, the load resistor can be selected to optimize the roll-off frequency. However, it must still provide enough impedance to drive properly the drain current. Figure 9.3 demonstrates an example of the roll-off frequency found in our measured noise PSD data. Figure 9.4 shows an example of the frequency response of the system dominating the PSD characteristics and generating non-reliable data.

Figure 9.3 – Roll-off frequency for 10×10 μm^2 n-channel devices with V_{gs} = 0.9 V, V_{ds} = 0.5 V, r_{ds} ≈ 14 KΩ and R_{load} =10 KΩ.

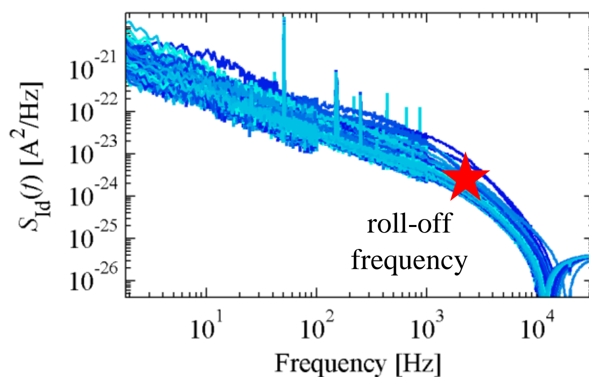

Figure 9.4 – Roll-off frequency smaller than 10 Hz. For n-channel devices with W×L = 8×30 μm^2, V_{gs} = 1.8 V, V_{ds}=0.1 V, r_{ds} ≈ 13 KΩ and R_{load} = 10 KΩ.

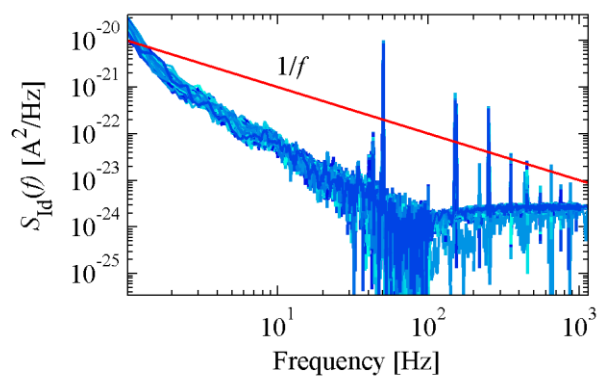

The load resistor also defines how much of the system noise floor is added to the drain voltage noise, through (8.1). Figure 9.5 shows the system noise floor added to the drain voltage noise of the device under test. The figure shows that for a frequency around 10 Hz the system noise is around -

150 dB. Then, for the setup in Figure 9.4, the converted current noise of the system noise floor is approximately 3×10^{-23} A^2/Hz, which is very close to the measured noise.

Figure 9.5 – Noise floor of the low frequency noise measurement system

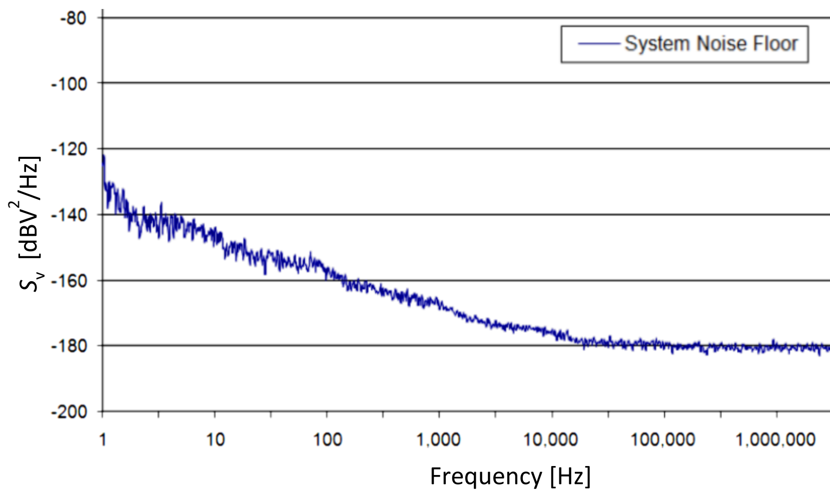

(Hansen, 2009)

One problem in looking at noise with an FFT is that the obtained spectrum is inherently noisy. Due to this problem, the system allows to use averaging in the FFT data. Averaging sacrifices the information of low frequencies to decrease the noise of the FFT data. This method divides the time domain in many windows of the same size and the FFT result of each window is averaged out, resulting in a smoother frequency domain response. In our analysis, averaging was commonly set as 25× for 1 Hz to 100 Hz, 250× for 100 Hz to 1 KHz and 2500× for higher bands.

From Parseval's theorem, the resulting variance in the FFT spectrum is given by S_{Id}^2 divided by the averaging number. As instance, for an averaging set as 25× the variance in the FFT spectrum is $S_{Id}^2/25$. For devices with very small LFN variability, this inherent variance in the FFT spectrum can interfere in the proper extraction of the LFN variability. Therefore, after acquiring the data from the measurement system we also treat the FFT data in MATLAB, using a smoothing function. The smoothing function also helps to smooth out spikes and some interferences found in the spectrum. Figure 9.6 and Figure 9.7 show examples of the data before and after smoothing.

Figure 9.6 – Smoothing function applied to four 1×0.06 μm^2 n-channel device with V_{gs}=1.2 V, V_{ds}=0.5 V.

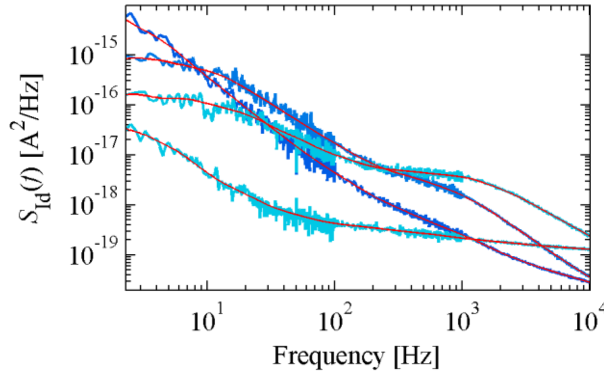

Figure 9.7 – Smoothing function applied to a 10×10 μm^2 n-channel device with V_{gs}=1.2 V, V_{ds}=0.5 V.

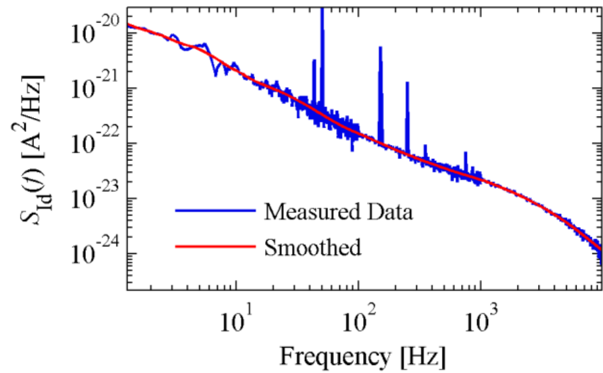

9.2 Lognormal Estimators

In this section of the work, we are going to analyze three different ways to estimate the expected value, the variance and the normalized variance (variance/mean^2) of a lognormal distribution. The three different methods are characterized by its bias and variance. From these analyses, we are going to discuss which estimator is more convenient to use in the low frequency noise analysis.

The three different methods analyzed are as follow:

Method 1 – Sample Mean and Variance

Method 1 consists of the simple use of the sample mean and sample variance of the original data. Therefore, the estimated population mean, the estimated population variance and the estimated population normalized variance are given by

$$m_1 = \frac{1}{n}\sum_{i=1}^{n} x_i \ , \tag{8.3}$$

$$s_1^2 = \frac{1}{n-1}\sum_{i=1}^{n}(x_i - m_1)^2 \tag{8.4}$$

and s_1^2 / m_1^2 respectively. Where, x_i is the original ith observation, n is the size of the observation.

Method 2 – Maximum Likelihood Estimator

Method 2 is given by the Maximum Likelihood Estimator (MLE), which calculates the mean and variance of the normal distribution and then transforms back to the lognormal distribution using the distribution properties. Using MLE we have:

$$m_2 = e^{\mu+\sigma^2/2}, \tag{8.5}$$

$$s_2^2 = e^{2\mu+\sigma^2}(e^{\sigma^2}-1), \tag{8.6}$$

$$s_2^2 / m_2^2 = e^{\sigma^2}-1, \tag{8.7}$$

where

$$\mu = \frac{1}{n}\sum_{i=1}^{n}\ln(x_i) \tag{8.8}$$

and

$$\sigma^2 = \frac{1}{n-1}\sum_{i=1}^{n}(\ln(x_i)-\mu)^2 \tag{8.9}$$

Method 3 – UMVU Estimator

The method 3 is given by the Uniformly Minimum Variance Unbiased Estimator (UMVUE). As its name already says, this estimator is unbiased and it has the minimum variance. Using UMVUE, we have

$$m_3 = e^{\mu} f(\sigma^2/2), \tag{8.10}$$

$$s_3^2 = e^{2\mu}\left[f(2\sigma^2) - f\left(\frac{n-2}{n-1}\sigma^2\right)\right], \tag{8.11}$$

where

$$f(t) = 1 + t\frac{n-1}{n} + \sum_{k=2\ldots}\left(\frac{t^k (n-1)^{2k-1}}{n^k k!}\prod_{l=2}^{k}\frac{1}{n+2l-3}\right) \tag{8.12}$$

Evaluation of the Methods

The three methods are compared with respect to its mean, median and variance for each parameter estimated (mean, variance and variance/mean^2). The variance of the parameter estimated is compared by the 2th and 98th percentile calculation. The influence of the sample size on these estimators is determined by swiping from 15 to 150 observations. To compare the three methods, 100,000 Monte Carlo simulations were done, for each sample size, using Matlab for generating random variables from the lognormal distribution described in Table 9.1. Then for each sample size the mean, median and the 2th and 98th percentiles were calculated from the 100,000 simulations.

Table 9.1 shows the statistics of a lognormal distribution found in our LFN measurements for a small area device.

Table 9.1 – Statistics of the lognormal distribution used in the Monte Carlo simulation.

Mean	Variance	Mean of log (μ)	SD of log (σ)	Variance/Mean^2
1.04×10^{-8}	**2.66×10^{-15}**	**-20**	**1.8**	**24.53**

Figure 9.8 shows the estimation of the mean for the three methods. In the figure, we can see that Method 1 and Method 3 are unbiased estimators for the mean, as their means of estimated means are equal to the distribution's mean from Table 9.1. Method 2 is a biased estimator for the mean; however, it is symmetrical around the distribution mean. Hence, the median of the estimations is unbiased. Figure 9.8 also shows that Method 3 gives a smaller variability in the estimations.

Figure 9.8 – Estimation of the Expected value of a lognormal distribution using three different methods.

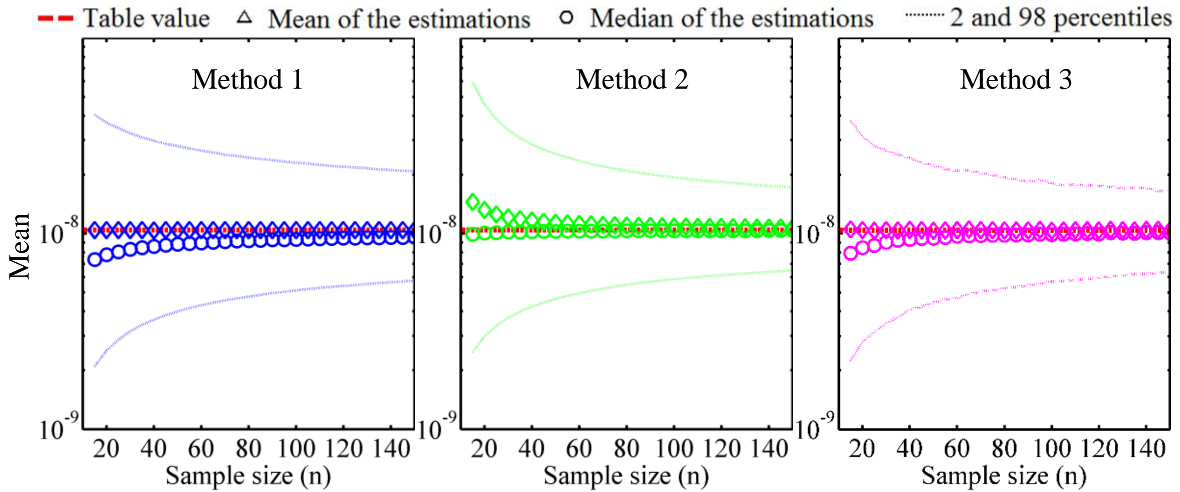

Figure 9.9 shows the estimation of the variance for the three methods. In the figure, we can see that Method 1 and Method 3 are also unbiased estimators for the variance, as their means of estimated variance are equal to the distribution's variance in Table 9.1. Again, Method 3 gives a smaller estimations' variability and Method 2 is a biased estimator for the variance. However, it is symmetrical around the distribution's variance and the median of the estimations is unbiased. This symmetry is an important propriety for estimators of lognormal distributions as it gives the same probability to find lower and higher values than the distribution's parameter.

Figure 9.9 – Estimation of the Variance of a lognormal distribution using three different methods.

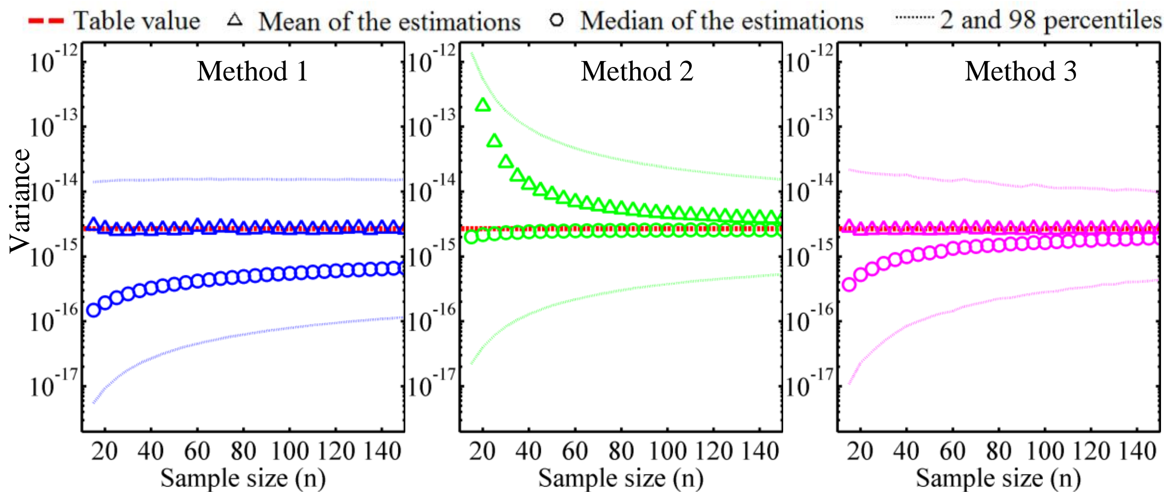

Figure 9.10 shows the estimation of the variance/mean^2 for the three methods. In the figure, we can see that all three methods are biased estimators for the normalized variance. However, Method 2 is symmetrical around the distribution's normalized variance and the median of the estimations is unbiased.

Because of the symmetry property of Method 2, in this work we use this method to evaluate the E[S_{Id}], Var[S_{Id}] and K. Section 9.3 shows how the bootstrap analysis behaves using the three methods and the reasons for choosing Method 2 may become more evident.

Figure 9.10 – Estimation of the Variance/mean^2 of a lognormal distribution using three different methods.

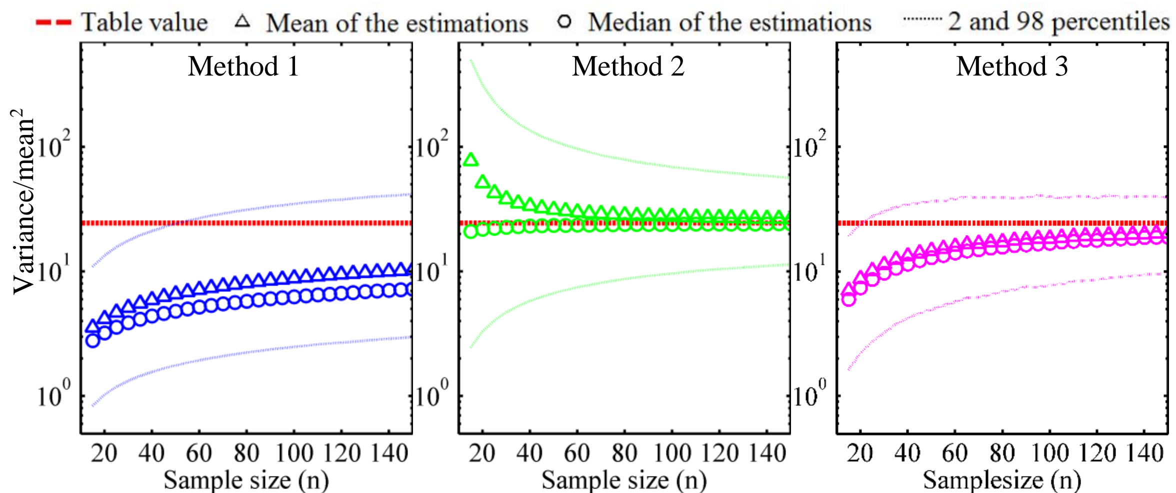

9.3 Bootstrapping

Bootstrapping is a resampling method efficient for calculating the uncertainty and the confidence interval of an estimation. The method randomly samples the observations with repetition, keeping the original size of observations of the original population, repeating the process for thousands of times. Hence, for an original population of N observation the bootstrap creates M new populations of N observations and values of the original observations may appear multiples times in the new resampled population. For every population of N observations new means, variances and normalized variances are calculated. Therefore, from the M quantities of mean, variance and normalized variance calculated, one can calculate the uncertainties from the mean, variance and normalized variance estimations.

In order to test the behavior of the three methods, described in Section 9.2, in the bootstrapping analysis, 20 populations of 50 observations (n = 50) were taken from the true lognormal distribution described in Table 9.1. For all the 20 populations the mean, variance and variance/mean^2 was calculated using the three methods and for all the 20 populations a bootstrap analysis with 100000

draws was done to determine the uncertainty of the estimations. The uncertainty was calculated using 2th and 98th percentiles and the results can be seen in Figure 9.11, Figure 9.12 and in Figure 9.13.

From the figures bellow we can see that despites Method 2 has a larger variability than Method 3 and be a biased estimator (Section 9.2) the symmetry propriety makes Method 2 a better estimator and the calculated uncertainty bars more often englobe the true distribution value, differently than what is seen for Method 1 and 3.

Figure 9.11 – Bootstrapping analysis of 50 observations using three different estimation methods for the expected value.

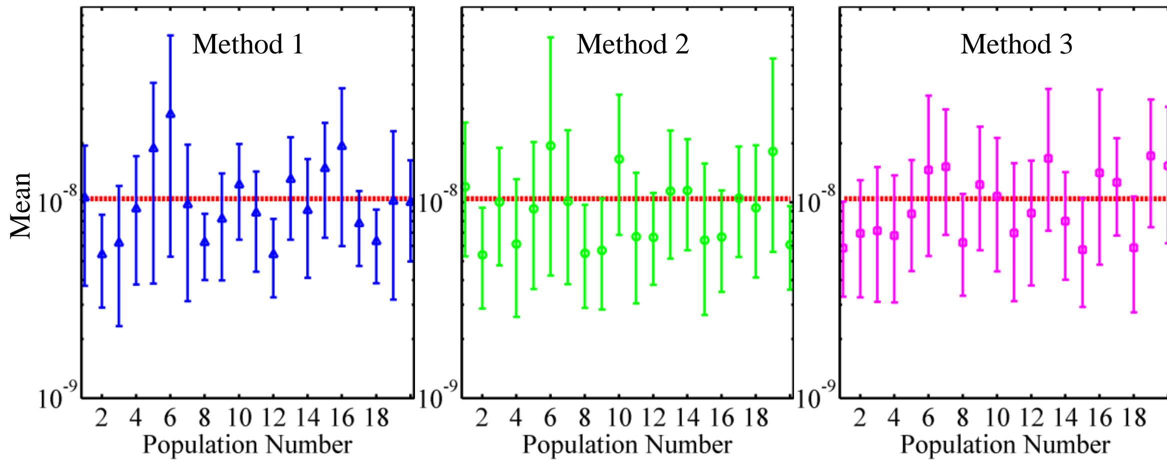

Figure 9.12 – Bootstrapping analysis of 50 observations using three different estimation methods for the variance.

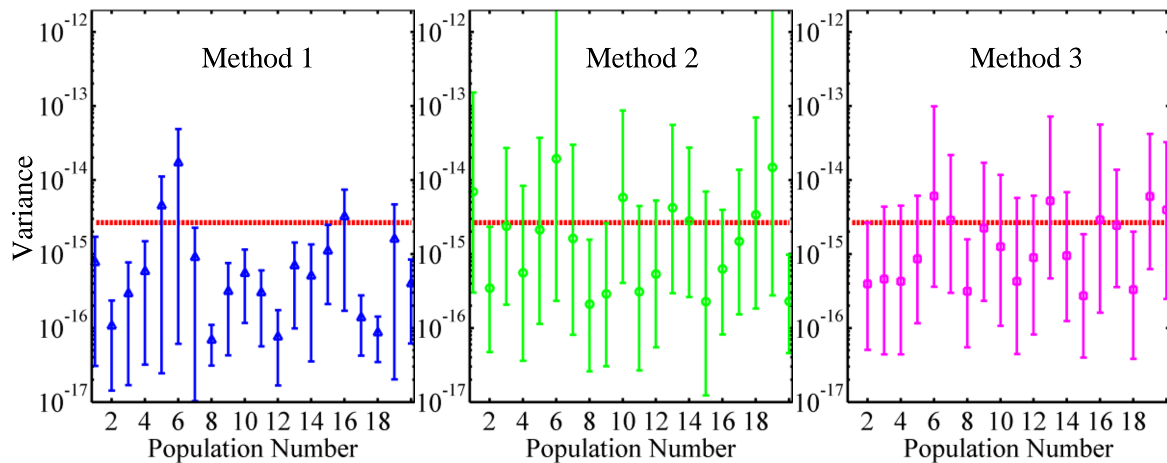

Figure 9.13 – Bootstrapping analysis of 50 observations using three different estimation methods for variance/mean^2.

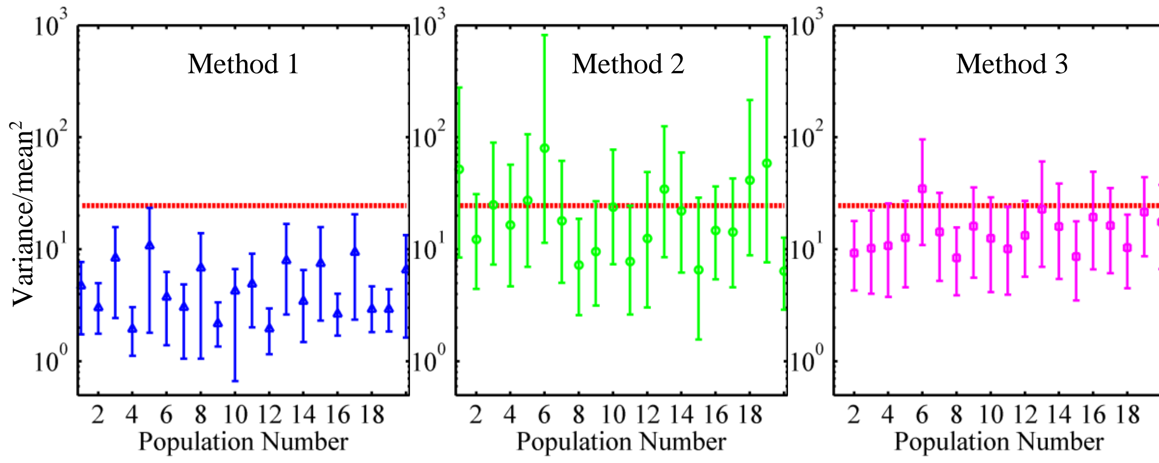

10 CONCLUSION

In this work, we proposed a new physics-based RTN model to describe the statistics of the low frequency noise in MOSFETs. Using the model, we explained the behavior of the LF noise statistics as a function of device biases, geometry and physical parameters. The applicability of the model is demonstrated through numerous results for n-channel and p-channel devices from different mixed-signal CMOS technology nodes. The model is well suited for both large and small area devices, and for both $1/f$ like and Lorentzian dominated spectra. Using the lognormal nature of noise distribution, we also explained why variability of RTN does not follow a $1/\sqrt{\text{area}}$ dependency, as it is still commonly assumed in literature.

From our measurements, we show that the noise variability ($\sigma[\ln(S_{Id})]$) of long channel devices is a strong function of drain and gate biases, while the variability of short channel devices is weakly dependent on bias. Using the proposed model, we explain these observations. We, also, analyze and explain, using the proposed model, the effect of the halo-implanted regions in the LF noise statistics, which can considerably increase the noise variability of long channel devices under weak inversion operation.

Furthermore, we showed that the statistics of the LF noise of n-channel and p-channel devices are different. We explained this difference using the proposed model and considering that the trap density of p-channel devices is a varying function of the quasi-Fermi level, while the trap density of n-channel devices can be considered constant in energy.

Moreover, we introduced the normalized parameter K that allows us to compare the noise variability among different device technologies, geometries and biases. Under given bias condition, we demonstrated that this parameter is technology specific and can be used to compare the dielectric quality of different technologies.

Finally, we showed that the proposed model can be transformed into a compact model, suited for circuit simulators and we analyzed some of the possibilities to implement it.

REFERENCES

Aarts, A. C. T., Smit, G. D. J., Scholten, A. J. & Klaassen, D. B. M., 2008. A PSP-Based Small-Signal MOSFET Model for Both Quasi-Static and Nonquasi-Static Operations. *Transaction on Electron Devices,* 55(6), pp. 1424 - 1432.

Agostinelli, M. et al., 2005. *Erratic fluctuations of sram cache vmin at the 90nm process technology node.* s.l., s.n., pp. 655-658.

Asenov, A., Balasubramaniam, R., Brown, A. & Davies, J., 2003. RTS amplitudes in decananometer MOSFETs: 3-D simulation study. *Electron Devices, IEEE Transactions on,* 50(3), pp. 839 - 845.

Beaulieu, N. C. & Xie, Q., 2004. An Optimal Lognormal Approximation to Lognormal Sum Distributions. *IEEE Transactions on Vehicular Technology,* 53(2), pp. 479 - 489.

Berz, F., 1970. Theory of low frequency noise in Si MOST's. *Solid-State Electronics,* 13(5), pp. 631-647.

Bukhori, M. et al., 2010. *'Atomistic' simulation of RTS amplitudes due to single and multiple charged defect states and their interactions.* Stanford Sierra, s.n.

Campbell, J. et al., 2009. *Random telegraph noise in highly scaled nMOSFETs.* Montreal, s.n.

Chauhan, Y. S. et al., 2013. *BSIM6.0 MOSFET Compact Model: Technical Manual.* [Online]
Available at: http://www-device.eecs.berkeley.edu/bsim/Files/BSIM6/BSIM6.0.0/BSIM6.0.0_Technical_manual.pdf
[Accessed 1 June 2016].

Chauhan, Y. S. et al., 2013. BSIM6: Analog and RF Compact Model for Bulk MOSFET. *Transaction on Electron Devices,* 17 October, 61(2), pp. 23-244.

Christensson, S. & Lundström, I., 1968. Low frequency noise in MOS transistors—II Experiments. *Solid-State Electronics,* 11(9), pp. 813-820.

Christensson, S., Lundström, I. & Svensson, C., 1968. Low frequency noise in MOS transistors—I Theory. *Solid-State Electronics,* 11(9), pp. 797-812.

Fu, H.-S. & Sah, C.-T., 1972. Theory and experiments on surface 1/f noise. *IEEE Transactions on Electron Devices,* 19(2), pp. 273 - 285.

Ghibaudo, G. & Roux-dit-Buisson, O., 1994. *Low Frequency Fluctuations in Scaled Down Silicon CMOS Devices Status and Trends.* Edinburgh, s.n.

Grasser, T., 2012. Stochastic charge trapping in oxides: From random telegraph noise to bias temperature instabilities. *Microelectronics Realiability,* 52(1), pp. 39 - 70.

Grasser, T. et al., 2009. *Switching Oxide Traps as the Missing Link Between Negative Bias Temperature Instability and Random Telegraph Noise.* San Francisco, s.n.

Hall, R. N., 1952. Electron-Hole Recombination in Germanium. *Physics Review,* July, 87(3), pp. 387-387.

Hansen, M., 2009. *Achieving Accurate On-Wafer Flicker Noise Measurements Through 30 MHz.* [Online]
Available at: https://www.cascademicrotech.com/files/30MHzFlickerNoiseMeasurement-WP.pdf
[Accessed 21 June 2016].

Higashi, Y. et al., 2014. Unified Transient and Frequency Domain Noise Simulation for Random Telegraph Noise and Flicker Noise Using a Physics-Based Model. *IEEE Transactions on Electron Devices ,* 61(12), pp. 4197 - 4203.

Hooge, F. N. & Vandamme, L. K. J., 1978. Lattice scattering causes 1/*f* noise. *Physics Letters A,* 6(4), pp. 315-316.

Hung, K. K., Ko, P. K., Hu, C. & Cheng, Y. C., 1990. A Physics-Based MOSFET Noise Model for Circuit Simulators. *IEEE Transactions on Electronics Devices,* May, 37(5), pp. 1323-1333.

Hung, K. K., Ko, P. K., Hu, C. & Cheng, Y. C., 1990. A Unified Model for the Flicker Noise in Metal-Oxide-Semiconductor Field-Effect Transistors. *IEEE Transactions on Electronics Devices,* March, 37(3), pp. 654-665.

Hung, K. K., Ko, P. K., Hu, C. & Cheng, Y. C., 1990. Random Telegraph Noise of Deep-Submicron MOSFETs. *IEEE Electron Device Letter,* 11(2), pp. 90-92.

Ioannidis, E. et al., 2011. *Low frequency noise variability in high-k/metal gate stack 28nm bulk and FD-SOI CMOS transistors.* San Francisco, s.n.

Ioannidis, E. et al., 2013. *Evolution of low frequency noise and noise variability through CMOS bulk technology nodes.* Montpellier, s.n.

Johnson, N. L., Kotz, S. & Balakrishnan, N., 1994. *Continuous Univariate Distributions Vol. 1.* New York: Wiley.

Kaczer, B., Roussel, P. J., Grasser, T. & Groeseneken, G., 2010. Statistics of Multiple Trapped Charges in the Gate Oxide of Deeply Scaled MOSFET Devices—Application to NBTI. *Electron Device Letters,* 31(5), pp. 411-413.

Kim, S., Choi, S.-J., Moon, D.-I. & Choi, Y.-K., 2011. An Extraction Method of the Energy Distribution of Interface Traps by an Optically Assisted Charge Pumping Technique. *IEEE Transactions on Electron Devices,* 58(11), pp. 3667 - 3673.

Kirton, M. J. & Uren, M. J., 1989. Noise in Solid State Microstructures: A New Perspective on Individual Defects, Interface States and Low-frequency(1/f) Noise. *Advanced in Physics,* July, 38(4), pp. 367-468.

Klaassen, F. M. & Prins, J., 1967. Thermal noise of MOS transistors. *Philips Research Report,* Volume 22, p. 505–514.

Kolhatkar, J., Vandamme, L., Salm, C. & Wallinga, H., 2003. *Separation of random telegraph signals from 1/f noise in MOSFETs under constant and switched bias conditions.* Estoril, s.n.

Li, X. et al., 2008. *PSP 102.3.* [Online]
Available at: http://www.nxp.com/wcm_documents/models/mos-models/model-psp/psp102p3_summary.pdf
[Accessed 1 June 2016].

Lopez, D. et al., 2011. Low-Frequency Noise Investigation and Noise Variability Analysis in High-k /Metal Gate 32-nm CMOS Transistors. *IEEE Transactions on Electron Devices,* 27 July, 58(8), pp. 2310 - 2316.

Machlup, S., 1954. Noise in Semiconductors: Spectrum of a Two-Parameter Random Signal. *Journal of Applied Physics,* 25(3), pp. 341 - 343.

Mainetti, L., Patrono, L. & Vilei, A., 2011. *Evolution of wireless sensor networks towards the Internet of Things: A survey.* Split, s.n.

McWhorter, A., 1957. *1/f Noise and Germanium Surface Properties.* RH Kingston, s.n.

Mueller, H. H. & Schulz, M., 1996. Conductance modulation of submicrometer metal–oxide–semiconductor field-effect transistors by single-electron trapping. *Journal of Applied Physics,* 79(8), pp. 4178 - 4186.

Mueller, H. H. & Schulz, M., 1998. Random telegraph signal: An atomic probe of the local current in field-effect transistors. *Journal of Applied Physics,* 83(3), pp. 1734-1741.

Nour, M. et al., 2016. A Stand-Alone, Physics-Based, Measurement-Driven Model and Simulation Tool for Random Telegraph Signals Originating From Experimentally Identified MOS Gate-Oxide Defects. *IEEE Transactions on Electron Devices,* 63(4), pp. 1428 - 1436.

Palma, A. et al., 1997. Quantum two-dimensional calculation of time constants of random telegraph signals in metal-oxide–semiconductor structures. *Physical Review B,* 56(15), pp. 9565 - 9574.

Paydavosi, N. et al., 2013. *Flicker noise in advanced CMOS technology: Effects of halo implant.* Bucharest, s.n.

Pelgrom, M., Duinmaijer, A. C. & Welbers, A., 1989. Matching properties of MOS transistors. *IEEE Journal of Solid-State Circuits,* 24(5), pp. 1433-1439.

Ralls, K. S. et al., 1984. Discrete Resistance Switching in Submicrometer Silicon Inversion Layers: Individual Interface Traps and Low-Frequency (1/f) Noise. *Physical Review Letters,* January, 52(3), pp. 228-231.

Reimbold, G., 1984. Modified 1/f trapping noise theory and experiments in MOS transistors biased from weak to strong inversion—Influence of interface states. *Electron Devices, IEEE Transactions on,* 31(9), pp. 1190 - 1198.

Roy, A. S., Enz, C. C. & Sallese, J.-M., 2007. Noise Modeling in Lateral Nonuniform MOSFET. *IEEE Transaction on Electron Devices,* 58(8), pp. 1994-2001.

Scholten, A. et al., 2003. Noise modeling for RF CMOS circuit simulation. *Electron Devices, IEEE Transactions on,* 50(3), pp. 618 - 632.

Scofield, J. H., Borland, N. & Fleetwood, D. M., 1994. Reconciliation of Different Gate-Voltage Dependencies of 1/f noise in n-MOS and p-MOS Transistors. *IEEE Transactions on Electron Devices,* 40(11), pp. 1946-1952.

Scofield, J. H., Coll, O., Borland, N. & Fleetwood, D. M., 1994. Reconciliation of Different Gate-Voltage Dependencies of 1/f noise in n-MOS and p-MOS Transistors. *Transactions on Electron Devices,* November, 41(11), pp. 1946 - 1952.

Shockley, W. & Read, W. T., 1952. Statistics of the Recombinations of Holes and Electrons. *Physical Review,* September, 87(5), pp. 835-842.

Simoen, E., Dierickx, B., Claeys, C. & Declerck, G., 1992. Explaining the amplitude of RTS noise in submicrometer MOSFETs. *IEEE Transactions on Electron Devices,* 39(2), pp. 422 - 429.

Srinivasan, P. & Dey, S., 2012. *New and critical aspects of 1/f noise variability in advanced CMOS SoC technologies.* San Francisco, s.n., pp. 19.3.1 - 19.3.4.

Toh, S. O., 2009. *Impact of random telegraph signals on Vmin in 45nm SRAM.* s.l., IEEE International, pp. 1-4.

Tuinhout, H. & Duijnhoven, A. Z.-v., 2013. *Evaluation of 1/f noise variability in the subthreshold region of MOSFETs.* Osaka, s.n.

Vandamme, L., Li, X. & Rigaud, D., 1994. 1/f noise in MOS devices, mobility or number fluctuations?. *Electron Devices, IEEE Transactions on,* 41(11), pp. 1936 - 1945.

Wang, K. L., 1980. MOS interface-state density measurements using transient capacitance spectroscopy. *IEEE Transactions on Electron Devices,* 27(12), pp. 2231 - 2239.

Wirth, G. et al., 2009. *Statistical model for MOSFET low-frequency noise under cyclo-stationary conditions.* s.l., s.n., pp. 1-4.

Yu, B. et al., 2012. *Modeling local variation of low-frequency noise in MOSFETs via sum of lognormal random variables.* San Jose, s.n.